DOCTORAL DISSERTATION

High Frequency Analysis of Permanent Magnet Motors

YERAI MORENO LAFUENTE

Supervised by
DR. GAIZKA ALMANDOZ LARRALDE
and
DR. ARITZ EGEA CACERES

Electronics and Computer Science Department
Mondragon Unibertsitatea

MAY 2024

Submitted in fulfillment of the requirements of the

PHD PROGRAMME IN APPLIED ENGINEERING

High Frequency Analysis of Permanent Magnet Motors

Submitted in fulfillment of the requirements of the

PHD PROGRAMME IN APPLIED ENGINEERING

Presented by

YERAI MORENO LAFUENTE

Supervised by

DR. GAIZKA ALMANDOZ LARRALDE

and

DR. ARITZ EGEA CACERES

Electronics and Computer Science Department
Mondragon Unibertsitatea

In HERNANI, MAY 2024

Thesis Committee:

President: Dr. Claudia Steluta Martis (Technical University of Cluj-Napoca)
Vocal: Dr. Konstantin Vostrov (Lappeenranta University of Technology)
Vocal: Dr. Jose-Enrique Ruiz-Sarrio (Universitat Politècnica de València)
Vocal: Dr. Aitor Etxeberria (Orona Innovation Center)
Secretary: Dr. Javier Poza Lobo (Mondragon Unibertsitatea)

This research was partially funded by the Non Doctoral Research Staff Training Programme of the Department of Education of the Basque Government, with grant numbers PRE-2020-1-0229, PRE-2021-2-0057, PRE-2022-2-0001 and PRE-2023-2-0001.

STATEMENT OF ORIGINALITY

Hereby I declare that this dissertation is my original authorial work, which I have worked out on my own. All sources, references, and literature used or excerpted during the elaboration of this work are properly cited and listed in complete reference to the due source.

Yerai Moreno Lafuente
Hernani, May 2024

ACKNOWLEDGMENTS

I want to express my gratitude to all who contributed to the completion of this PhD thesis, for their support and encouragement.

I would like to start by thanking my supervisors Gaizka Almandoz and Aritz Egea for their guidance and support during this PhD. Thank you for trusting me to do this research and helping me on this journey. I would not have reached this milestone without you.

I would also like to acknowledge Prof. Bernd Ponick and all the team for receiving me at the IAL. Thanks to Cara and all of the IAL colleagues for making my stay in Hannover even more rewarding and welcoming me into the group from the first day.

Many thanks to all my friends and colleagues who have been with me all this time. You make every working day more enjoyable. Sharing every moment of this roller coaster with you makes the bad moments less bad and the good moments great.

A Ainhoa, gracias por estar a mi lado durante la tesis. Los momentos difíciles han sido más fáciles gracias a ti.

A mis padres y a mi hermano, gracias por vuestro apoyo constante y por darme la energía para seguir adelante cada día. A mi padre, en particular, quiero agradecerle por ser mi guía en el fascinante mundo de las máquinas eléctricas y por contagiarme su pasión por la enseñanza. Sin vosotros, no hubiera llegado hasta aquí. Muchísimas gracias.

ABSTRACT

The trend towards electrification has led to an increased use of wide-bandgap semiconductors in electric drives. These semiconductors allow the development of high power density and high efficiency drives, but also present challenges related to Electromagnetic Interference (EMI) due to their higher voltage derivatives. These derivatives lead to voltage overshoots at the machine terminals, which can potentially damage the insulation of the machine. Therefore, the aim of this PhD is to develop a complete design methodology that makes it possible to optimise the electrical machine also from the Electromagnetic Compatibility (EMC) point of view.

The research begins with a comprehensive literature review on high-frequency modelling of electrical machines and the impact of design parameters on their high-frequency behaviour. This review also covers an overview of the current tools used for these models.

A novel high-frequency model of the electrical machine based on FEM simulations is presented. This model, validated on various industrial machines, extends beyond most existing models in the literature, covering a frequency range of 100 Hz to 50 MHz. The validation process incorporates data from 28 samples from one machine to account for manufacturing tolerances.

In addition, the high-frequency machine model is integrated in a whole drive model. This model, validated with experimental measurements, enables EMI analysis considering all drive components, including the inverter, cable, and EMC filter. Unlike models in the existing literature that use motor behavioural models derived from experimental measurements, the proposed model uses impedance data from FEM simulations. This approach allows for the prediction of common-mode currents right from the design stage.

The thesis concludes with an analysis of how design variables influence the impedance of the electrical machine and, consequently, the drive's common-mode currents. It introduces a new design methodology for electrical machines that incorporates the EMC perspective. Two industrial machines exceeding the EMI regulation limits serve as case studies. The thesis proposes a design improvement that successfully reduces their common-mode current. This last point highlights the significant contribution of this research to the field of electrical machine design and EMC optimisation.

LABURPENA

Elektrifikaziorako joerak banda zabaleko erdieroaleen erabilera handitzea bultzatu du. Erdieroale hauek potentzia-dentsitate eta errendimendu altuko eragingailuak garatzeko aukera ematen duten arren, sortzen diren tentsio-deribatu handiek Interferentzia Elektromagnetikoekin (EMI) lotutako erronkak aurkezten dituzte. Deribatu horiek sorturiko gaintentsioak direla eta, makinaren isolamendua kaltetu daiteke. Beraz, doktorego-tesi honen helburua makina elektrikoa Bateragarritasun Elektromagnetikoaren (EMC) ikuspegitik optimizatzea ahalbidetuko duen diseinu-metodologia oso bat garatzea da.

Lehenik eta behin, makina elektrikoen maiztasun altuko modelizazioari eta makinaren diseinu-parametroek maiztasun altuko portaeran duten eraginari buruzko berrikuspen bibliografiko sakona egiten da. Bertan modelo horietarako gaur egun erabiltzen diren baliabideak deskribatzen dira.

Ondoren, literaturan dauden modelo gehienetatik haratago doan maiztasun altuko inpedantzia modelo berri bat aurkezten da, elementu finituen simulazioetan oinarritua. Modelo hau makina industrial desberdinak erabilita balidatu da 100 Hz-tik 50 MHz-ra bitarteko maiztasun-tartean. Fabrikazio tolerantziak kontuan hartzeko, makina baten 28 lagin desberdin aztertu dira.

Gainera, makinaren maiztasun altuko eredua eragingailu elektriko oso baten modeloan integratzen da. Modelo hau neurketa esperimentalen bidez balioztatzen da, eta eragingailuaren osagai guztiak kontuan hartuta EMI analisiak egiteko aukera ematen du, inbertsorea, kablea eta EMC iragazkia barne. Literaturan dauden ereduek ez bezala, zeinek neurketa esperimentaletatik eratorritako motorraren ereduak erabiltzen dituzten, proposatutako ereduak elementu finituekin simulatutako inpedantziak erabiltzen ditu. Honek diseinu-fasean modu komuneko korronteak aurreikusteko aukera ematen du.

Azkenik, diseinu aldagaiek makina elektrikoaren inpedantzian eta, ondorioz, eragingailuaren modu komuneko korronteetan duten eragina aztertzen da. Makina elektrikoak EMC ikuspuntutik diseinatzeko metodologia bat garatzen da. Hau aztertzeko EMI araudiaren mugak gainditzen dituzten bi makina industrial erabiltzen dira eta modu komuneko korrontea murrizten duen diseinu hobekuntza bat proposatzen da. Azken atal honek makina elektrikoen diseinuan eta bateragarritasun elektromagnetikoaren optimizazioan egindako ekarpenaren garrantzia azpimarratzen du.

RESUMEN

La tendencia hacia la electrificación ha llevado a un mayor uso de semiconductores de banda ancha en los accionamientos eléctricos. Estos semiconductores permiten desarrollar accionamientos de alta densidad de potencia y alto rendimiento. Sin embargo, también plantean retos relacionados con las interferencias electromagnéticas (EMI) debido a sus elevadas derivadas de tensión. Estas derivadas provocan sobretensiones en los terminales de la máquina, que pueden dañar el aislamiento de la misma. Por lo tanto, el objetivo de esta tesis es desarrollar una metodología de diseño completa que permita optimizar la máquina eléctrica también desde el punto de vista de la Compatibilidad Electromagnética (EMC).

La investigación comienza con una exhaustiva revisión bibliográfica sobre el modelado de alta frecuencia de las máquinas eléctricas y el impacto de los parámetros de diseño en su comportamiento a alta frecuencia. Esta revisión también cubre una visión general de las herramientas actuales utilizadas para estos modelos.

Se presenta un novedoso modelo de alta frecuencia de la máquina eléctrica basado en simulaciones de elementos finitos. Este modelo, validado con varias máquinas industriales, va más allá de la mayoría de los modelos existentes en la literatura, cubriendo un rango de frecuencias de 100 Hz a 50 MHz. El proceso de validación incorpora datos de 28 muestras de una máquina para tener en cuenta las tolerancias de fabricación.

Además, el modelo de alta frecuencia de la máquina se integra en un modelo del accionamiento completo. Este modelo, validado con mediciones experimentales, permite realizar análisis de EMI teniendo en cuenta todos los componentes del accionamiento, incluidos el inversor, el cable y el filtro EMC. A diferencia de los modelos existentes en la literatura que utilizan modelos del motor derivados de mediciones experimentales, el modelo propuesto utiliza datos de impedancia de simulaciones de elementos finitos. Este enfoque permite predecir las corrientes de modo común desde la fase de diseño.

La tesis concluye con un análisis de cómo las variables de diseño influyen en la impedancia de la máquina eléctrica y, en consecuencia, en las corrientes de modo común del accionamiento. Después, introduce una metodología de diseño de máquinas eléctricas que incorpora la perspectiva de EMC. Dos máquinas industriales que superan los límites de la normativa de EMI sirven como casos de estudio. La tesis propone mejoras de diseño que reducen con éxito la corriente de modo común. Este último punto subraya la importante contribución de esta investigación al campo del diseño de máquinas eléctricas y la optimización de la compatibilidad electromagnética.

CONTENTS

LIST OF FIGURES

LIST OF TABLES

NOMENCLATURE

Acronyms / Abbreviations

AC Alternating Current

CISPR International Electrotechnical Commission International Special Committee on Radio Interference

CM Common mode

CMV Common Mode Voltage

CW Circumferential Winding

DM Differential mode

DoE Design of Experiments

DPM Distributed Parameter Model

EMC Electromagnetic Compatibility

EMI Electromagnetic Interference

FEM Finite Element Method

HF High Frequency

IGBT Insulated Gate Bipolar Transistor

IM Induction Machine

IPMSM Interior Permanent Magnet Synchronous Machines

ISO International Standardisation Organization

LISN Line Impedance Stabilisation Network

LPM Lumped Parameter Model

PD Partial Discharge

PMSM Permanent Magnet Synchronous Machine

PWM Pulse Width modulation

SiC Silicon Carbide

TW Toroidal Winding

WBG Wide Band Gap

Greek Symbols

δ Skin depth (m)

$\Delta(f_i)$ Per unit impedance error for the i^{th} frequency

μ_{eff}	Effective permeability
ε	Dielectric Constant
μ''	Imaginary part of the complex permeability
μ	Relative Permeability
μ_{local}	Local Permeability
ω	Pulsation (rad)
Φ	Magnetic Flux (Wb)
γ	Propagation constant
μ'	Real part of the complex permeability
ρ	Volumetric density of an electric charge (C/m^3)
σ	Conductivity ($\Omega \times m$)
μ_0	Permeability of the Vacuum (H/m)

Other Symbols

$\vec{A}$	Magnetic Vector Potential (W/m)
$\vec{B}$	Magnetic Flux Density (T)
C_b	Bearing capacitance
C_{sr}	Stator-to-rotor capacitance
C_{wh}	Winding-to-housing capacitance
C_{wr}	Winding-to-rotor capacitance
C_{ws}	Winding-to-stator capacitance
C_{wsh}	Winding-to-shaft capacitance
$\vec{D}$	Electrical Flux Density (C/m^2)
$\vec{E}$	Electrical Field Strength (V/m)
$\vec{H}$	Magnetic Field Strength (A/m)
$\vec{H}_z$	Magnetic Field within the sheet (A/m)
$\vec{J}$	Current Density (A/m^2)

Chapter 1

INTRODUCTION

This first chapter provides a brief introduction to the thesis framework, the analysis of electromagnetic compatibility in electrical machines. An introduction to this phenomenon and its main issues can be found in the following pages. In addition, the objectives of the thesis are listed in these pages. The outline of the document is also presented with a short description of each chapter. Finally, the papers published during the PhD are shown at the end of the chapter.

1.1 RESEARCH CONTEXT

The United Nations has defined the Sustainable Development Goals as a universal call to action to end poverty, protect the planet, and ensure prosperity by 2030. These goals encompass various aspects of human well-being, including clean energy, sustainable consumption, and climate action [4].

In line with these objectives, the European Commission has set ambitious targets for improving energy efficiency in all sectors, including transportation, industry, and residential. One of the key strategies is to increase the use of energy-efficient technologies and practices, which can significantly reduce energy consumption and greenhouse gas emissions [5].

In the context of sustainable energy, the development and deployment of efficient electrical drives is crucial. These drives, which are used in a wide range of industrial machinery applications, can contribute significantly to energy savings as they account for more than 40% of global electricity consumption [6]. Recent studies have shown that Wide-Band-Gap (WBG) devices, such as those made of Silicon Carbide (SiC), can enhance the performance of these drives by improving power density, dynamic response, and energy efficiency [7].Their high working frequency and low switching losses enable more compact inverter and motor designs with higher efficiency.

However, the use of WBG devices at higher frequencies can lead to Electromagnetic Interference (EMI) problems due to their higher voltage derivatives. These can also affect the robustness of electrical machines and other electronic devices, leading to potential failures. Converters supply electrical machines with frequency and amplitude modulated voltages, which can generate large voltage derivatives. As frequency increases, these derivatives also increase, resulting in higher overvoltages at the motor terminals, which might cause the deterioration of the winding insulation and even cause protection failures in the event of short circuit or contact defects [8, 9].

Furthermore, modulated voltages generate Common Mode Voltage (CMV) that can cause damage to drive components and affect other elements connected to the same network. For example, the voltage induced in the shaft can cause bearing currents, leading to their deterioration [10].

In summary, achieving the Sustainable Development Goals and the energy efficiency targets of the European Commission requires a comprehensive approach that considers not only the development of energy-efficient technologies but also the associated challenges.

Several solutions have been proposed to reduce the effects of undesired CMV in the shaft and bearings. These include the use of insulated or ceramic bearings; applying different conductive greases; and adding Faraday shielding, brushes, or shaft grounding rings [11, 12]. However, these solutions address only the effects of CMV on bearings.

To reduce EMI throughout the electrical machine, shielded cables, along with grounding, are recommended to provide a low-impedance path for the CMV. Various inverters and modulation techniques have been proposed to reduce the generation of CMV from the source [11,13,14]. However, the most commonly used solution to prevent EMI from entering the grid is to add a filter to the drive [15].

Most solutions involve adding components to the drive, which increases its cost, volume, and weight, as well as the complexity of the system. Furthermore, add-ons are typically

included only after Electromagnetic Compatibility (EMC) tests have failed, and corrective actions are required to comply with regulations and bring the product to market.

Therefore, an EMI strategy-based design should be implemented early in the design stage to reduce the cost of the product, improve reliability, and achieve the optimal solution. Thus, understanding and predicting EMI noise using high-frequency models during the design stage is crucial to effectively managing this noise at the device level.

For all of the above, the EMC in electrical machines has drawn the interest of Mondragon Unibertsitatea, which has been doing research on electrical machines for several years and working on an empirical high-frequency electric drive model. The present PhD is a step forward, focused on the design and optimisation of electrical machines from the EMC perspective. To do so, it is necessary to develop a high-frequency model of the machine by other means, such as Finite Element Method (FEM) simulations. The issue is that the empirical models developed so far require measuring the impedance of the machine in order to be modelled by means of lumped parameter models. Obviously, this approach is not feasible at the design stage, since a manufactured machine is not available.

1.2 HIGH-FREQUENCY PHENOMENA IN ELECTRIC DRIVES

A typical electric drive consists of three main elements: the energy source (batteries or the grid), the converter that applies the desired voltage and frequency to the electric machine with different modulation techniques, and the electrical machine. This structure is shown in Figure 1.1.

The diagram illustrates various types of Electromagnetic Interferences (EMI) in the system. Green waves represent radiated EMI that originates from the inverter switching circuits [16]. The red line represents the Differential Mode (DM) EMI, which traverses one phase and returns across other phases to the grid. Lastly, the blue line indicates Common-Mode (CM) EMI, which flows through the common ground, interconnecting all elements with the disturbance [13]. Notably, the modulated voltage pulses generate a common-mode voltage in the motor's input connection, leading to several issues such as leakage currents, shaft voltage, and bearing currents, as discussed in the preceding section. In addition, depending on the characteristics of the cables, overvoltages can occur on the motor terminals, which might affect the life cycle of the insulation systems.

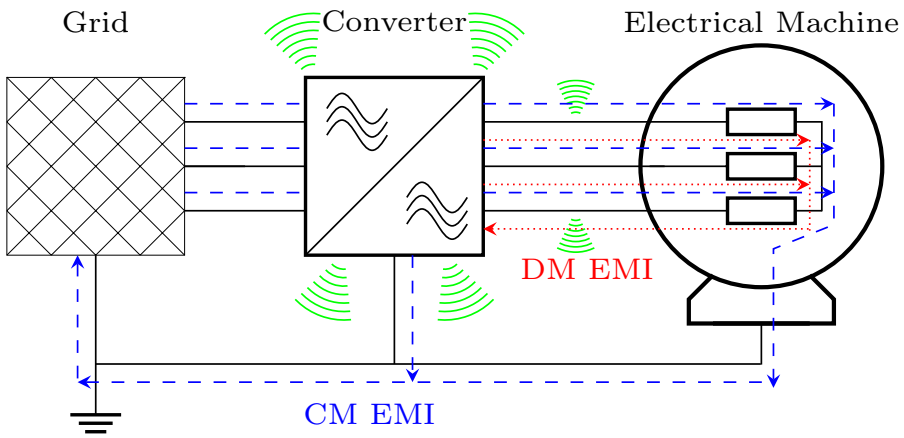

Figure 1.1: Radiated and conducted EMIs in an electric drive.

There are two main types of EMI, depending on the propagating medium: conducted and radiated. This PhD is focused on conducted EMI in both the common and differential modes. These EMI flow through the wires from the source of interference (the inverter) to a susceptible receiver, which could be the motor or any electrical device connected to the system or the power grid. The other type of EMI is the radiated one, which propagates through the environment if there is a cable acting as an antenna [16].

1.3 EMC STANDARDS FOR ELECTRIC DRIVES

EMC standards are established to ensure that systems can operate effectively within their electromagnetic environment without causing unacceptable electromagnetic disturbance to any element within that environment.

Although different standards are established depending on the application of the equipment or even the geographical location, the main regulation for measuring the emission characteristics of industrial equipment is the European standard EN 55011 [17]. Specific limits for lifts and walking steps are also defined in EN 12015 [18]. In these regulations, limits are set for voltage emissions, both in the Alternating Current (AC) main supply connection and in the machine connections, as these disturbances are usually amplified by the power cables used in the drives.

There are two main limits, the average emission limit and the quasi-peak limit. These limits are usually given in dBμV and there are different limits depending on the frequency, which ranges from 150 kHz to 30 MHz. For higher frequencies up to 1 GHz, the radiated emissions are analysed, but these are outside the scope of this work.

In order to pass the EMC test of the AC power port, a filter is usually included, as emissions around 1-4 MHz are typically above the limit. Therefore, to reduce the cost of the product and increase its reliability, an EMI strategy-based design should be added early in the product development cycle to reduce costs and achieve the best solution. Consequently, understanding and predicting EMI noise using High-Frequency (HF) models during the design phase is essential to manage EMI problems at the device level. This is the main objective of this thesis.

1.4 HYPOTHESES AND OBJECTIVES

The main objective of the thesis is to establish the design rules that make it possible to improve the high-frequency behaviour and robustness of electrical machines, and indeed the high frequency performance of the overall electrical drive.

1.4.1 Hypotheses

For accomplishing the main objective, some hypotheses must be defined, analysed, and solved. Next, the main hypotheses are summarised:

H1. By adjusting the high-frequency behaviour of the electrical machine, the performance of the whole electric drive should be improved.

H2. By modifying the motor impedance, the lifetime of the bearings and the winding insulation would be increased, preventing unexpected and premature failures.

H3. Knowledge of the high-frequency behaviour of electrical machines and the use of appropriate tools and methodologies for analysis and design could make possible the optimisation of the electric drive for each particular application.

H4. Prototyping the electric drive with an optimised electrical machine would allow to evaluate the effectiveness and usefulness of the developed design methodology and tools, as well as the improvements obtained with respect to a conventional electrical machine.

1.4.2 Objectives

The main objectives associated with the previous hypotheses are the following.

O1. Reduce the EMI of the whole electric drive, without adding a filter by reducing the common mode current in the grid connection point.

O2. Increase the reliability and robustness of the drive by reducing the common-mode current and overvoltages in the motor terminals.

O3. Define a design methodology that also improves the high-frequency behaviour of electric machines.

O4. Demonstrate the validity of the design tools and methodology in a practical case study by manufacturing and evaluating a prototype.

Next, some actions are defined to achieve the objectives described above:

A1. Definition of experimental procedures to conduct high-frequency measurements.

A2. Development of high-frequency analysis tools.

A3. Identification of design parameters that influence the high-frequency behaviour of the electrical machine.

A4. Development of a new electrical machine design with improved EMC behaviour and increased reliability.

1.5 PUBLICATIONS

The following contributions have been made during the PhD.

1.5.1 Journal Articles

PUBLICATION 1: Reference [1]

"Analysis of Permanent Magnet Motors in High Frequency—A Review"

Y. Moreno, G. Almandoz, A. Egea, B. Arribas and A. Urdangarin

Applied Sciences, vol. 11, no. 14, p. 6334, Jul. 2021, doi: 10.3390/app11146334.

Abstract: Electric drives consume a great amount of the world's energy, and it will keep increasing due to the electromobility trend. Thus, the efficiency of electric drives must be improved to reach the desired sustainability goal. The Silicon Carbide devices contribute to this objective due to their high working frequency and lower switching losses. However, working at higher frequencies may bring serious Electromagnetic Compatibility (EMC) problems, as well as insulation stress and higher bearing currents. Hence, it is important to have an electrical machine electrical equivalent circuit model to predict the electromagnetic interference levels. This review summarizes the current state of the art in electrical machine modeling and analysis in high frequency. The main analysis tools as Finite Element Methods, analytical and measurement-based tools are compared in their application to high-frequency electrical machine analysis. Then, different machine high-frequency models are reported, detailing their individual features. Additionally, the influence of the machine design parameters on EMC behavior is outlined for future analysis. All in all, Finite Element analysis is the most accurate tool for high-frequency analysis, provided that the mesh size is thinner than the skin depth. It is also concluded that the winding placement is an essential parameter to define the high-frequency behavior of the machine.

PUBLICATION 2: Reference [2]

"High-Frequency Modelling of Electrical Machines for EMC Analysis"

Y. Moreno, A. Egea, G. Almandoz, G. Ugalde, A. Urdangarin and R. Moreno

Electronics, vol. 13, no. 4, p. 787, Feb. 2024, doi: 10.3390/electronics13040787.

Abstract: The trend towards electrification in mobility has led to the increased use of silicon carbide (SiC) semiconductors. These semiconductors are more efficient but also present challenges related to electromagnetic interference (EMI) due to their higher voltage derivatives. This paper introduces a new high-frequency impedance model for electrical machines. The proposed model distinguishes itself from existing approaches by being entirely derived from Finite Element Method (FEM) simulations, which include capacitances in the magnetic simulation. This approach achieves a balance between computational efficiency and high accuracy across the entire frequency spectrum, ranging from 100 Hz to 50 MHz. The model provides valuable insights during the design phase and was rigorously validated using data from 28 samples of an industrial machine.

1.5.2 Conference Proceedings

PROCEEDINGS 1: Reference [3]

"High-Frequency Modelling of Windings" Y. Moreno, A. Egea, G. Almandoz, G. Ugalde, A. Urdangarin, and R. Moreno

in 2022 International Conference on Electrical Machines (ICEM), Sep. 2022, pp. 1232–1238, doi:10.1109/ICEM51905.2022.9910696.

Abstract: Electrical drives consume a great amount of the world's energy, and this will keep increasing due to the electromobility trend. Hence, the efficiency of electrical drives must be improved to reach sustainability. Silicon Carbide devices have a high working frequency and lower switching loss, increasing the device efficiency. Nevertheless, higher operation frequencies may bring major Electromagnetic Compatibility issues, in addition to insulation stress and higher bearing currents. This paper presents the simulation process to obtain a high-frequency model of an electrical machine. Then, some small and controlled coils are modelled to construct the high-frequency model step by step, analysing the slight differences between conductor diameters and materials that would be difficult to see in a machine. These models are validated with experimental impedance measurements. This represents the first step in modelling an electrical machine equivalent circuit to predict the electromagnetic interference levels from the design stage.

1.6 OUTLINE OF THE DOCUMENT

CHAPTER 1
The first chapter provides a rough view of the thesis. Motivation, hypotheses, and objectives are presented and the framework of the thesis is presented. The outline of the document is given, and finally, the published papers are presented.

CHAPTER 2
In the second chapter, a thorough analysis of the state-of-the-art is conducted. First, the high-frequency phenomena are explained. Then, the different analysis tools and models used to analyse the machines at high frequency are described. Finally, the influence of different design parameters on the high-frequency behaviour of electrical machines is presented.

CHAPTER 3
The overall process for obtaining a high-frequency impedance model with Finite Element simulations is presented. The model is validated using measurements from 28 industrial machines, taking into account manufacturing tolerances. The complete model of individual conductors is described and compared to a simpler alternative based on bulk coils. The validation process starts with a single coil and culminates in the complete machine.

CHAPTER 4
The machine is integrated into the complete electric drive system. Initially, the modelling technique for each component is introduced. Then, the entire drive system is validated by examining the common-mode voltage and currents. The impact of the machine on the common-mode current in the grid is then assessed. Lastly, the EMC filter is integrated into the system.

CHAPTER 5
In order to change the CM impedance of the electrical machine, different design variables can be modified. In this chapter, an analysis is carried out to set some design specifications to decrease the CM currents of the electrical drive. Then, those design specifications are introduced into the general design methodology of an electrical machine. Finally, a case study with two industrial machines exceeding the EMI regulation limits is presented. The proposed design improvement successfully reduces their common-mode current.

CHAPTER 6
The conclusions of the work done during the PhD are described, identifying future research challenges and opportunities.

Chapter 2

STATE OF THE ART

When working at high frequency, there are different phenomena that must be taken into account because they affect the behaviour of the electrical machine. In this chapter, these phenomena are explained first. Then, the current state of the art of the high-frequency analysis tools for electrical machines is described. Later, different techniques for modelling electrical machines at high frequencies are depicted based on the literature. Finally, the influence of different design parameters on the high-frequency behaviour of electric motors is presented. Part of the work presented in this chapter was published as a review article in [1].

2.1 HIGH FREQUENCY PHENOMENA

In low-frequency operation, parameters such as resistance and inductance exhibit minimal dependency on frequency, making them essentially constant. However, at higher frequencies, new phenomena emerge that cause variations in these parameters. Consequently, as the frequency increases, the resistance increases as well, while the inductance decreases.

2.1.1 High-Frequency Phenomena in Conductors

As the frequency increases, the skin effect becomes prominent as one of the primary phenomena. This effect arises because of the induced eddy currents within the current-carrying conductor that are generated by the self-generated high-frequency magnetic field. These eddy currents, in turn, create a non-uniform distribution of current density within the conductor, pushing electrons towards the outer regions. Consequently, the effective cross section available for current flow is reduced, as the current tends to flow predominantly within a thin layer known as the skin depth (illustrated in Figure 2.1).

The skin depth can be determined using the well-known analytical expression:

$$\delta = \sqrt{\frac{2}{\omega \mu \sigma}} \tag{2.1}$$

Here, δ represents the skin depth, ω denotes the current pulsation, μ signifies the medium's permeability, and σ stands for the conductivity of the material. Notably, according to Equation (2.1), it is evident that the skin depth decreases as the frequency increases, indicating that higher frequencies result in thinner skin depths.

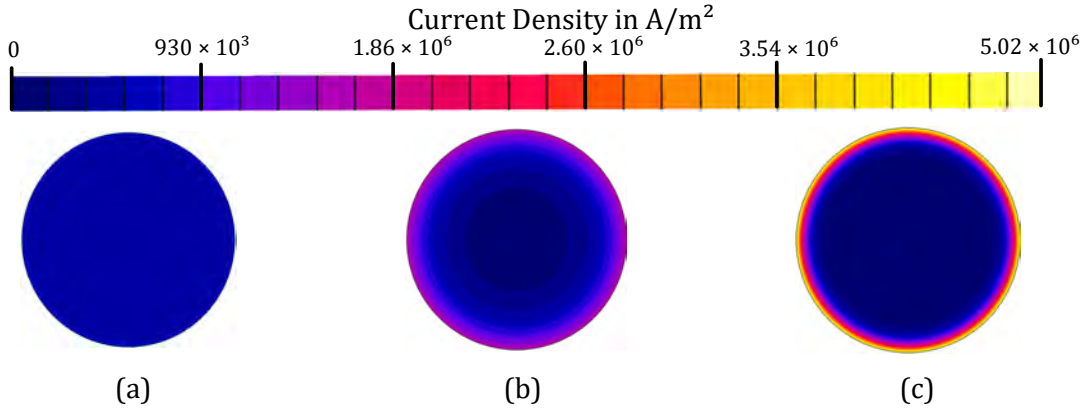

Figure 2.1: Skin effect in a conductor of 2 mm of diameter. (a) 1 kHz. (b) 100 kHz. (c) 1 MHz.

The current distribution on the surface causes higher resistance and lower inductance because of the way the magnetic flux is spread within the conductor. The skin effect is specific to each conductor and is not influenced by neighbouring conductors, allowing for the analysis considering a single conductor [19, 20]. To mitigate this effect, a conductor diameter smaller than the skin depth can be used, considering its dependence on frequency and geometry.

The interaction between the conductors that form a coil is known as the proximity effect, which has a greater impact compared to the skin effect [21]. Although similar in nature to the skin effect, the proximity effect involves the induction of eddy currents in a

conductor due to the high-frequency magnetic field generated by neighbouring conductors. Consequently, this phenomenon hinges on the relative positioning of the conductors and can be mitigated by employing windings with twisted strands or Litz wires. However, while effective, these solutions introduce manufacturing complexities and can result in an uneven current distribution between the strands [22]. The influence of proximity effect on the distribution of the current density within an electrical machine coil is illustrated in Figure 2.2. When these effects combine, the effective cross-sectional area of a wire further diminishes, leading to a subsequent increase in resistance [23, 24].

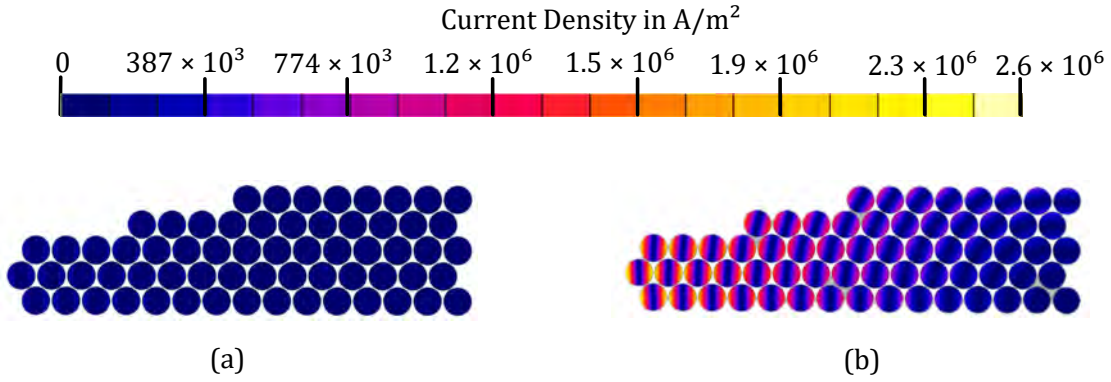

Figure 2.2: Proximity effect on conductors of an electric motor coil. (a) 1 kHz (b) 10 kHz.

2.1.2 High-Frequency Phenomena in Magnetic Cores

Regarding the magnetic core of electric machines, there are high-frequency phenomena in this domain that can greatly impact the motor's performance. Typically, the magnetic cores of the stator and rotor are constructed by laminated electrical steel sheets to minimise the eddy currents caused by alternating magnetic fields. In this way, magnetic losses can be significantly reduced. However, at higher frequencies, the effect of eddy currents is notably increased, even with the insulation of the lamination, as the skin depth becomes smaller than the thickness of the sheet.

Induced eddy currents produce a shielding effect within the electrical sheets, which forces the magnetic flux out of the ferromagnetic core. This results in a reduction in the relative permeability of the magnetic material and consequently in the inductance value [21, 23, 25]. The frequency threshold for this change is based on the thickness of the individual steel sheets and their resistivity [23, 24, 26].

In [24], a two-dimensional model is developed to replicate a bulk ferromagnetic core, while a three-dimensional model is used to depict a laminated ferromagnetic core. In the scenario of the laminated core, the inductance reduction is less pronounced compared to the bulk core due to the incomplete expulsion of magnetic flux from the laminations. In contrast, resistance experiences a more significant increase in the laminated core due to the larger surface area for eddy current circulation and the increased proximity effect between the laminated sheets, which amplifies the eddy currents within the core. It is important to mention that the simulations do not consider the non-linear magnetic saturation of the ferromagnetic core or the displacement current term, which is deemed insignificant, especially below 1 GHz [24].

2.1.2.1 *Complex Permeability*

As mentioned previously, eddy currents arise in the core as a result of the conductivity of the ferromagnetic material. The primary approach for simulating these currents and their impacts is through the frequency-dependent effective complex relative permeability [23, 27, 28]. This is obtained by simplifying Maxwell's equations within the laminated sheet to a one-dimensional scenario. Although a detailed explanation will be provided for clarity, a comprehensive discussion can be found in [28–30].

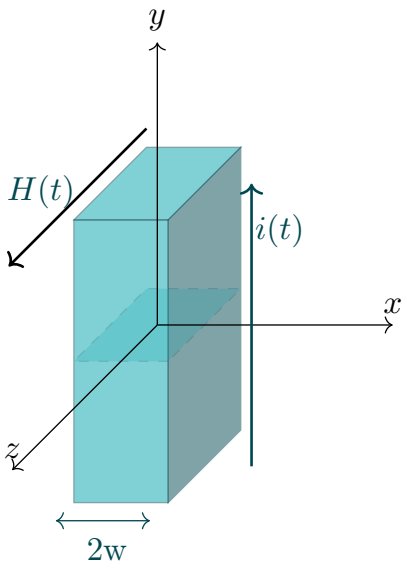

Figure 2.3: Single laminated sheet

Considering a single rectangular laminated sheet as in Figure 2.3, assuming that the current is in the y direction, the magnetic field is the following:

$$\frac{\partial^2 H_z(\mathrm{x},t)}{\partial \mathrm{x}^2} = \frac{\partial H_z(\mathrm{x},t)}{\partial t} \tag{2.2}$$

Solving Equation (2.2) results in two waves in the opposite direction:

$$H_\mathrm{z}(\mathrm{x},t) = C_1 e^{j\omega t - \gamma \mathrm{x}} + C_2 e^{j\omega t - \gamma \mathrm{x}} \tag{2.3}$$

Given that the propagation constant is specified as: $\gamma = \frac{1+j}{2\delta} = \sqrt{j\omega\mu\sigma}$, where σ and μ represent the local conductivity and permeability, respectively. Under the assumption of symmetrical boundary conditions on both sides of the sheet, the magnetic field within the sheet can be expressed as:

$$H_\mathrm{z}(\mathrm{x},t) = \frac{H_0}{1+e^{-\gamma \mathrm{w}}}(e^{j\omega t - \gamma(\mathrm{x}+\mathrm{w})} + e^{j\omega t - \gamma(\mathrm{x}-\mathrm{w})}) \tag{2.4}$$

The magnetic flux density can be determined by the following expression:

$$\langle B_\mathrm{z} \rangle = \frac{1}{A_{cross}} \int_{-\mathrm{w}}^{\mathrm{w}} \mu H_\mathrm{z}(\mathrm{x},t) \Delta y \, dx = \frac{H_0 e^{j\omega t}\mu}{\gamma} \tanh(\gamma \mathrm{w}) \tag{2.5}$$

where A_{cross} denotes the cross-section area of the sheet. Subsequently, the effective permeability μ_{eff} in the z-direction of the laminated sheet can be computed as:

$$\mu_{eff} = \frac{\langle B_z \rangle}{\mu_0 H_z^{ext}} = \mu_{local} \left(\mu'(f) - j\mu''(f) \right) \tag{2.6}$$

where H_z^{ext} is the external field and μ_0 is the permeability of the vacuum. Local permeability can be estimated using an optimisation algorithm [30].

Finally, in the next equation 2.7, μ' is the real part of the complex relative permeability, representing the energy stored in the core, while the imaginary part (μ'') represents the losses of the core.

$$\begin{cases} \mu'(f) & = \mu_{local} \frac{\delta}{\mathrm{w}} \left(\frac{\sinh(\mathrm{w}/\delta) + \sin(\mathrm{w}/\delta)}{\cosh(\mathrm{w}/\delta) + \cos(\mathrm{w}/\delta)} \right) \\ \mu''(f) & = \mu_{local} \frac{\delta}{\mathrm{w}} \left(\frac{\sinh(\mathrm{w}/\delta) - \sin(\mathrm{w}/\delta)}{\cosh(\mathrm{w}/\delta) + \cos(\mathrm{w}/\delta)} \right) \end{cases} \tag{2.7}$$

The phasor relationship between the $\vec{H}$ field and the two components of $\vec{B}$ can be seen in Figure 2.4. As mentioned above, the real part represents the inductive energy stored in the magnetic material, whereas the imaginary part represents the losses. The resulting $\vec{B}$ phasor forms an angle with $\vec{H}$ (α) that is called the loss angle of the material.

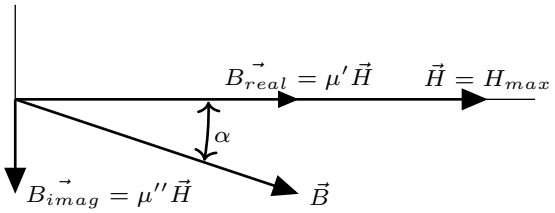

Figure 2.4: Phasor relationship between B and H for a complex permeability material [29].

2.1.3 Parasitic Capacitances

At low frequencies, parasitic capacitances usually have minimal impact because of their high impedance. However, as the operating frequency increases, the impedance of these capacitances decreases, establishing new circulating paths for currents inside the motor. This alteration can significantly influence the impedances in differential and common mode, together with the currents in differential and common mode in the motor [23, 31–33].

The primary parasitic capacitances present in an electric motor are illustrated in Figure 2.5a. These include C_{wr} (winding-to-rotor capacitance), C_b (bearing capacitance), C_{ws} (winding-to-stator capacitance), C_{sr} (stator-to-rotor capacitance), C_{wh} (winding-to-housing capacitance) and C_{wsh} (winding-to-shaft capacitance).

Within the winding, various capacitances emerge. Among them, C_{ij} represents the interturn capacitance, while C_{pp} denotes the capacitance between phases, which may be ignored if the winding comprises a single-layer configuration [23]. The comprehensive paths for common-mode (CM) currents are identified in [32]. Accurate calculation of interturn capacitances requires examining some factors such as conductor geometry, type and properties of materials, positioning within the slot, and insulation thickness [34, 35].

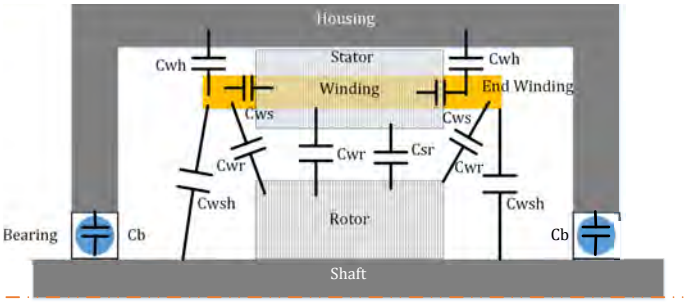

(a)

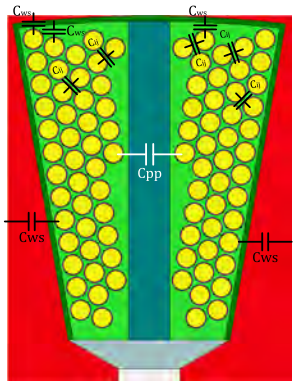

(b)

Figure 2.5: Parasitic capacitances. (a) Motor view. (b) Winding turns.

2.2 ANALYSIS TOOLS

Lumped Parameter Models (LPM) are commonly used to represent the behaviour of electrical machines at high frequencies. There are two primary approaches to define the values of these parameters. The first approach involves determining the LPM parameters of the motor through experimental measurements, which is widely used in the literature [26, 31, 36–58]. This method is practical and enables accurate EMC simulation of motor drives. However, it requires the disposal of a real motor for the measurements, making it unsuitable for the preliminary design phase prior to prototyping.

In the second approach, a corresponding circuit model known as LPM is constructed to determine each circuit constant using the motor design parameters through analytical methods [34, 59–72], Finite Element Method (FEM) [21, 23–25, 27, 28, 31, 35, 61, 73–86], or a combination of both, known as hybrid methods [32, 87, 88]. Through FEM-based electromagnetic field analysis, the inductance, resistance, and capacitance of each winding turn can be determined, which are difficult to measure experimentally [24]. This section delves into the primary tools used for calculating the parameters of the equivalent circuit.

2.2.1 Finite Element Methods

FEM is based on the fundamental laws of electromagnetism that are Maxwell's equations. In (2.8), based on Gauss's law, it relates the volumetric density of an electric charge (ρ) with the electrical flux density ($\vec{D}$). Faraday's law (2.9) relates the electrical field strength ($\vec{E}$) to the time-varying magnetic flux density ($\vec{B}$). Then the Gauss law for electromagnetism states that the flux across any closed surface is always zero, whatever the field and the surface are(2.10). Finally, in Maxwell-Ámpere's law (2.11) it relates the magnetic field strength ($\vec{H}$) with the current density ($\vec{J}$) and the electrical flux density ($\vec{D}$) [89, 90]. The time varying of the flux density is the displacement current term that is neglected below 1GHz. In the analysis proposed in this thesis, this term will be neglected because the frequency range of interest is below 30 MHz.

$$\nabla \cdot \vec{D} = \rho \tag{2.8}$$

$$\nabla \times \vec{E} = -\frac{\partial \vec{B}}{\partial t} \tag{2.9}$$

$$\nabla \cdot \vec{B} = 0 \tag{2.10}$$

$$\nabla \times \vec{H} = \vec{J} + \frac{\partial \vec{D}}{\partial t} \tag{2.11}$$

To solve those equations in FEM magnetic application, the magnetic vector potential ($\vec{A}$) is used, solving Equation (2.12), where v_0 is the reluctivity of vacuum, v_r and σ are the reluctivity and conductivity of the medium and and V is the electric scalar potential. In this solution, only ($\vec{E}$), ($\vec{B}$) and ($\vec{H}$) are computed, since the ($\vec{D}$) field is not used in magnetic applications. Moreover, solving Equation (2.12) decouples the equations of the electric and magnetic fields. This decoupling depends on the materials, the frequency, and the dimension of the study domain, being suitable for frequencies below 10 GHz.

$$\nabla \times \left(v_0 \left[v_r \right] \nabla \times \vec{A} \right) + \left[\sigma \right] \left(\frac{\partial \vec{A}}{\partial t} + \nabla V \right) = 0 \tag{2.12}$$

2.2.1.1 *Analysis of eddy Currents and Iron Losses*

Iron losses in electrical machines are well known to be frequency dependent, with both hysteresis and eddy currents increasing as the frequency increases. Accurate modelling of these losses often requires the consideration of the non-linear permeability of the magnetic core [21, 77]. In [21], non-linear permeability is incorporated by assigning different permeability values to various regions based on the flux density vector, with mesh element sizes set below the wavelength of the Pulse Width modulation (PWM) excitation frequency. This approach effectively accounts for the non-linearity of the magnetic material's BH curve. Conversely, a linear approximation of the BH curve is proposed in [23], giving precise results.

Although explicit methodologies for calculating hysteresis and excess losses may not always be delineated in high-frequency motor models found in the literature, [91] introduces an improved core loss model for transformers and machines, validated up to 1.6 kHz under high-frequency and non-sinusoidal supply conditions.

In terms of model geometry, 2-D models often overlook two critical effects: lamination of the magnetic core and end effects. Consequently, 2-D models tend to overestimate the shield effect in sheets, leading to underestimated iron loss, reduced coil inductance, and increased resistance [24, 83]. Addressing this limitation, [78] incorporates the lamination effect in 2-D models through an equivalent conductivity approach. Initially, 3-D laminated and bulk core simulations are conducted, adjusting the conductivity of the bulk core to match the eddy losses of the laminated core. The impact of lamination on the magnetic flux distribution can be observed in Figure 2.6a. Furthermore, Figure 2.6b demonstrates the end effect, where the end-winding leakage flux induces a local elevation in the flux density at the edge of the tooth-shoe region, resulting in additional core losses [22].

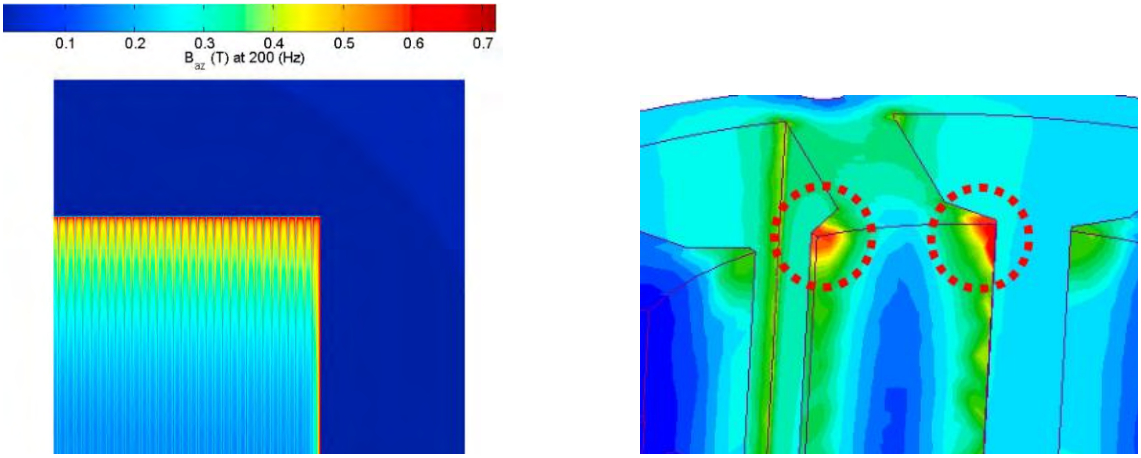

(a) (b)

Figure 2.6: Illustration of iron sheet effects. (a)Lamination effect [92]; (b) End effect [22].

Moreover, since the stator serves as a CM current path at high frequencies, its impedance must be carefully determined. In [92], the impedance of electrical sheets is computed for high-frequency transformers, encompassing both the parallel and perpendicular axes to the winding.

2.2.1.2 *Analysis of Coil Conductors*

In low frequency FEM analysis, it may be sufficient to represent winding coils as bulk coils, as important performance measures such as joule losses or torque capacity generally do not depend on the frequency of the power supply. However, as frequencies increase, detailed modelling of the winding and finer mesh becomes imperative due to nonuniform current distribution stemming from skin and proximity effects. To achieve accurate results, the mesh size must be smaller than the skin depth at the given frequency [79]. Hence, solving such intricate problems may substantially escalate the computational burden, making it necessary to address simplification strategies to strike a balance between computational load and result accuracy. Several approaches aimed at achieving this balance are explored in the literature.

In [88,93], four distinct FEM models for axial high-speed Permanent Magnet Synchronous Machines (PMSM) are evaluated, including bulk coils and individual conductors with fine mesh in the 2D and 3D domains. The complete 3-D model, which incorporates the end windings, is the most accurate to calculate AC losses in coils, as it accounts for end, skin, and proximity effects. In contrast, bulk-coil models typically overlook these effects. In particular, even with fine mesh, 2-D models often underestimate AC copper losses [83].

To mitigate computational demands while maintaining accuracy, three methodologies are proposed:

- In [88], a bulk coil 3-D model with coarse mesh is advocated for calculating magnetic flux density. Analytical formulations are then applied to estimate AC copper eddy current losses, disregarding skin and proximity losses. This method finds relevance in coreless permanent magnet machines, where most AC copper loss is due to the interaction of the magnetic flux with the conductors [88].
- [93] suggests a 2-D model with detailed conductors and fine mesh, supplemented by coefficients derived from flux density variation along the machine's active length in a coarse mesh 3-D model to adjust for losses along end windings.
- [87] proposes calculating flux density for various layers of the conductors, followed by an analytical calculation of the AC loss for the radial flux machines. In cases where skin depth is less than the conductor radius, flux density is computed at different points within each conductor [87].

Table 2.1 provides an overview of different approaches for analysing the electromagnetic behaviour of electrical machines by simulation. Most models incorporate the rotor, while end winding inclusion is primarily limited to 3-D models. Meshes, where specified, typically exhibit a size smaller than the skin depth at the analysed frequency to accurately capture skin and proximity effects.

In some instances, the ferromagnetic core properties are simply mentioned without further elaboration. However, the majority of cases include iron losses and even the lamination effect, typically employing 3-D models or equivalent 2-D models. Modelling approaches vary, with some models incorporating complex permeability and nonlinear BH curves, while others choose to use a constant permeability.

Table 2.1: FEM Electromagnetic simulation comparison.

Case	Frequency Range	Geometry	Mesh	Rotor Model	End Winding	Skin Effect	Proximity Effect	Iron Core
[32]	30–5 M	3-D.1 slot.		x	x [94]		(Bulk turn)	R_{core} & L_{core} [1] [70]
[35] [2]	100–100 M	2-D.1/8 Model.		x		x	x	-
[78]	20–4 M	2-D.1/4 Model.		x			(Bulk turn)	Equivalent σ
[21,95]	10 k	2-D.1/2 Model	$< \delta$	x		x	x	Nonlinear BH
[23]	100–1 M	2-D slot		x		x	x	Complex μ. Linear BH
[77]	0–100 k	2/3-D		x	x	x	x	nonlinear BH and losses
[61]	10–10 M	2-D.1 slot		x		x	x	x
[73]	1 k–10 M	2-D.1 slot				x	x	Constant μ, No lamination
[24]	10 k–20 M	3-D.3 slot	$< \delta$		x	x	x	Constant μ. One sheet
[28]	0–10 M	2-D.1 slot	$< \delta$			x	x	Coreless
[84]	0–200 k	2-D.1 slot	$< \delta$			x	x	x
[87]	0–800	2-D Full	$< \delta$	x		x	x	
[88]	500–3 k	3-D.3 coils	Some $< \delta$	x	x			Coreless
[93]	0–333	2-D. Half	Fine		x	x	x	
[22]	0–1.4 k	3-D.1 Phase	Fine		x	x	x	nonlinear BH and losses
[83]	0–600	2-D.1 pole		x		x	x	
[27,96]	10 k–1 M	2-D.1 slot	$< \delta$			x	x	Complex μ. One sheet
[86,97]	1 k–30 M	2-D	$< \delta$			x	x	Effective permeability
[98]	20 k–4 M	2-D/3-D	$< \delta$	x	x	x	x	3-D

[1] Analytical equations are used. [2] Rotor position is taken into account for R and L calculations.

All the cases reported in the table work on the high-frequency behaviour of electric machines, but the ones on the lower section of the table focus primarily on extracting AC copper losses for high-speed PMSM, not in the general behaviour of the machine.

2.2.1.3 *Parasitic Capacitances*

At high frequencies, the presence of parasitic capacitances among different components of the machine leads to additional current paths, impacting the motor's behavior significantly. Thorough analysis of these capacitive couplings is essential, requiring the use of electrostatic FEM simulations [21,31,99].

Various techniques are available to determine the capacitances between the conductors, as detailed in [100]. In electrical machinery, these conductors may refer to the winding conductors, as well as the stator and rotor cores, which also function as coupling paths. The following are the most commonly used approaches [82]:

- Minimum Energy Method: The procedure involves conducting $N(N+1)/2$ simulations, where N represents the number of regions to be evaluated. Subsequently, the stored energy will be determined based on the electric field value. An efficient approach to determining the self-capacitance coefficients C_{ii} is to perform N simulations, where all conductors except the one whose capacitance itself is computed are assigned a boundary condition $V_j = 0$ for $j \neq i$. The equation (2.13) is then solved, with W_i representing the stored energy and V_i denoting the applied voltage. To evaluate the mutual capacitance between two regions C_{ij}, the boundary conditions $V_j \neq V_i \neq 0$ are specified, while the remaining regions are set to zero.

$$C_{ii} = 2\frac{W_i}{V_i^2} \quad C_{ij} = C_{ji} = 2\frac{W_{ij} - 0.5(C_{ii}V_i^2 + C_{jj}V_j^2)}{V_i V_j} \tag{2.13}$$

- Gauss law method: It consists of performing N simulations in which the conductors are defined with a boundary condition $V_k = 0$ for $k \neq j$. Then, after solving the electric field distribution in each simulation, the expression (2.14) is applied, where Q_{ij} is the charge of each conductor due to the voltage excitation. $(N+1)/2$ simulations are enough, so the number of simulations required is significantly reduced. Hence, this method can be considered more suitable than the minimum energy method for electrical motors, which normally use coils comprising a rather high number of conductors.

$$C_{ij} = 2\frac{Q_{ij}}{V_j} \tag{2.14}$$

Concerning the model's geometry, the capacitances of the active section of the machine can be computed using 2-D FEM electrostatic simulations, while the capacitances of the end-windings require 3-D FEM simulations [32, 94]. It is important to note that the capacitive interaction between the active part of the stator winding and the stator core is notably larger than other capacitive interactions, making it the primary path for the CM current. Therefore, in certain scenarios, 2-D FEM simulations are sufficient to analyse this primary CM current path [23]. Nevertheless, the end winding accounts for up to 40% of the total capacitance between the winding and the rotor, affecting the phase-to-phase capacitance, and thus, it is crucial to include it for the precise assessment of the bearing currents [35, 101]. However, as mentioned before, it can be neglected for the calculation of capacitance between windings and the stator core.

Furthermore, the capacitances between turns and between turns and the stator contribute to forming a symmetric matrix $N \times N$, where N represents the number of turns, as illustrated in Eq. (2.15). Here, C_{ij} denotes the capacitance between the ith and jth turns, and C_{ii} represents the capacitance between the ith turn and the core [27, 61, 64, 73, 75, 78]. Additionally, in references [21, 24], the concept of phase-to-phase capacitance is introduced for windings with multiple layers.

$$[C] = \begin{pmatrix} \ddots & -C_{ij} & \cdots \\ \cdots & C_{io} + \sum_{j=1}^{Nc} C_{ij} & \cdots \\ \cdots & -C_{ji} & \ddots \end{pmatrix} \tag{2.15}$$

In [82], the importance of the mesh arrangement among the conductors is emphasised, suggesting the definition of a minimum of two mesh layers between the conductors to ensure precise results. The authors point out that the calculated matrix reveals that the most significant connections usually occur between adjacent turns and those in front of the stator core. They propose simplifying the matrix by disregarding insignificant values of remote conductors, a strategy also mentioned in [73].

Table 2.2 presents a summary of the models analysed, detailing their objectives and considered capacitive couplings. Notably, the winding-to-stator capacitance is commonly included in all cases, except for one that focuses on the impact of the end winding on bearing currents. In this instance, the winding-to-rotor coupling takes precedence. Nevertheless, certain publications choose to adopt a more straightforward method of considering winding-to-ground capacitance instead of winding-to-stator capacitance, simplifying the models.

It is noteworthy that, in most cases, turn-to-turn capacitances are accounted for, particularly in the analysis of transient voltages. Interestingly, when it comes to the common and differential mode impedances of electrical machines, the influence of the rotor

Table 2.2: FEM Electrostatic comparison.

Case	Experimental Validation	Geometry	Rotor Model	End Winding	Winding Stator	Winding Rotor	Bearing Capacitor	Stator Rotor	Turn Turn
[32]	Bearing Current	3-D.1slot.	x	x	x	x	x		
[94]	CM	2-D/3-D.1/4 Model.	x	x	x	x	x	x	
[35]	CM & DM	2-D.1/8 Model.	x		x	x		x	x
[78]	CM	2-D.1/4 Model.	x		x				(bulk)
[21,95]	Over-voltage	2-D.1/2 Model	x		[1]				x
[23]	CM & DM	2-D slot	x	[2]	x	x			x
[77]	Over-voltage	2/3-D	x	x	[1]				x
[61]	Over-voltage	2-D.1 slot	x		[1]				x
[73]	CM	2-D.1 slot		[2]	[1]				x
[24]	CM & DM	3-D.3 slot		x	x				x
[28]	CM	2-D.1 slot			x				x
[84]	RL	2-D.1 slot		x	[1]				x
[76]	Capacitance	2-D 1-slot			x				
[82]		2-D 1-slot			x				x
[101]	Bearing Currents	3-D Full	x	x		x	x	x	
[27,96]	CM & DM	2-D 1 slot			x				x
[97]	CM & DM	2-D 1 slot			x				x

[1] Winding to ground. [2] Analytical equations are used.

may not be significant as only a few models consider it. Therefore, for the CM impedance calculation, the end windings are neglected. However, in all cases where bearing currents and overvoltages are examined, the rotor is taken into account.

2.2.2 Analytical Tools

When it comes to analytical methods, certain assumptions and simplifications are often necessary to compute the resistance, inductance, and capacitance values using manageable formulas. Although these simplifications may result in less precision compared to FEM simulations, analytical calculations typically require significantly lower computational resources. This section provides a summary of various analytical approaches found in the literature.

2.2.2.1 *Analysis of the Magnetic Core*

On the one hand, as the frequency increases, eddy current losses escalate within the ferromagnetic core. In the study presented in [62], it is assumed that the eddy currents are confined to the skin depth, which leads to a uniform current density throughout it. Consequently, with parameters such as stator length, resistivity, and slot perimeter, the resistance attributed to iron loss due to eddy currents is derived for integration into the circuit model.

On the other hand, [59] considers that the resistance associated with core losses at low frequencies is proportional to the power of the induction machine. In addition, empirically estimated damping resistance is introduced in parallel with winding inductance to account for high-frequency iron loss coupled with winding skin and proximity effects. This resistance is essential because of its impact on the differential mode impedance at the primary resonance frequency.

References to hysteresis or excess loss are scarce, except for the model proposed in [68], which adopts Bertotti's estimation method for iron losses. However, the resultant common-mode and differential-mode currents lack of experimental validation.

Furthermore, in [69, 70], the authors investigate the common-mode impedance of the stator. They propose that when a common-mode current flows through the stator, it induces a circumferential flux within the stator yoke. These currents and fluxes propagate along the iron surface at the skin depth. In their research, they considered the magnetic flux in each lamination to be the sum of the flux generated by the current within that lamination and the current flowing in the adjacent lamination. Assuming equal currents traverse each of the N laminations, the core impedance can be expressed as depicted in (2.16), where r_1 and r_2 denote the inner and outer diameters of the stator yoke, respectively.

$$Z_c = (1+j)\frac{N}{3\pi\sigma\delta}\ln\frac{r_2}{r_1} \tag{2.16}$$

2.2.2.2 *Analysis of Coil Conductors*

At high frequencies, windings experience skin and proximity effects, as detailed in Section 2.1.1. The skin effect can be quantified using Equation (2.17), where L represents the winding length, r denotes the radius of the conductor and δ signifies the skin depth defined in Equation (2.1).

$$R_{skin} = \frac{\rho L}{A_{eff}} = \frac{\rho L}{\pi r^2 - \pi(r-\delta)^2} \tag{2.17}$$

For instance, in [62], the analysis of a single coil in an electrical machine is in agreement with the experimental measurements. However, when examining a group of coils, the resistance increases significantly as a result of the unaccounted proximity effect in the model, thereby compromising its accuracy.

Estimating the proximity effect analytically poses a challenge. The most prevalent method in the literature, proposed by [102], originates from transformer analysis. Another approach suggested by [71] leverages exact analytical equations for round conductor windings to compute AC resistance, resulting in more precise results. Nonetheless, these methods rely on 1-D flux density models, not considering the effect of leakage flux crossing the slot opening.

In contrast, [72] introduces a 2-D analytical model to forecast proximity losses in the stator slots of PMSMs, accounting for the effects of the slot openings. The model solves the Laplacian equation in the rectangular coordinate system of machine slots, applying appropriate boundary conditions for the magnetic field intensity. However, it operates under certain assumptions:

- Proximity losses at the bundle level are disregarded when transposing conductors.
- The slots are rectangular in shape.
- The conductors are evenly distributed within the slot.

The model validation with FEM results for single- and double-layer windings demonstrates accurate predictions up to 1.5 kHz.

In [60], Bessel functions are used to calculate the AC resistance of a shielded multiconductor, yielding satisfactory outcomes at low frequencies but exhibiting increased discrepancies, up to 12%, compared to FEM results at high frequencies. The performance of this method is further scrutinised in [61] for machine windings, revealing a similar error level compared to the FEM results.

Moreover, the approach proposed in [59] utilises the IEEE standard Induction Machine (IM) circuit [103], with parameters sourced from manufacturer datasheets. Additional adjustments are introduced to accommodate high-frequency effects, including the inclusion of inductance for the first turns of the winding, which impacts the high-frequency antiresonance point. Furthermore, a stator turn-to-turn damping resistance is defined to address wire skin and proximity effects. However, a perfect match in differential-mode impedance is not achieved because the stator leakage inductance skin effect is not taken into account.

Upon summarising the notable cases derived from analytic methods in Table 2.3, it becomes evident that their accuracy lags behind FEM methods, with a narrower frequency range. Among these, only the method detailed in [72] provides a direct estimation of the losses due to the proximity effect in electric machines, while the damping resistance integrated in [59] addresses the skin and proximity effects in the winding along with the iron losses at high frequency in the machine.

Table 2.3: Analytic simulation comparison.

Case	Frequency Range	Iron Core	Proximity Effect	Capacitive Coupling to Ground	Validation
[62]	0–80 k	Eddy Currents		Parallel plates	Single coil
[59]	0–1 M	Damping resistance	Damping resistance	Bulk winding	DM CM (Not adjusted resonances)
[68]	0–200 k	Bertotti	FEM	Lumped C network	
[72]	0–1.5 k		Laplacian Equation		Joule Losses in PMSM (Error $< 10\%$)
[60]	0–10 M	(Shielded cable)	Bessel function		R & X with FEM (Error $\approx 12\%$)

2.2.2.3 *Parasitic Capacitances*

When the working frequency increases, the impedance of the parasitic capacitances decreases, leading to new current flow paths inside the motor which affect its DM and CM impedances. The analytical calculation of capacitances is spread out in the literature.

- **Stator-Winding-to-Rotor Capacitance:** In [34,63], each slot is modelled as a plate capacitor, comprising the air gap and opening height of the slot with air permittivity, and the insulation of the wedge slot and upper slot with relative permittivity of the insulation material. This method, while efficient, introduces an approximate error of around 15% due to geometric simplifications.

  Alternatively, [33] employs the method of image charges to compute winding-to-rotor capacitance. This technique replaces elements within the geometry with imaginary electric charges, replicating boundary conditions. Line charges represent the slot portion, while ring charges represent the end-winding portion. Despite yielding small deviations from the FEM results, this method facilitates the prediction of the bearing voltage.

Furthermore, accounting for the end-winding contribution to winding-to-rotor capacitance is essential. As described in [23], the end windings typically exhibit a rectangular structure. Hence, capacitance estimation utilises the cylindrical capacitor equation (2.18), incorporating relative permittivity (ε_r), vacuum permittivity (ε_0), end-winding length (l_{ew}) and rotor diameter (d_r) along with air gap distance (d_{air}). Validation against FEM results reveals slight discrepancies, but overall alignment.

$$C_{wr,ew} = \frac{2\pi\varepsilon_r\varepsilon_0 l_{ew}}{3} \ln\left(\frac{d_r + 2d_{air}}{d_r}\right) \tag{2.18}$$

- **Rotor-to-Stator Capacitance:** The stator and the rotor are viewed as cylindrical capacitors. To adjust for the impact of the slot openings, a coefficient is introduced, similar to the one utilised for decreasing the airgap flux density in magneto-static computations, known as Carter's coefficient. The computed results exhibit a deviation of 15% from the actual measurements, but the author argues that the estimates are conservative, given that the method overestimates the bearing currents [63].

- **Bearing Capacitance:** If a bearing rotates at a speed that allows the formation of an electrically insulating lubricating film, it functions like a capacitor, provided that the applied voltage is below the electrical breakdown threshold. Calculating this capacitance considers factors such as the minimum thickness of the lubrication film and the Hertzian contact area [63]. Experimental verification of the model is performed through voltage measurements on the bearings.

- **Turn-to-turn Capacitance:** In [64], an analytical model is presented to predict the capacitance between turns of a winding. The model does not account for capacitance between nonadjacent turns, assuming that the electric flux lines are directed only towards the nearest conductor. The capacitance between turns is a combination of air gap and coating capacitances. Although the accuracy of the analytical results in comparison to the FEM results is debatable because of the relative error, the results tend to converge to a similar order of magnitude. Additionally, in [67], the capacitance between turns in windings made of rectangular conductors is computed assuming that they act as parallel plate capacitors, but the analytical values do not align with the FEM results. Furthermore, [66] highlights the necessity of using different analytical methods depending on the actual winding configuration to avoid deviations of up to 400%. One method is suitable for widely spaced round wires in single-layer windings, while the other is applicable when the wire spacing is small compared to the diameter, assuming the conductors are in contact. Thus, understanding the specifics of electrical machine design is crucial before selecting a calculation approach [104].

- **Winding-to-Stator Capacitance:** In [34], the winding turns are considered a single winding region, and the capacitance between the stator winding and the stator core is regarded as a plate capacitance. This simplification has been found to be inadequate based on the observed outcomes. Conversely, Ramos et al. assumed that the ferromagnetic core surface acts as a perfect equipotential, causing the electric field lines to be perpendicular to the core's surface [64]. Consequently, the electric field lines from the turn to the core cover only half the distance compared to those between turns. The capacitance between a turn and the stator is approximated to be twice that between turns according to [64, 105]. Nevertheless, according to FEM findings, the capacitance between a turn and the stator should be 2.4–3 times higher than the capacitance between turns.

In table 2.4, various publications are contrasted in terms of how they calculate capacitance in electric machines, specifying the methodology or primary geometric simplification used and the degree of error compared to actual measurements. The table shows that precision is generally limited across the studies, although it could suffice for certain approximations, as discussed in those works. Understanding the geometry of the machine is crucial when selecting a calculation approach.

Table 2.4: Analytic Capacitance comparison.

Case	Winding Stator	Winding Rotor	Stator Rotor	Turn Turn
[63]		Plate capacitors (≈15%)	Cylindrical caps (≈15%)	
[34]	Plate capacitors (≈80%)	Plate capacitors (≈30%)	Cylindrical caps (≈20%)	
[33]		Image charges (4–10%)		
[23]		Cylindrical capacitors (≈30%)		
[64]	$2C_{tt}$(≈50%)			Conductors(≈32%)
[66]				For single layer (≈15%)
[67]				Plate capacitors(≈16%)

2.2.3 Measurement Based Tools

One common method for modelling an electric motor for high-frequency analysis involves measuring both the DM and the CM impedance and deriving the circuit parameters from these measurements. Although this method is widely used, it is not practical for the design phase as it requires a prototype. Typically, two different connection configurations are used to obtain impedance values in the frequency domain [26, 31, 36, 37, 39–41, 44–47, 49–51, 53–55, 57, 58]. The CM impedance measurement setup is illustrated in Figure 2.7a, while the DM impedance measurement setup is depicted in Figure 2.7b.

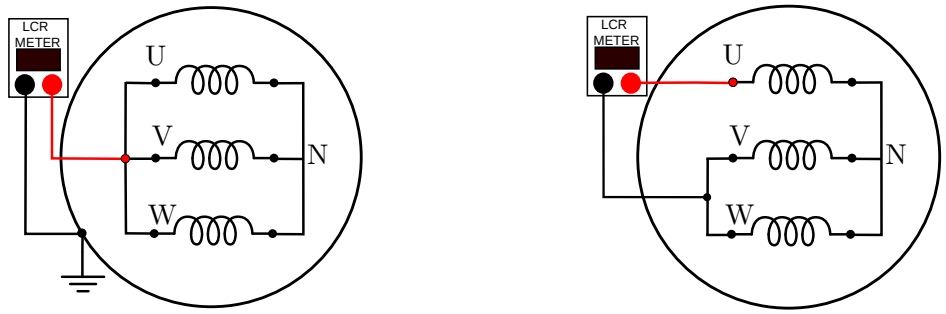

Figure 2.7: Impedance measurement connection layout. (a) CM; (b) DM.

Moreover, according to [31, 45, 46, 49], it has been mentioned that although Interior Permanent Magnet Synchronous Machines (IPMSM) have often been considered equivalent to Induction Machines (IM) for EMI simulations, the impedance characteristics differ because the DM impedance changes with the position of the rotor, influenced by the variation of reluctance, as illustrated in Figure 2.8.

In [46], a novel approach is presented, which involves measuring the impedance of two phases in series and determining the equivalent inductances for various positions of the rotor. Additionally, [36] and [41] require supplementary measurements to finalise the model parameters. Conversely, [52] examines the ground current of an induction machine and assesses the CM impedance, illustrated in Figure 2.7a, along with the impedance between the three-phase terminals and the motor neutral using a floating ground terminal.

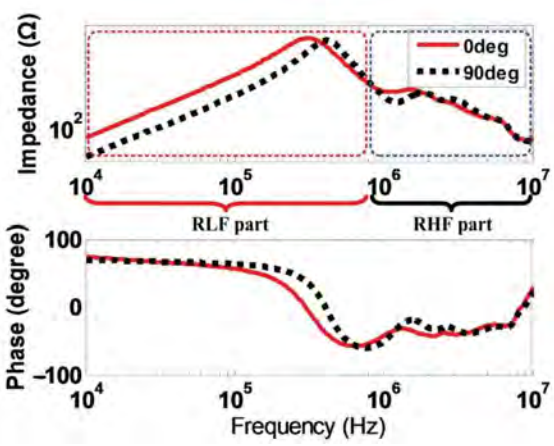

Figure 2.8: Variation in differential mode impedance due to to the effect of rotor position [31].

The method for computing the LPM parameters is dependent on the specific model used. Although most models feature predetermined LRC segments [26, 36, 37, 39, 41, 43, 44, 51–55, 57, 58], some models incorporate LRC segments equal in number to the resonance points on the impedance curve [31, 49, 50].

Many authors assign a physical interpretation to the RLC parameters, while others associate these values with specific points or regions on the impedance curve [26, 31, 41, 46]. Some researchers also employ data fitting techniques, allowing for the possibility of negative resistance values [39, 40, 106]. In a study by Hoffmann et al. [47], certain initial model parameters are analytically derived from the impedance curve, while the remaining parameters are optimised using a minimisation algorithm that enforces constraints on their positivity and realness.

After the primary classification of the methods is completed, additional pertinent information regarding the methods is discussed. In Figure 2.9, the DM impedance measurement and an equivalent circuit are illustrated. Typically, only resonances within the EMI analysis frequency range (150 kHz–30 MHz) are taken into account, and to prevent computational challenges, it is advisable for each chosen pair of peaking and dipping frequencies to be sufficiently distant from each other. For ease of characterisation, it is assumed that the inductance in every stage of the circuit in Figure 2.9a is significantly smaller than that of the subsequent stage to its right. The authors in [50] emphasise that this assumption is imposed solely on the behavioural model and does not impact the machine's performance.

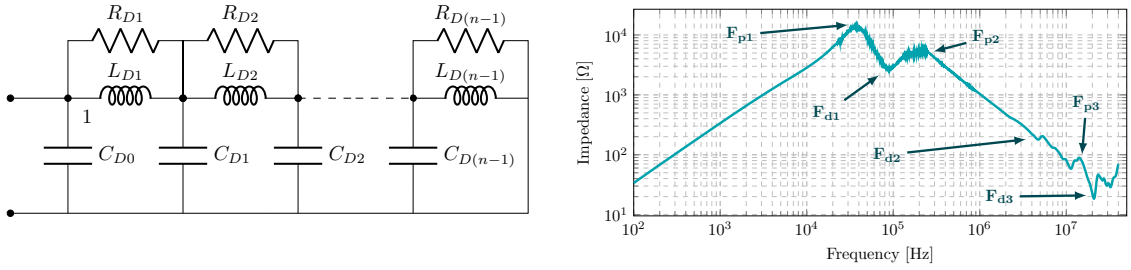

(a) (b)

Figure 2.9: Measurement-based modeling of an IM. (a) Typical single-phase equivalence for DM impedance; (b) DM impedance.

DM parameters are established based on the peaks and troughs identified in Figure 2.9b, without any specific physical significance. By applying a similar methodology to the CM

impedance, a three-phase equivalent circuit is constructed, incorporating the motor into the electric drive model and verifying it up to a frequency of 10 MHz.

Moreover, as described in [31, 46, 49], the model is segmented into two subcircuits. One pertains to the low-frequency domain, in which the RL values acquired through FEM are affected by the rotor position, while the other corresponds to the high-frequency domain, where the values are solely dependent on frequency and not on the rotor position. Validation of this model through measurements demonstrates a high level of accuracy below 3 MHz.

In the scenario discussed by [36], five tests are performed to derive the parameters taking into account the rotor, resulting in the extraction of rotor-to-stator capacitance. However, a significant limitation of this approach is that the rotor must be electrically isolated from the frame to measure the rotor-to-stator capacitance. The validity of this method and the proposed model is confirmed through validation for both EMI and shaft voltage analysis. On the other hand, [47] approaches the issue using a Lumped equivalent circuit from a different perspective. The process involves identifying a series of complex CM and DM impedances from 11 similar-type electrical machines. Initial parameters are estimated based on approximations from the measured data, and the remaining parameters are determined through a minimisation algorithm, resulting in a model that aligns with the measured results up to 30 MHz.

In [44], it is mentioned that the iron loss resistance plays a crucial role in damping the initial resonance in DM. This resistance is determined by extracting the value of R_e from the impedance at this specific resonance point. Subsequently, the model is expanded to demonstrate that more accurate outcomes are achieved when R_e is characterised as a resistance that varies with frequency, representing the skin effect observed in the ferromagnetic core.

Moreover, in [26] Rahimi et al. introduced a combined approach to determine the model parameters by integrating CM and DM measurements with FEM simulations. The model accounts for eddy current loss, inter-turn effects of the winding, and the impact of leakage inductance on the initial winding turns. At lower frequencies, the DM impedance is influenced by the stator magnetisation inductance and resistance related to core losses. Due to the presence of more unknown parameters than equations derivable from DM impedance characteristics, a 3-D FEM analysis is used to evaluate the core losses.

Lastly, in [107], a PMSM model from [55] is incorporated into the complete drive system, along with models for the inverter and power cable. Each component - inverter, power cable, and PMSM - is validated separately before the overall model is validated. The results show a high level of accuracy compared to the measured spectrum. However, additional validation is necessary in the 10 to 30 MHz range to account for electromagnetic noise generated by the voltage probes and current transducers.

2.3 MODELLING

In the preceding section, three distinct analytical tools were delineated for the analysis of high-frequency electrical machines. Through this analysis, certain electrical properties (inductance, resistance, capacitance) are derived, which are then incorporated into various models. This section categorises the principal models according to their structure, techniques for extracting parameters, and key features.

In terms of their complexity or magnitude, the models can be grouped into two classifications: Distributed Parameter Models (DPM) and Lumped Parameter Models (LPM). DPMs are known for their higher level of accuracy, although they may not be easily interfaced with other system components due to their requirement for intensive computational resources [21, 23, 61, 73, 75, 77, 78, 95].

In contrast, LPM are more convenient since they can be incorporated into a comprehensive electrical drive model, and their parameters can be derived from basic impedance measurements [24, 26, 32, 35, 37, 41, 44–47, 49, 50, 53, 54, 57, 59, 108]. Some researchers have created highly precise DPM models and simplified them into LPM using matrix reduction techniques [21] or by grouping the RL parameters [23]. An overview of the various models is presented in Table 2.5.

Table 2.5: Comparison of high-frequency models for electrical machines.

Model	Frequency Range	Model Type	Parameter Extraction	Inter-Turn Effects	Bearing Model	Rotor Model	Integration in Drive	Simulation Domain	Iron Loss
[54]	1 k–13 M		Measured	x	x		x	Freq & Time	Implicit
[41]	10 k–10 M		Measured	x	x		x	Freq & Time	Implicit
[44]	10 k–10 M		Measured				x	Freq & Time	R Parallel
[47]	10 k–10 M		Measured	x				Frequency	Implicit
[53]	100 k–500 M		Measured					Frequency	Implicit
[36]	10 k–10 M		Measured	x		x	x	Freq & Time	Implicit
[37]	100–100 M		Measured	x				Freq & Time	R
[45]	150 k–10 M	LPM	Measured	x		x [1]	x	Freq & Time	R
[55]	100–30 M	Fixed	Measured	x		x	x	Freq & Time	R
[26]	100–10 M	Segments	Measured [2]	x				Frequency	R—L—RC
[39]	100 k–100 M		Measured					Freq & Time	Implicit
[57]	10 k–1 M		Measured	x				Freq & Time	Implicit
[58]	100–10 M		Measured	x				Freq & Time	R Parallel
[108]	100–10 M	3 segments	Measured	x	x	x	x	Freq & Time	Implicit
[59]	10–10 M		Analytic	x	x	x	x	Freq & Time	R Parallel
[32]	30–5M		FEM [3]		x	x		Time	RL
[35]	100–100 M		FEM	x	x	x	x	Freq & Time	Implicit
[50]	1 k–10 M	f(F)	Measured				x	Freq & Time	Implicit
[46]	10 k–3 M	Segments	Measured [2]			x [1]		Freq & Time	Implicit
[78]	20–4 M		FEM [3]	x				Frequency	Implicit
[95]	10 k		FEM	x		x	x	Time	Implicit
[23]	100–1 M		FEM [3]	x		x	x	Frequency	R Parallel
[77]	0–100 k	DPM	FEM	x		x		Time	Implicit
[61]	10–10 M		FEM	x				Freq & Time	Implicit
[73]	1 k–10 M		FEM	x				Freq & Time	Implicit
[24]	10 k–20 M		FEM	x				Frequency	Implicit
[27]	10 k–1 M		FEM	x				Frequency	Implicit
[97]	1 k–30 M		FEM	x				Frequency	Implicit
[98]	20 k–4 M		FEM	x		x	x	Freq & Time	Implicit

[1] The rotor position is also considered. [2] FEM is used for some parameters. [3] Analytical equations are used for some parameters.

In terms of the simulation domain, certain models operate within the frequency domain to acquire characteristics such as CM and DM impedance in different frequencies. Conversely, for simulating overvoltages and currents, the time domain is essential. In this context, the frequency dependence of the parameters is typically addressed through lumped-parameter circuits, as adjusting the value for every frequency may not be feasible. Two primary approaches are outlined in this regard.

In [23], a total of four parallel RL branches are used to simulate skin and proximity effects on resistance and inductance values, each branch corresponding to a specific frequency range. The resistance of the initial branch, which represents the low-frequency range, is directly derived from the FEM values, while the resistances of the subsequent branches are determined using a frequency-dependent formula. The reduction in inductance with frequency is characterised by two empirical factors sourced from [109]. A similar approach is adopted in [31, 46, 49] to address variations in resistance and inductance with frequency. They utilise Foster's network and adjust the values through data fitting procedures. The accuracy of the models is confirmed through validation, which yields precise results.

While all models are grounded in LCR circuits, they relate to distinct components of the device and encompass different high-frequency phenomena.

- **Inter-turn effects:** In order to create a precise model at high frequencies, it is essential to account for the interactions between conductors. Most FEM-based models incorporate these interactions in their analysis, while measurement-based approaches implicitly take them into consideration.
- **Bearing:** Only a few models incorporate bearings due to the significance of their capacitance in simulating bearing currents. In other models, the bearings are ignored or computed using analytical methods [63] or empirical approaches [35, 74]. Bearing capacitance can be ignored in cases involving plastic bearings or when the machine is stationary, as noted by [23, 34]. In [59], the model includes the rotor, shaft, and bearings, which makes it highly valuable to examine the performance of the motor at various frequencies. Additionally, this model is well suited to investigate bearing currents and CM shaft voltage in both the time and frequency domains.
- **Rotor:** As C_{wr} and C_{sr} are a thousand times smaller than C_{ws}, the impact of the rotor on the impedance of the DM at high frequencies is negligible. However, when examining CM current paths for bearing currents, considering stator-to-rotor capacitance becomes crucial, requiring consideration of rotor modelling [23, 59]. Including the rotor leads to a 16.4% decrease in the maximum overvoltage related to the turn-to-ground voltage, making it essential for insulation design [77]. Furthermore, in [45], improvements are made to a traditional dq Interior Permanent Motor model by incorporating ground capacitance, iron loss resistance, and ground resistance. This modification ensures that the values of RL remain constant irrespective of the rotor's position, similar to the machine models employed for control purposes.
- **Iron Loss:** As detailed in Section 2.1.2, eddy currents play a crucial role at high frequencies. Various models incorporate a loss resistance connected in parallel with the winding impedance, while others do not explicitly mention any particular parameter in the electrical circuit to address the losses, which are inherently included in the circuit characteristics. In [26], the introduction of an R in parallel with L and a RC is suggested to consider the impact of eddy currents in iron within the mid-frequency spectrum.

For example, [78] introduces a distributed parameter turn-by-turn model. The RLC parameters are obtained from 2-D FEM simulations and analytical formulas, considering both the turn-to-turn capacitance and the ferromagnetic core capacitance. A notable feature of this technique is that the circuit is formulated in a matrix form, enabling rapid computation of the CM impedance, which is accurate up to 4 MHz. A similar strategy is applied in [110, 111] to simulate resonances and frequency responses in transformer windings, using inductance and capacitance matrices.

The proposal of [53] stands out for introducing a high-frequency model between 100 kHz and 500 MHz for PMSM used in electric vehicles. This model can effectively represent the emitted EMI frequency spectrum, even with delta-connected stators. However, its precision in determining impedance values at resonant frequencies is limited.

2.4 INFLUENCE OF DESIGN PARAMETERS ON EMC

After examining the electromagnetic interference characteristics of the machine through various models presented in the preceding section, it is essential to assess the impact of various factors using these models. Several elements can influence EMC performance, including the design parameters, materials used in manufacturing, and manufacturing processes and tolerances. When delving into the specifics of the design parameters and tolerances, FEM analysis is typically the primary choice.

2.4.1 Power Rating

While [44] acknowledges that construction materials and tolerances can unpredictably affect the model parameters, it asserts that the winding-to-stator capacitance increases with the power rating because thicker wires are employed in higher power machines, thereby increasing the turn-to-stator area. The document also notes that stray inductance decreases as the power rating escalates. However, the power rating is not a manipulable variable for optimising the EMC performance of the machine, as it is predetermined by the application and is a key requirement.

2.4.2 Grounding Points

In [112], it is observed that the configuration of the grounding points and their placement in the machine frame can influence the paths taken by high-frequency currents in the CM current flow. These HF currents typically travel to grounding points via the surface of metallic components, but the distribution of current flow may vary according to the impedance of the paths.

2.4.3 Winding Configuration

It has been observed that the impedance of a series connected winding machine is four times greater than that of a machine connected in parallel, due to the fact that the winding inductance changes proportionally to N^2. Moreover, the initial resonance frequency of a parallel machine connection is approximately twice the resonance frequency of a series-connected winding machine [58, 59, 96].

Moreover, the literature also examines the star and delta winding configurations. In [54], it is demonstrated that the CM impedance in both configurations is predominantly capacitive, with the resonance frequency being 6 times higher in the delta-connected machine. The impedance levels below and above the resonance points are equivalent since the CM paths within these frequency ranges are the same for both configurations. Although the shapes of the DM impedances for both winding connections are similar, the magnitude of the impedance in the star configuration surpasses that of the delta configuration across the entire frequency spectrum. The authors attribute this difference to the structure of the DM path. In the delta configuration, the DM path consists of approximately two windings in parallel, while in the star configuration, this path comprises one winding in series with two windings connected in parallel. In [58], the machine connections are also scrutinised and a model applicable to series, parallel, star, and delta connections is proposed.

In [59], the study of a 5 hp induction motor highlights that a delta connection winding exhibits twice the effective capacitance from the stator winding to the ground compared to a star connection.

In [38] circumferential (CW) and toroidal winding (TW) topologies are analysed in terms of winding configuration. CW represents the conventional concentrated winding in electrical machinery, whereas TW forms a toroid shape, which reduces the end windings. The research concludes that although TW may offer advantages in thermal management and higher power density, it results in an increase in winding-to-ground capacitance, leading to an increase in CM current by approximately 20 dB.

2.4.4 Conductor Diameter, Placement and Impregnation

Reducing the diameter of the conductor at high frequencies primarily results in a decrease in effective resistance and an increase in inductance values [96]. The impact on interturn capacitances is also notable, although this effect might be somewhat exaggerated due to the greater air space between conductors resulting from maintaining their position and reducing the diameter.

Additionally, the positioning of the conductors within the slot plays a crucial role in simulating the CM current and voltage. This is because the skin and proximity effects significantly influence the voltage distribution across the windings and the insulation stress in the conductors [61, 113]. When the winding conductors are farther away from the rotor, the capacitance between the winding and the rotor decreases, resulting in lower bearing currents [14, 74].

In [83, 113], it is observed that the optimal orientation of the conductors in relation to the leakage flux lines results in the lowest copper losses. Specifically, aligning the strands in parallel with the flux lines minimises losses (Figure 2.10a), while arranging them closely together leads to slightly higher losses (Figure 2.10b), and aligning them perpendicular to the flux lines (Figure 2.10c) results in significantly higher losses. Additionally, the voltage level plays a role in copper loss, as lower voltages lead to increased AC losses because of the larger cross-sectional area of the conductor needed to carry higher currents for the same power.

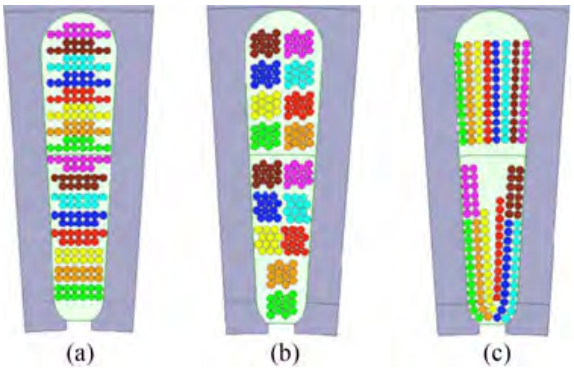

Figure 2.10: Conductor Arrangements [83]. (a) Strands aligned with flux lines. (b) Strands arranged in compact bundles. (c) Strands aligned in perpendicular to flux lines.

Furthermore, reduced capacitance has been observed to be achieved when the conductors are positioned closer to the centre of the slot rather than near the edge of the tooth [36, 76]. In addition, research indicates that a minimal amount of impregnation reduces stray capacitance, although this can affect thermal and mechanical characteristics. Therefore, a

balance must be achieved [76]. Both combinations of conductor positioning and impregnation quantity are illustrated in Figure 2.11.

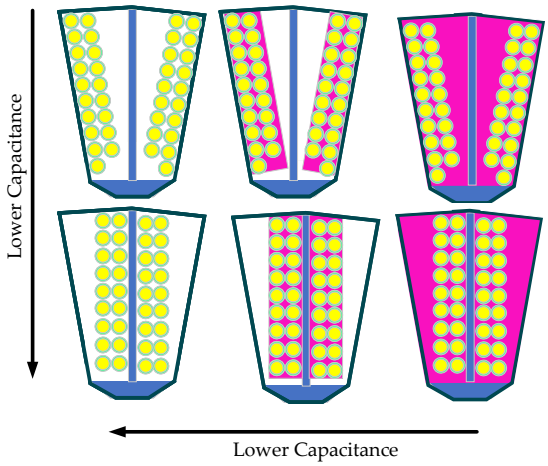

Figure 2.11: Winding position and impregnation.

In [82], they performed an analysis to examine how insulation affects the overall capacitance matrix of a slot. The capacitance coupling is directly related to the quantity of dielectric material present in the slot.

An increase in the thickness of the slot wall insulation could result in a slight increase in the CM impedance of the machine and cause the resonance point to change to a lower frequency, while the DM impedance remains almost unchanged [96].

In a more practical context, [65] presents an optimisation technique aimed at enhancing the EMC performance of DC machines by adjusting factors such as the thickness and material of the winding insulation, as well as the position of the conductors. The results were highly comparable. Although we strive for similar objectives in EMC optimisation of electrical motors, it is crucial to conduct a comprehensive assessment that takes into account all relevant influencing factors.

2.4.5 Additional Actions

Following the initial machine design, additional measures can be implemented to reduce EMI in electrical machines after manufacture. For example, as proposed in [74], the addition of extra grounded electrodes in the slot wedge can help decrease the capacitance between the winding and rotor, thereby reducing noncirculating bearing currents.

In addition, in [114] diminishing the magnitude of the magnetic flux leakage is proposed through a two-layer shielding approach for the machine, with the aim of decreasing the induced voltage in the neighbouring electrical circuit. However, implementing shielding for the entire machine could be overly costly and unwieldy, leading Vostrov (2020) to propose shielding specifically for the end windings to mitigate the winding-to-rotor capacitance and the bearing currents. The end winding, which constitutes less than 1% of the winding-to-stator capacitance, accounts for up to 40% of the total winding-to-rotor capacitance and significantly affects the phase-to-phase capacitance [35, 101]. Various shielding techniques are suggested, resulting in various reductions in C_{wr}, with notable improvements in bearing health and longevity. Although solid shielding could achieve the most substantial reduction,

it also escalates iron losses; hence, the Faraday cage shielding might present a more favourable alternative.

Furthermore, there exist external elements outside the machine that may influence the EMI performance, including the inverter modulation pattern and frequency, as well as the DC bus voltage. However, these factors are beyond the scope of this study [11–13, 36].

While the operational point of the machine or its torque angle can impact the level of DM EMI, using this as a method to improve EMI is not feasible, as it would limit the operating range of the machine [49]. Similarly, the size of the air gap also influences the stator-to-rotor capacitance, affecting both EMI characteristics and machine performance [36].

In [115], a novel systematic approach is introduced to assess the impact of tolerances on PMSM performance, with the aim of checking potential noncompliant dimensional factors and material properties. This method is based on the outcomes of the open-circuit and short-circuit tests outlined in IEEE Std 1812. The study employs Design of Experiments (DOE) to scrutinise the effects of each parameter under consideration. The output variables examined include short circuit current, torque ripple, open circuit voltage, and core losses. This methodology could prove beneficial for evaluating the influence of tolerances and design parameters on high-frequency performance.

In summary, Table 2.6 presents a summary of the various design parameters that affect the high-frequency performance of the machine.

Table 2.6: Design parameter influence review.

Parameter	**Impact**	**Optimum**
Parallel Circuits	First resonance frequency	$f_{rSeries} = \frac{1}{2} f_{rParallel}$
Y-Δ Connection	First resonance frequency in CM Impedance DM Impedance Amplitude	(Δ higher than Y) (Y higher than Δ)
Conductor placement	Cwr & insulation stress Bearing & CM Currents Shaft Voltage Copper Losses	 Furthest from rotor Middle of the slot Strands aligned with flux lines
Conductor diameter	Winding-to-ground capacitance Resistance & Inductance	Smallest -
Slot wall insulation	Winding-to-ground capacitance	The thickest **
Winding Topology	Winding-to-ground capacitance	Circumferential winding
Impregnation level of conductors	Stray Capacitance	Low (affects thermal)
Slot Shape	C_{wr}, Shaft voltage	-
Electrodes in slot wedge	Cwr & insulation stress Bearing & CM Currents Shaft Voltage	High diameter Nearest from rotor >1 electrodes together
Airgap size	C_{rs}	Minimum
Shielding	Induced voltage	Depends on frequency
End-winding shielding	C_{wr}	Faraday's cage *

* It is necessary to find a balance between the complexity of the shielding structure and the desired reduction in C_{wr}.
*Raising the insulation levels could result in decreased dissipation of heat.

2.5 SUMMARY OF THE CHAPTER

2.5.1 High-Frequency Phenomena

In the winding, the skin and proximity effects increase with frequency, affecting both the resistance and the inductance values of the coils. To model those effects correctly, a detailed geometry of the stator slot must be considered. The skin effect depends on the diameter and frequency of the wire, so it can be eliminated using conductors smaller than the skin depth in parallel strands. However, an excessive number of strands becomes ineffective at a certain stage due to the proximity effect, which also poses challenges in the manufacturing process. Litz wires are used to reduce skin and proximity effects, with an especial transposition to reduce the proximity effect, but above a frequency, the proximity effect is not softened.

With respect to capacitance couplings, the properties of dielectric insulation materials must be precisely known. Otherwise, the computation of the capacitances might differ from the real values. It is remarkable that when an electrical machine is manufactured, some conductors may vary their position from the theoretical one, making the capacitance calculation differ from the measures also.

Moreover, the end-winding should also be considered to gain accuracy, including the skin and proximity effects in that region. Concerning the capacitive coupling, even if the end winding represents less than 1% of the winding-to-stator capacitance, it is up to 40% of the total winding-to-rotor capacitance, so it must be taken into consideration especially for modelling bearing currents, where the path through the rotor gains importance.

With respect to the magnetic core, eddy currents are significant in high frequency. Not only because of the iron losses they create but also because of the shielding effect they produce. Due to this shielding effect, the magnetic flux is pushed out from the magnetic core, decreasing the effective ferromagnetic material area and leading to a decrease in the value of the winding inductance. The lamination of the stator prevents the flux from being totally pushed out of the core, leading to a higher winding inductance compared to a bulk stator. Lamination also prevents eddy currents from being generated in the stator, but once the skin depth is lower than the thickness of the sheet, more eddy currents are produced in the laminated stator, as there is a proximity effect between sheets, increasing the resistance of the coil compared to a bulk stator.

2.5.2 Analysis Tools

Regarding the FEM analysis, the detailed geometry of an electrical machine can be accurately modelled, obtaining precise resistance and inductance values, taking into account the skin and proximity effects, as well as eddy current losses in the stator and capacitive couplings. The geometry mesh is essential to obtain accurate results in FEM. When working in high frequency, the skin depth of the materials must be finely meshed, both in the conductors to consider skin and proximity effects and in the core, as the eddy currents flow along the skin depth of the iron sheets. Thus, the mesh size must be thinner than the skin depth. However, this meshing requirement leads to higher time consumption and computational load. Thus, a trade-off must be found between the complexity of the model and the resulting accuracy. For the active length of the machine, 2-D simulations are usually used, even if the resistivity of the sheets must be calibrated to take into account the lamination effects, sometimes using 3-D models. Once a 3-D FEM simulation is done,

some authors propose different coefficients to take into account this end winding, by using just 2-D FEM for successive simulations. With respect to the capacitance calculation in electrostatic FEM, the same applied to magnetic calculation is applied, needing 3-D models for the end winding, at least for the winding-to-rotor capacitance calculation, where it has a big impact. In this case, a 2 mesh layer must be defined between the conductors for turn-to-turn capacitance accuracy. The Gauss-law method is recommended for the calculation of the capacitance matrix, as it requires fewer simulations.

In the case of analytical tools, they commonly require less computation time, as some assumptions and simplifications are considered for each specific case. The skin effect can be easily calculated analytically, reducing the effective cross-section area of the conductors. Nonetheless, the computation of the proximity effect is not so simple due to the non-uniform distribution of the magnetic field in the slot. Bessel functions have been used to calculate the AC resistance of the winding, leading to 12% errors at 50 MHz. An analytical method is found to calculate the Joule losses taking into account the proximity losses, but a uniform conductor distribution is assumed in a rectangular slot, so it may not be applicable to all cases, and it is only tested until 1.5 kHz, so it may need further development for use in EMC analysis of electric machines. With respect to the capacitance values, geometric simplifications are done to simplify the calculations to plate capacitors in the case of the winding-to-rotor capacitance or cylindrical ones for the stator-to-rotor capacitance, and even if they converge to the same order of magnitude, they are not accurate enough. In the literature a novel approach for the determination of the winding-to-rotor capacitance is proposed using the method of image charges, validating the results with FEM. In the turn-to-turn capacitance, some methods can reach acceptable results, but the method must be chosen depending on the specific disposition of the winding, otherwise large errors can appear.

Concerning measurement-based simulation models, a fairly good accuracy can be reached by adjusting the model behaviour in the whole frequency range. However, it is important to note that this approach is not suitable for the motor design stage, as the prototype must already be built to perform the experimental impedance measurements and then obtain the parameter values by curve fitting. For example, this approach should be suitable for analysing the behaviour of the overall electric drive in simulation, considering the high-frequency models of the motor, the inverter, and the EMC filter, but not for predicting the behaviour of the electrical machine during the design process. Inside the measured-based simulation models, there are two different ways of obtaining the electrical circuit model, by looking for the physical meaning of each parameter and relating it to the impedance curve, or just by parameter fitting procedures, obtaining even negative values. This model can obtain excellent accuracy in the entire frequency range.

All in all, FEM tools are recommended for a detailed high-frequency analysis of electrical machines during the design stage. They take into account all high-frequency phenomena and obtain very accurate results provided that the geometry, the properties of materials, and the mesh are properly defined.

2.5.3 Modelling

The high-frequency models of electrical machines can be classified on the basis of their topology, parameter extraction methods, and their main characteristics as well as their working domain. Distributed Parameter Models tend to be more accurate, but they are difficult to integrate into the whole electric drive due to the intensive computation required.

Lumped parameter models are more commonly used as they are more practical. The LPM values are usually calculated from measurements, but there are some DPMs obtained from the FEM values that are converted to LPM with matrix reduction techniques.

With respect to the simulation domain, some models are working in the frequency domain, for example, to obtain the CM and DM impedance versus frequency. However, to simulate overvoltages and currents, the time domain is needed. In this domain, the frequency dependency of the parameters is usually considered using RL parallel branches or Foster networks, as varying the value for each frequency may not be practical. If frequency-dependent values are obtained from FEM, the equivalent RL branches can be obtained using data-fitting methods.

Finally, depending on the objective of the simulation, the developed model may highlight or neglect some parts of the machine. On the basis, all models are RLC circuits, with different number of segments and different physical meanings, but in origin, all refer to winding self and mutual inductances, resistance, and parasitic coupling capacitances. The interturn effects in the winding are essential to obtain accurate results, whereas the bearing capacitance is just included when the bearing currents are analysed. The iron losses produced by eddy currents in the stator are sometimes included as a resistor in parallel with the winding, whereas other times the losses are just implicit in the circuit values.

Concerning the rotor, its influence may only be significant when analysing bearing currents, shaft voltages, or terminal overvoltage. The rotor position is also important in the low-frequency range for salient-pole permanent magnet machines, as the inductance changes with the rotor position. Therefore, if a full frequency range (0 Hz–30 MHz) model is required, the rotor should be considered.

Finally, it should be mentioned that, generally, the models presented in the literature have not been demonstrated to be accurate in the overall range of frequencies covered by the EMC standards (from 150 kHz to 30 MHz). All proposals found in the literature show rather good accuracy up to 10 MHz, but not in the range of 10 MHz and 30 MHz. It would be convenient to extend the precision range to 30 MHz. Furthermore, as technological developments increase the working frequency of devices, it is foreseeable that standards will increase emission limits. Therefore, it is recommended to extend the measuring range also beyond 30 MHz.

2.5.4 Influence of Design Parameters

Different factors may affect the EMC behaviour of electrical machines, such as design variables, properties of materials, and tolerances associated with manufacturing processes. To go into detail about the design parameters and tolerances, normally FEM analysis is used as the main option.

Concerning the winding connection, the first resonance frequency of the CM impedance is higher for a delta connection, whereas the DM amplitude is higher for a star connection. The presence of parallel circuits doubles the first resonance frequency.

In relation to the conductor placement in the slot, their optimum position is farthest from the rotor, just in the middle of the slot. In this way, the winding-to-rotor capacitance is reduced, decreasing the insulation stress, the CM current, and the shaft voltage. The capacitances also depend on the amount of impregnation. The lower the impregnation quantity, the lower the capacitance. Moreover, the alignment of the conductors of each turn

with respect to the flux lines also affects the copper losses. In this way, if the conductors are aligned in the direction of the flux lines, usually horizontally in the slot of the machine, the copper losses will be lower.

Additionally, electrodes can be inserted into the slot wedge to reduce the bearing currents and shaft voltages, and shields can be added to the end windings or to the whole machine to reduce the winding-to-rotor capacitance, but these solutions might increase the cost and weight of the machine.

The analysis found in the literature is mainly focused on reducing bearing currents and insulation stress, so a broader approach may be needed to make an EMC strategy-based design for electrical machines.

Chapter 3

FEM MODELLING

This chapter presents a precise and efficient method to model the high-frequency impedance of electric machines. The model is validated using measurements from 28 industrial machines, taking into account manufacturing tolerances. The proposed methodology is described, detailing the required simulation steps. The complete model of individual conductors is described and compared to a simpler alternative based on bulk coils. The validation process starts with a single coil, extends to two coils, a full phase, and culminates with the complete machine. This research contributes to advancing our understanding of electric machine behaviour in high-frequency scenarios, with practical implications for design and performance optimisation. Part of the study described in this chapter was published in [2].

3.1 METHODOLOGY

This chapter presents the proposed methodology for modelling electrical machines at high frequency. This method is fully developed with Finite Element Method (FEM) simulations.

At the beginning of this PhD, another method was used that combined FEM simulations with an equivalent circuit as presented in [3]. Different coils were analysed, changing the conductor diameter and core material, which obtained good agreement with the measured impedances. However, parasitic capacitances change the current distribution of the conductors at high frequencies because of the leakage currents through them. This change in distribution will then also affect the inductance and resistance values at high frequency. Consequently, when windings with a higher number of layers and more conductors were modelled, the impedance at high frequency became less accurate.

Therefore, a new methodology has been developed in which capacitive couplings are first calculated by electrostatic simulation. Then, these capacitances are included in a magnetodynamic FEM simulation to calculate the common- and differential-mode impedances, achieving complete and accurate results. Altair Flux™ is used for FEM simulations. The process is depicted in Figure 3.1.

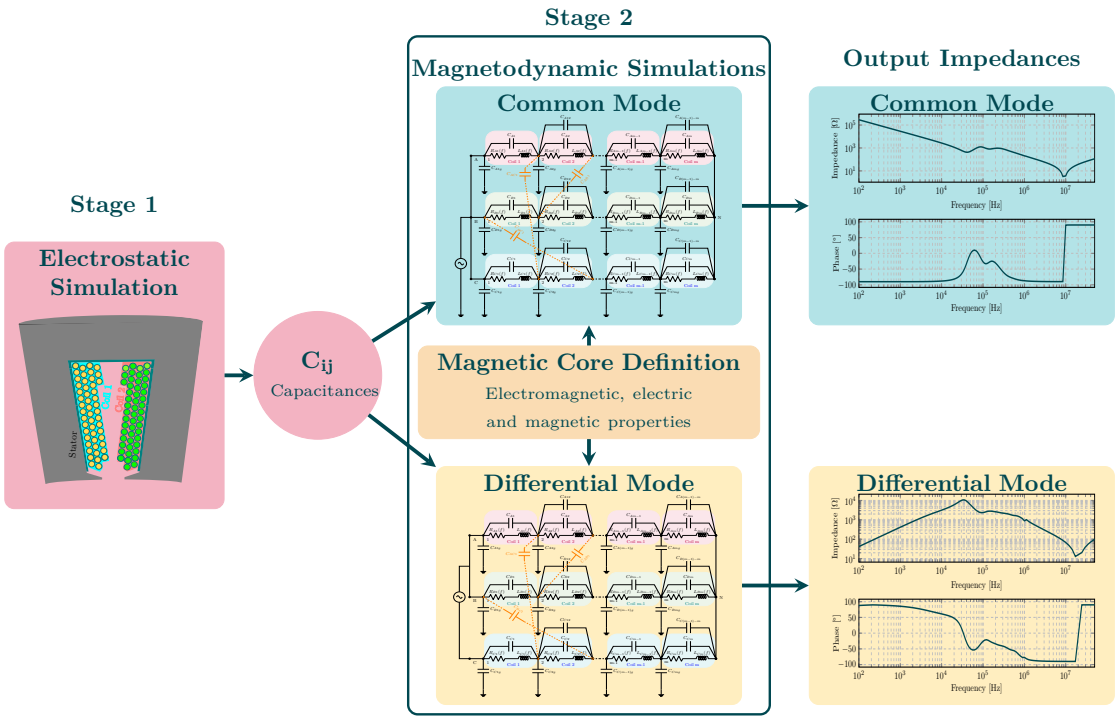

Figure 3.1: Simulation Methodology

The work presented in this chapter for the development of a high-frequency model for electrical machines is based on an industrial three-phase PMSM with concentrated winding. The main parameters of the machine are detailed in Table 3.1.

Table 3.1: Parameters of the analysed Machine.

Stator Slots	Poles	Coils per Phase	Turns per Coil	Conductor Diameter	Core Material
36	15	12	50	1.6 mm	M800-65A

3.2 ELECTROSTATIC SIMULATION

The electrostatic simulation involves the calculation of the capacitances between the conductors and between the conductors and the stator core. The process of obtaining the capacitance matrices is defined in Figure 3.2. In this section, the details of each step are described.

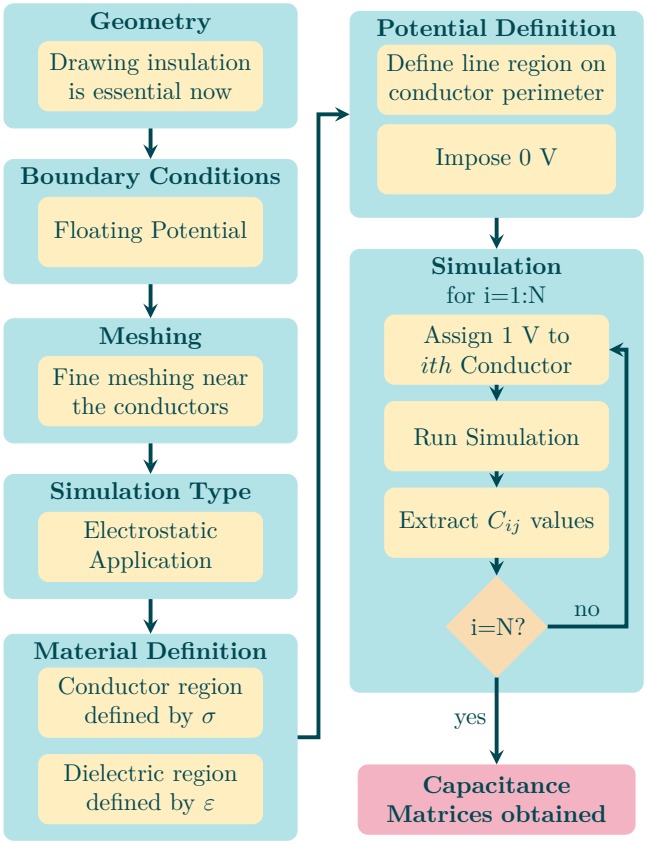

Figure 3.2: Process for electrostatic simulations.

3.2.1 Geometry & Meshing

Only a single slot in the machine is considered, and all conductors within the slot must be specified along with their insulating and impregnation materials. Ultimately, the conductors within one slot will not be capacitively connected to those in another slot because the stator core is positioned between them. In Figure 3.3, the concept of electrostatic simulations is depicted with two conductors. The key is to define the conductive and dielectric regions with their characteristics and with the corresponding distance between the elements.

The following elements must be defined based on Figure 3.3:

- **Domain:** Defining the boundaries of the simulation involves enclosing the simulated elements within an infinite box. This box serves as the boundary condition and is typically designated as either air or vacuum.
- **Perfect conductors:** Conductive components, such as conductors, the core of a coil or the stator of a machine, are considered perfect conductors because they are presumed to have equipotential surfaces.

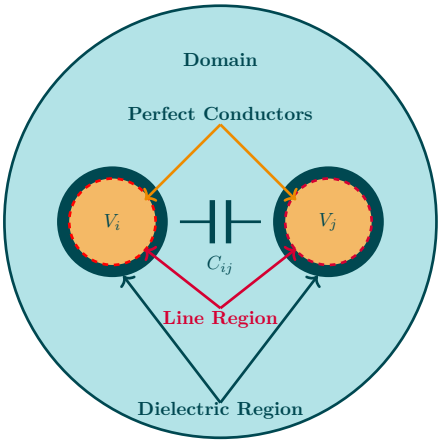

Figure 3.3: Capacitance Modelling.

- **Dielectric region:** Elements that are neither conductive nor air must be defined as dielectric so that permmitivity can be defined. They are usually insulation resin and conductor insulation.
- **Line region:** The surface of the conductive elements must be imposed with a 0 or 1 V potential to obtain the capacitance matrix. This is because the surface of the conductor is considered equipotential, i.e., the entire surface of the conductor is at the same voltage. Thus, a line must be defined in their perimeter to impose this potential.

Regarding the meshing, although it is not as critical as in the calculation of the skin effect, it is advisable to perform a fine meshing near the conductors in order to calculate the electric field accurately. In this way, the calculation of the stored charge and the corresponding capacitance will be more accurate.

3.2.2 Simulation & Boundary Conditions

As mentioned above, an electrostatic simulation is needed to obtain the capacitance of a system. These simulations are usually used to analyse high-voltage devices, spark gaps, and insulators, but the most widely used results are capacitances between conductive elements. The computation concerns the electric fields ($\vec{D}$ and $\vec{E}$) whereas the magnetic fields ($\vec{B}$ and $\vec{H}$) are not considered. Thus, the equations of the electric fields and of the magnetic fields are decoupled.

With respect to the boundary conditions, the first is to set the domain as shown in Figure 3.3. This is done by setting an infinite box with a floating potential. This last condition is important because imposing a potential may change the electric field in the domain.

3.2.3 Material Definition

The electric relative permittivity or dielectric constant (ϵ) is a physical parameter of materials that describes how much they are affected by an electric field. Permittivity is determined by the tendency of a material to polarise upon application of an electric field and thereby partially cancel out the material's internal field. In fact, the higher the permittivity, the better the insulator. In Table 3.2, some common insulators used in electric machines are shown with their values of dielectric constants.

Table 3.2: Typical materials used for electric insulation in electrical machines.

Material	Use	Typical ε value
Enamel	Conductor Impregnation	5
Nomex 410	Slot liner	2.9
Poliester Resin	Inter-turn impregnation	4.5
Polyamide/Imide	Conductor impregnation	4.7
PVC	Connection Cables	3

3.2.4 Potential Definition & Simulation Procedure

Finally, after the meshing and the definition of all regions, the simulations must be performed. To do so, the process defined in the diagram of Figure 3.2 is followed. The Gauss-Law method will be used for time & resource saving.

Thus, when defining the conductor voltages, a voltage of 0 V is imposed on all of them. Then, in each of the N simulations, a conductor will be set to 1 V, and the electric field distribution will be solved. Finally, with Equation (2.14) the desired capacitances are obtained and included in the matrix. After N simulations, a full N×N matrix is obtained with the capacitances between the conductors.

The diagonal elements refer to the self-capacitances, which are typically not practically meaningful for the given circuit. The relevant capacitances are the off-diagonal elements, indicating the capacitance between the conductors i and j and vice versa because of the symmetry of the matrices. Subsequently, the stator voltage is set to 1 V and the capacitances of the conductors to the stator are determined. As detailed in [3], a matrix of capacitances with dimensions $n \times n$ is generated from the simulation, where n represents the number of conductors per slot. Additionally, another matrix with dimensions $n \times 1$ is derived from the simulation, which contains the capacitances from the conductor to the stator. These capacitance values are essential for magnetodynamic simulation.

A full conductor-based model would require a huge computational effort, as each conductor of the machine must be defined individually. To avoid that, a simplified model is also developed that uses bulk coils instead of individual conductors. A bulk coil refers to a group of x conductors that function as a unified entity. This simple representation simplifies the simulation process by decreasing both the complexity and the computational load. The variation between the descriptions of the two models is illustrated in Figure 3.4.

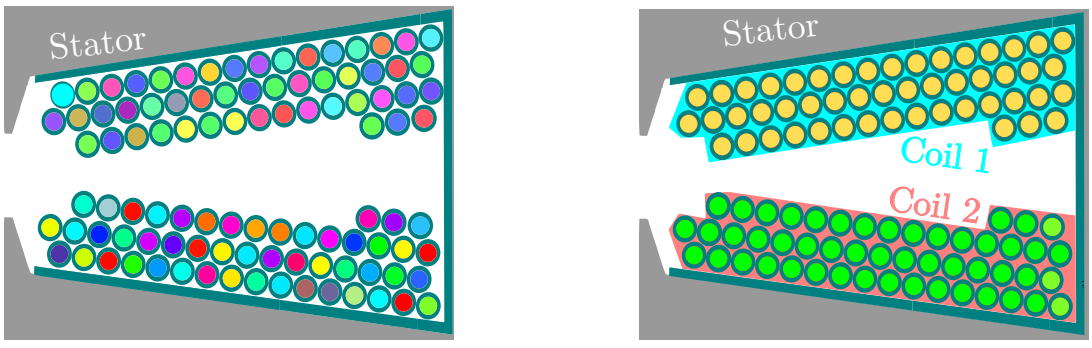

(a) (b)

Figure 3.4: Electrostatic models: (a) Full; (b) Simplified.

Taking into account the definition depicted in Figure 3.4a, where 50 conductors per coil are specified, a capacitance matrix of dimensions 100×100 is calculated, along with 100 capacitive connections to the stator for the complete model definition. As illustrated in Figure 3.4b, the simplified model retains the same geometric configuration, but the conductors on each side of the slot are combined and assigned identical voltages. Consequently, the simulation incorporates three components: two coil sides and the stator core. Although individual conductors are still represented to preserve geometric intricacies, only three nodes and the corresponding capacitances are established: the capacitance between the coil side and the stator (C_{ws}), the coil capacitance (C_w), and the coupling between the coil sides within the same slot (C_{ww}). Subsequently, after the capacitive connections have been extracted in either of the defined models, a magnetodynamic simulation is carried out to determine the CM and DM impedances.

3.3 MAGNETO-DYNAMIC SIMULATION

When current flows through a conductor material, it generates a magnetic field around it. To analyse these phenomena, a magnetic application is used in FEM. In this section, the steps for magnetodynamic simulations are described in detail, remarking the most important aspects to obtain correct results. A general diagram is shown in Figure 3.5. The details of each step are described in this section.

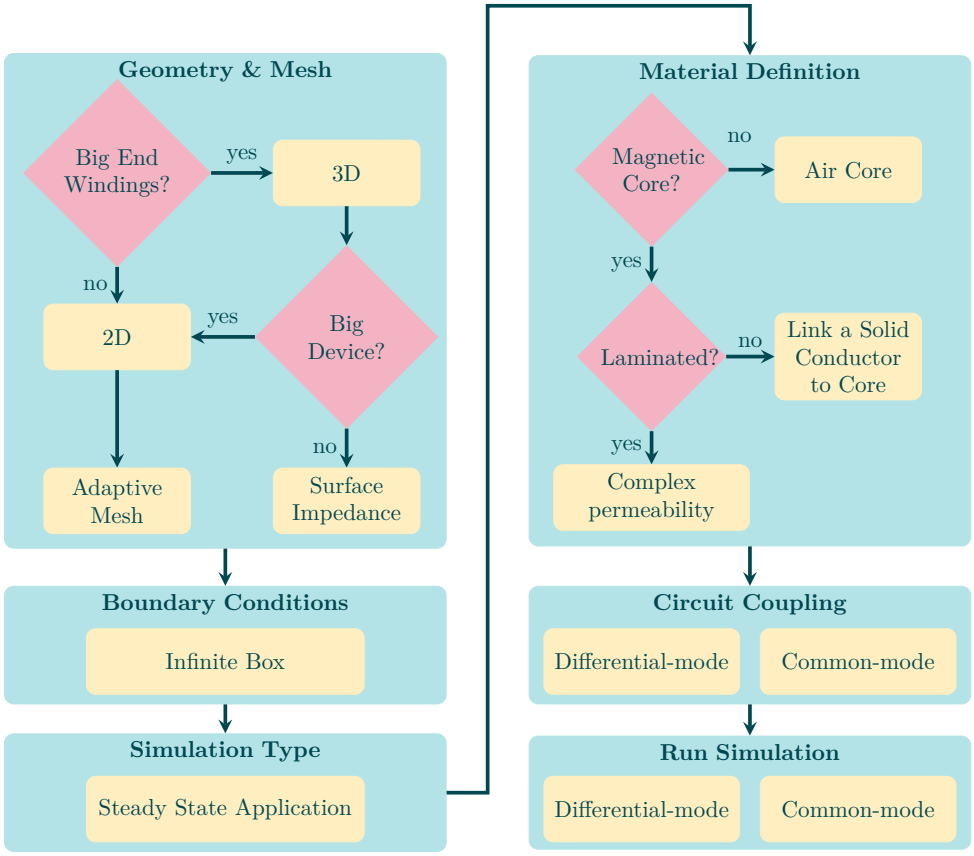

Figure 3.5: Process for magneto-dynamic simulation.

3.3.1 Geometry & Meshing

First and foremost, it is necessary to establish the geometry of the element. As discussed in Section 2.1, the characteristics of conductors become crucial at high frequencies due to the emergence of skin and proximity effects in conductive components, which impact resistance and inductance values. Consequently, it is essential to depict each winding conductor separately, although in electrical machine simulations the entire slot is typically treated as a unified conductor. The software *Altair Flux* is used for the FEM modelling of the electric machine. There are three methods to represent a solid conductor, as illustrated in Figure 3.6.

The easiest way is shown in Figure 3.6a, which consists of drawing a circle with the conductor diameter, and declare it as a solid conductor. This is appropriate for low frequencies, where the skin depth is not very significant. It is also cost-effective in terms of meshing and computational time.

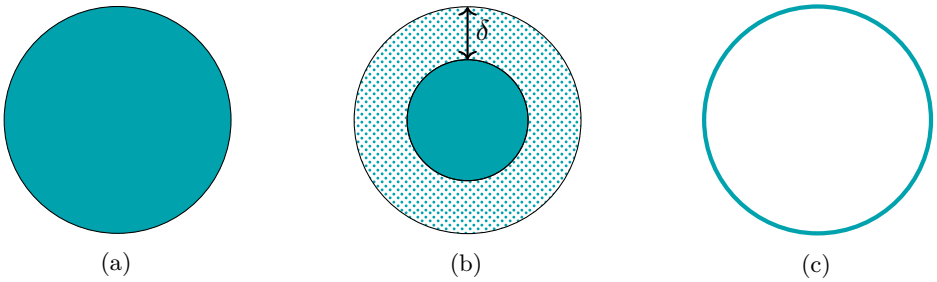

Figure 3.6: Conductor Modelling. (a) Solid conductor. (b) Solid conductor with adaptive meshing. (c) Surface Impedance.

Going a step further, in Figure 3.6b, another circle is drawn inside the previous conductor, with a variable diameter related to the skin depth (δ) of the material $D_{in} = D_{cond} - \delta$, where δ is defined in Equation (2.1). In this way, the mesh is automatically adjusted to the working frequency of the device. The main drawback of the method is that it requires drawing more lines, with the consequent increase in meshing nodes and the resolution time. If the skin depth is too low, it may also cause meshing errors.

As described in Figure 3.6c, another option is to define the conductor just by the exterior surface. This option is only available for 3-D models, as their computation time is much longer and implementing a variable mesh may be unfeasible. With this definition, since the interior of the conductor is not meshed, the solving time is reduced significantly, but it is valid only for very high frequencies. Thus, it is not valid for the full frequency range electrical machine model.

In Figure 3.7 the difference between the solid conductor and the adaptive mesh solid conductor can be seen by comparing the resistance and inductance values. It can be seen that resistance and inductance are underestimated with fixed mesh. For this example, a simple conductor of 1.6 mm diameter has been simulated, as is the one used in the analysed machine.

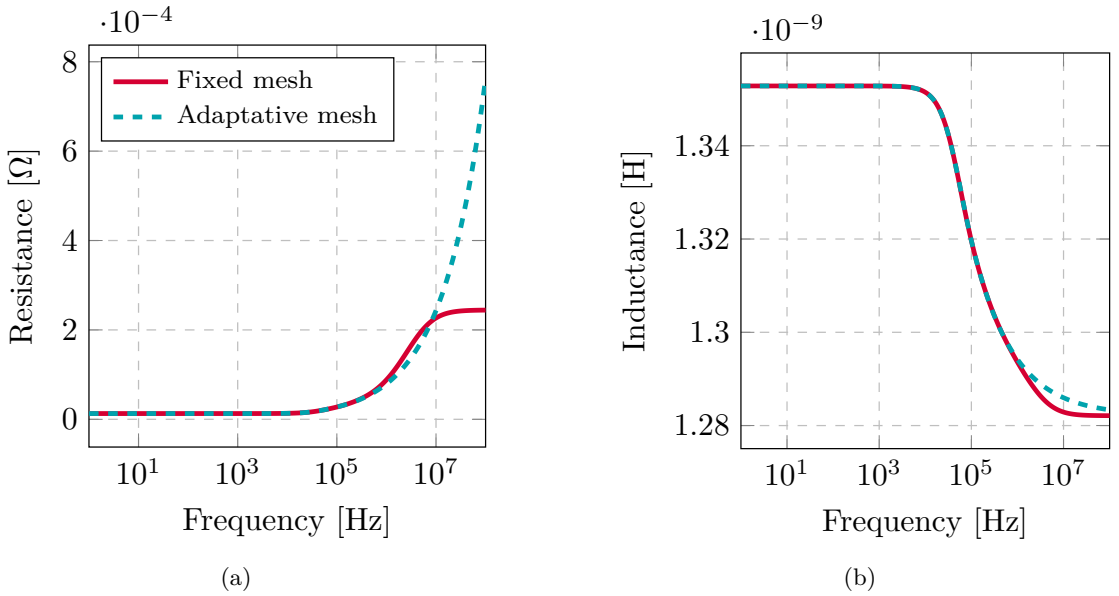

Figure 3.7: Modelling consequences in the electrical parameters of a conductor of 1.55 mm of diameter (a) Resistance; (b) Inductance.

For a 500-point simulation, the first case took 1 minute, while the adaptive case took 3 minutes. This time is considerably increased for the simulation of a coil or the entire winding of a machine, but it is necessary to model the high-frequency phenomena properly.

Once the geometry and mesh of a single conductor have been defined, it is necessary to define the geometry of the coils of the machine. Two ways of simulating the coil of a concentrated winding electric machine are shown in Figure 3.8.

(a) (b)

Figure 3.8: Magnetodynamic models: (a) Full; (b) Simplified.

In the detailed model depicted in Figure 3.8a, each individual conductor is meticulously represented and the mesh is tailored to the perimeter of these conductors, adjusting according to the frequency. However, attempting to simulate the entire machine would involve modelling approximately 100 conductors per slot in a machine housing 36 slots. Even with the application of symmetries and periodicities, this approach would impose an overwhelming computational burden due to the numerous capacitive couplings and the need for a fine mesh around individual conductors.

To address the challenges of simulation time and computational resources, a simplified method is proposed, as depicted in Figure 3.8b. In this approach, the coil is modelled as a bulk coil drawing the slot perimeter, specifying key parameters such as the turn number and the diameter of the conductor. Representing the coil without individual conductors focussing solely on the slot perimeter, similar to low-frequency models, eliminates the need for intricate conductor meshing, resulting in reduced geometric complexity and computational burden.

The simulation software can still capture the skin and proximity effects using homogenisation techniques. In fact, the positioning of the wire turns in the coil regions is given by the juxtaposition of a fixed unit cell. In these regions, the software performs a precomputation on a unit cell to estimate the impact of skin and proximity effects on the current density distribution. The results yielded by this pre-computation are then translated into equivalent material properties that are assigned to the coil region.

3.3.2 Simulation Type & Boundary Conditions

When solving a magnetic simulation, there are typically three applications available:

- **Magneto-static:** It is used to study the phenomena created by a magneto-static field. The magnetic field is related to the presence of DC currents or permanent magnets.

  The state variables are time independent and the computation concerns only the $\vec{B}$ and $\vec{H}$ fields, as they are decoupled from $\vec{D}$ and $\vec{E}$.

- **Transient Magnetic:** It is used to study variable time magnetic fields. This magnetic field can be caused by variable currents and/or permanent magnets. In this case, eddy currents and skin and proximity effects can be considered. A circuit coupling must be added to the conductive elements and a kinematic coupling must be assigned to regions in movement, such as the rotor of a rotating machine.

  The state variables are time dependent, and the computation concerns only the $\vec{B}$, $\vec{H}$ and $\vec{E}$ fields.

- **Steady State AC Magnetic:** This application allows the study of devices in the sinusoidal steady state for a given frequency. Consider that all physical quantities are sinusoidally time-varying for a given frequency. Magnets are not modelled in this case, as the magnetic field is connected with the presence of the time-varying sinusoidal electric currents. This application also considers the eddy currents and skin and proximity effects.

  The state variables are sinusoidal time dependent and the computation concerns only the fields $\vec{B}$, $\vec{H}$ and $\vec{E}$ as in the previous case.

Taking those three applications into account, it is decided that the most suitable one is the Steady State AC magnetic because it enables a frequency sweep to be conducted and allows for the acquisition of the necessary frequency-dependent parameters, in contrast to the other two alternatives.

Regarding the boundary conditions, a built-in boundary condition is set, called an infinite box. It is an air circle around the studied device, and its perimeter imposes the tangent magnetic field condition. Setting the box at a distance far enough from the device is crucial for the correct calculation of the flux lines.

3.3.3 Material Characterisation

For the magneto-dynamic simulations, there are two main characteristics of materials that must be defined, permeability and resistivity. Practically, three materials are defined: the copper conductors, the electrical sheet core, and the insulation, which can be defined as air or even as not drawn, as the electric field is not considered.

For copper conductors, the definition is simple. Its permeability is equal to 1 and its resistivity is defined as $1.72 \times 10^{-8} \Omega \times \mathrm{m}$.

Defining the material properties for ferromagnetic electrical sheets adds complexity to the modelling process. Typically, in FEM simulations of electrical machines, the core material is characterised by either a constant permeability or, for greater accuracy, the non-linear BH curve. Various methods can then be used to analyse iron core losses [116].

In machines, ferromagnetic cores are laminated to reduce eddy current losses at operational frequencies. However, at higher frequencies, where the skin depth is less than the width of the lamination, the eddy currents intensify on the core surface. This amplifies losses and induces a shielding effect that limits the penetration of magnetic flux, thereby reducing the inductance value. Although modelling this phenomenon in detail may require a 3D FEM approach with individual sheet representation [92], such an approach entails significant computational demands.

As discussed in Section 2.1.2.1, a practical method for assessing eddy currents in laminated magnetic cores, without modelling each sheet individually, involves determining the frequency-dependent effective complex relative permeability, accounting for both eddy current and hysteresis losses.

Figure 3.9 illustrates the impedance of a single coil in a electrical machine. While BH curve simulations tend to overestimate impedance near resonance because shielding effects and core eddy current losses are neglected, employing complex permeability yields impedance matching with measurements, with the resonance point suitably damped.

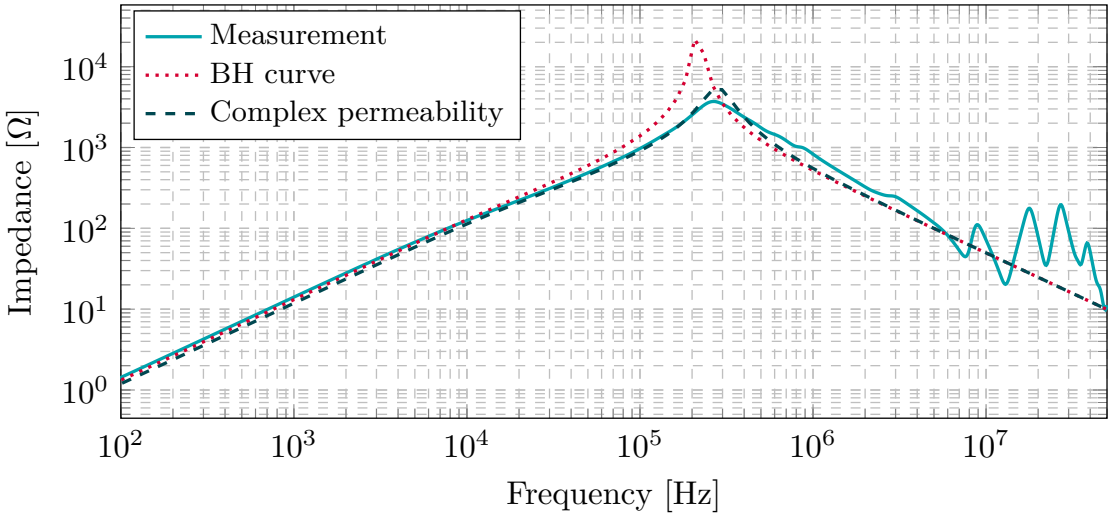

Figure 3.9: Influence of core modelling on the impedance of a coil.

In the electrical machine under study, the ferromagnetic core is made of M800-65A, which by definition has a width of 0.65mm and 8 W/kg losses at 1.5 T/ 50 Hz. It also has an approximate relative permeability of 1900 at 1.5 T/ 50 Hz. However, since a maximum of 0.5 A is introduced when measuring the impedance, very little field is produced around the sheet, decreasing the local permeability value.

Local permeability (μ_{local}) can be measured or estimated using an optimisation algorithm [30]. As samples of M800-65A sheet metal are available, the impedance of the toroid shown in Figure 3.10 was measured. This toroid is made of layers of M800-65A and is wounded.

Figure 3.10: Laminated toroidal core made of electric sheets of grade M800-65A.

The resistance and inductance of the toroidal coil are measured, enabling the derivation of the complex permeability illustrated in Figure 3.11, consistent with the proposed complex permeability model (2.7).

At low frequencies, μ'' remains at zero, indicating absence of losses in the component, but increases with frequency. Initially, μ' equals the local permeability, with a low value

around 105, suggesting that the core operates at a low magnetisation working point during measurement. As the shielding effect manifests itself, both permeability values decrease.

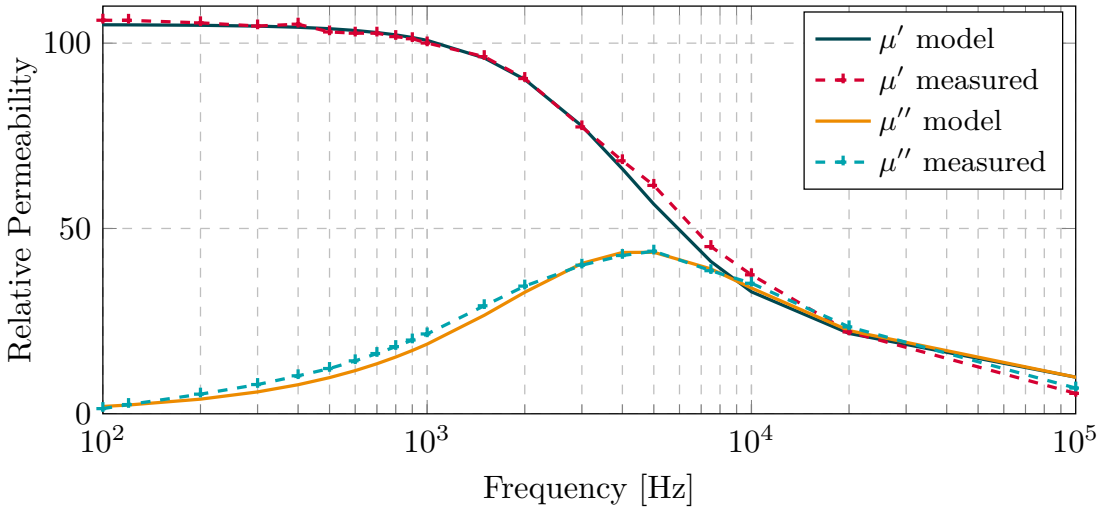

Figure 3.11: Complex permeability. Experimental vs. Simulation results.

3.3.4 Circuit Coupling & Simulation Procedure

Once the geometry is established, it is imperative to establish the connections within the circuit. The common-mode equivalent circuit per phase of an electrical machine is depicted in Figure 3.12, showing both detailed and simplified representations.

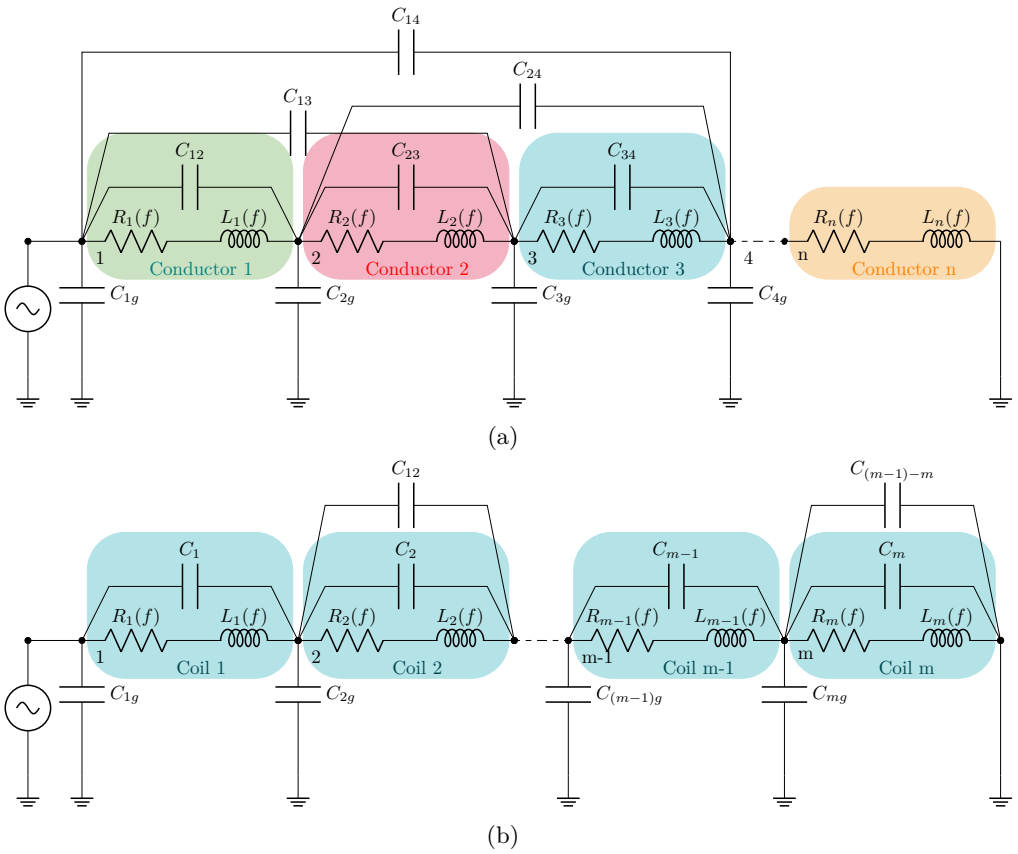

Figure 3.12: Per-phase CM equivalent circuit of an electrical machine: (a) Full (conductor-based); (b) Simplified (coil-based).

Figure 3.12a presents the full model circuit layout, where n denotes the number of conductors within one phase. Each conductor is interconnected with all others within the same slot via capacitances. Additionally, a capacitance exists between each conductor within the slot and the stator.

In contrast, the simplified representation in Figure 3.12b features m coils, significantly reducing the number of capacitive couplings. Here, capacitive connections exist only between the coils within the same slot (C_{12}), between the coil conductors (C_1), and between the coils and the stator (C_{1g}), which streamlines the circuit configuration.

3.4 COMPARATIVE ANALYSIS OF FULL AND SIMPLIFIED MODELS

This section conducts a comparative analysis between the previously discussed full and simplified models, using the impedance of a coil as a reference point. The experimental measurements obtained using an Omicron Bode100 Impedance Analyser are juxtaposed with the simulation results, as illustrated in Figure 3.13.

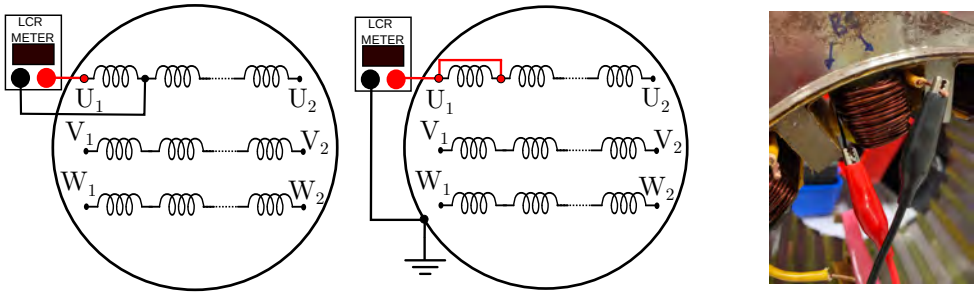

(a) (b) (c)

Figure 3.13: Experimental measurements of one coil: (a) DM; (b) CM; (c) Analysed coil.

Both models are in alignment with measurements throughout the frequency spectrum, although with varying degrees of precision, as illustrated in Figure 3.14. In particular, the simplified model demonstrates greater attenuation at the resonance point.

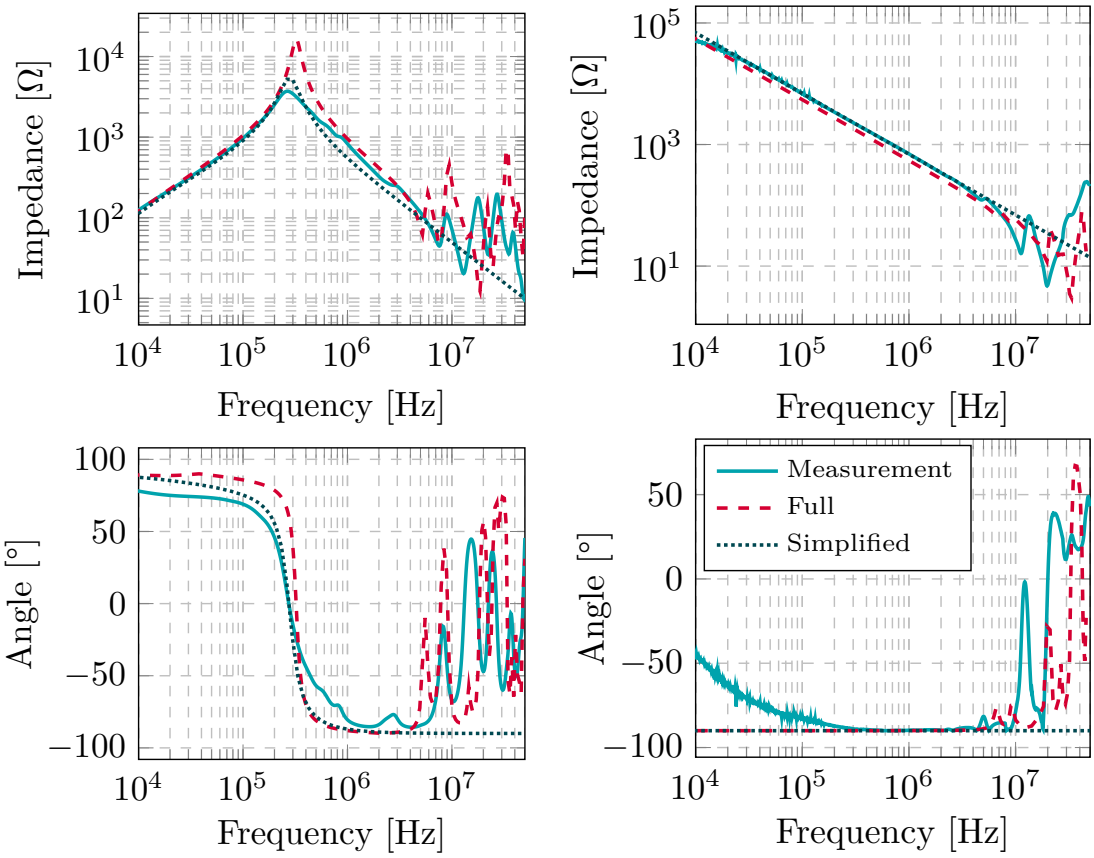

(a) (b)

Figure 3.14: One coil model. Experimental vs. Simulation results: (a) DM; (b) CM.

Furthermore, the detailed model reveals additional resonances within the 10–30 MHz range, which are absent in the simplified model. This disparity arises from the simplified

model's exclusion of capacitances between conductors, incorporating them instead as coil-to-coil capacitances. Consequently, the complex capacitive couplings responsible for these resonances are not captured in the simplified model. The primary resonance at 10 MHz in the common mode correlates with the initial turns of the coils.

The simplified model offers significant advantages in terms of its simplicity, reduced parameter count, and shorter simulation time, thus facilitating future optimisation processes, as demonstrated by Table 3.3.

Table 3.3: Comparison of Full and Simplified Coil Models.

	Electrostatic FEM Simulations	**Electrostatic Simulation Duration**	**Magnetodynamic FEM Circuit Components**	**Total Time for 100 Points**
Full Model	51	82 min	2700	11.4 h
Simplified Model	3	5 min	4	3.8 h

In calculating the capacitance matrix for a 50-turn coil using the full definition model, 51 electrostatic simulations were performed, resulting in increased nodes in the magnetodynamic circuit. In contrast, the simple definition model reduced the simulation time by 66%.

The main aim of this study is to develop a comprehensive machine model. Initially, it is acceptable to compromise accuracy and simulation speed by opting for a simplified model, as achieving a detailed definition of the entire machine may not be feasible within a reasonable time frame. Moreover, as the model expands to cover the entire machine, the impact of conductor-to-conductor capacitance in the higher frequency range will decrease, leading to better agreement between simulation and measurements, as shown in later results.

3.5 PROPOSED HIGH-FREQUENCY MACHINE MODEL

This section presents the step-by-step formulation and validation of the proposed model for two coils of the machine, then one phase, and finally the entire electrical machine.

3.5.1 Two Coils

The subsequent validation stage involved measuring the impedance of two coils, as depicted in Figure 3.15, and then contrasting it with the simulation results derived from the simplified definition model, as illustrated in Figure 3.16.

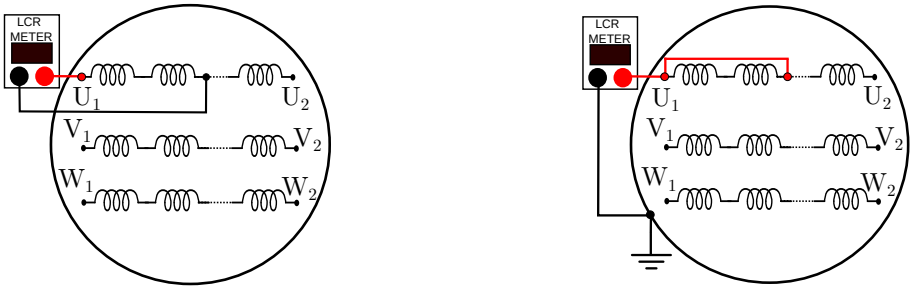

Figure 3.15: Experimental measurements of two coils: (a) DM; (b) CM.

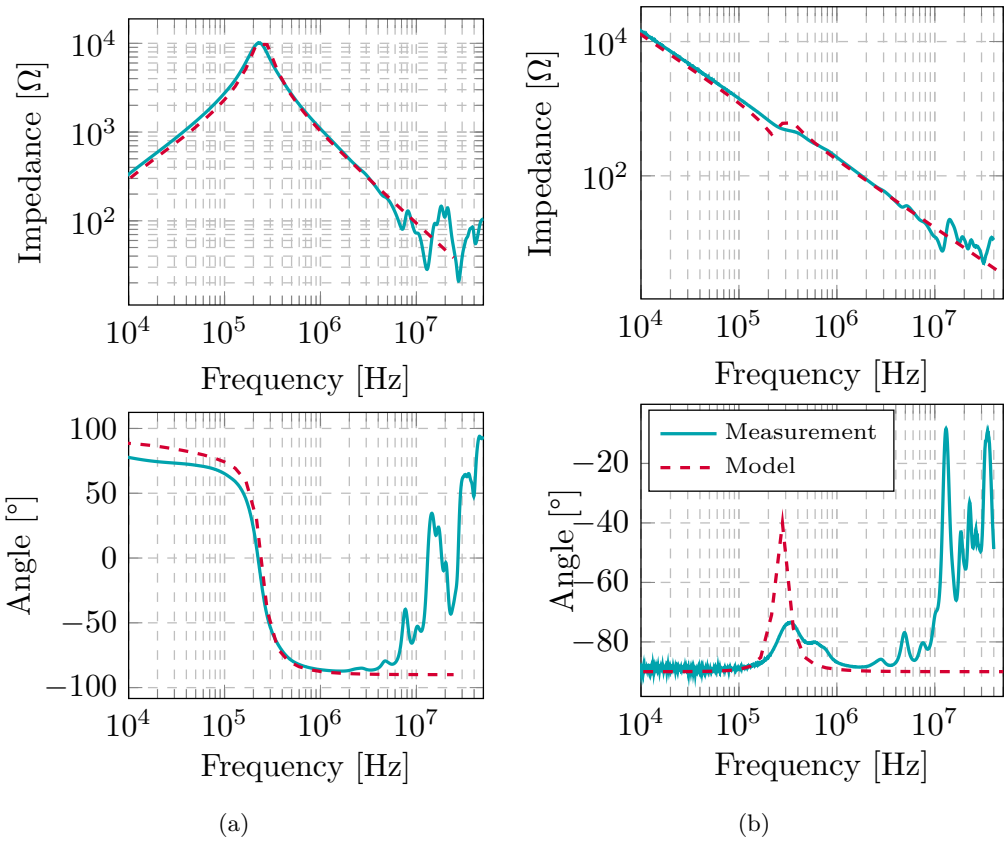

Figure 3.16: Two coils. Experimental vs. Simulation results: (a) DM; (b) CM.

The simulation findings aligned with the measurements up to 10 MHz. Beyond this frequency range, inter-conductor capacitive couplings emerged, similar to the single-coil

scenario, albeit with fewer resonances and reduced amplitudes compared to the previous case. However, the general concordance is acceptable.

A resonance is observed around 300 kHz in both the measurements and the simulation for the common-mode impedance, slightly less damped in the simulation. Once again, the initial turns of the coils and their interconnection were key factors influencing the common-mode impedance at approximately 10 MHz.

3.5.2 The Overall Phase

After confirming the validation of two consecutive coils with consistent results up to 10 MHz, the full phase was simulated and compared with the experimental data, as illustrated in Figure 3.17.

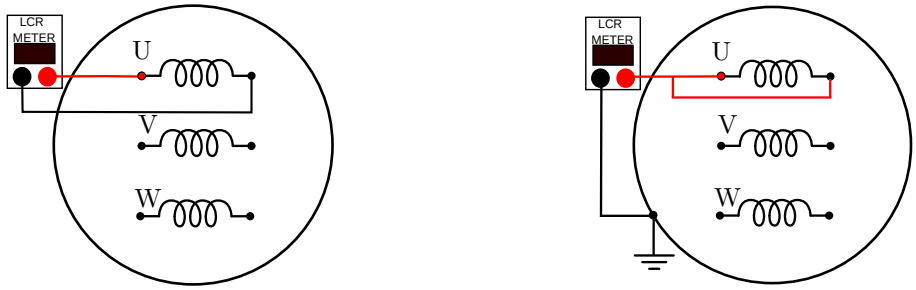

(a) (b)

Figure 3.17: Overall phase: (a) DM; (b) CM.

On the one hand, Figure 3.18 demonstrates that the simulation results closely matched the experimental data.

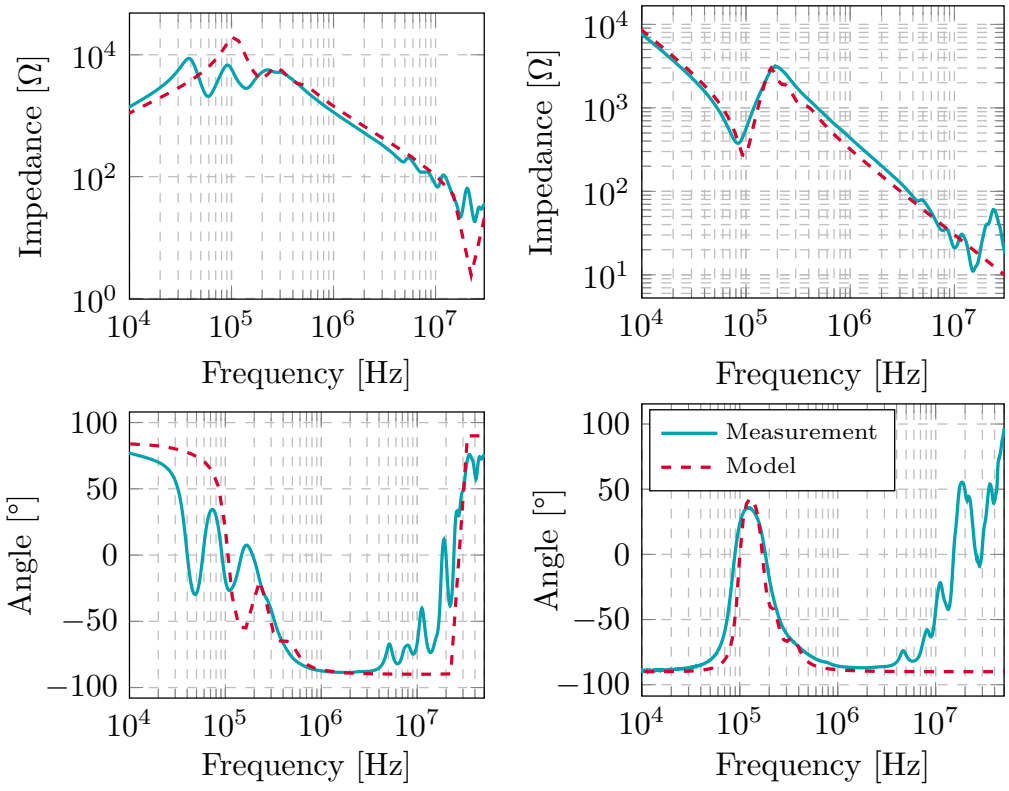

(a) (b)

Figure 3.18: Overall phase. Experimental vs. Simulation results: (a) DM; (b) CM.

However, the common-mode impedance produced a more precise result for the resonance frequency compared to the two-coil model. The presence of capacitive couplings between the coils in different slots may cause discrepancies in the resonance frequency in differential mode.

3.5.3 Full Electrical Machine

Upon validation of the simplified coil model, the full electrical machine model is simulated. Following the methodology outlined in Chapter 3.1, and integrating the three-phase electrical circuit depicted in Figure 3.19, the impedance of the electrical machine is calculated.

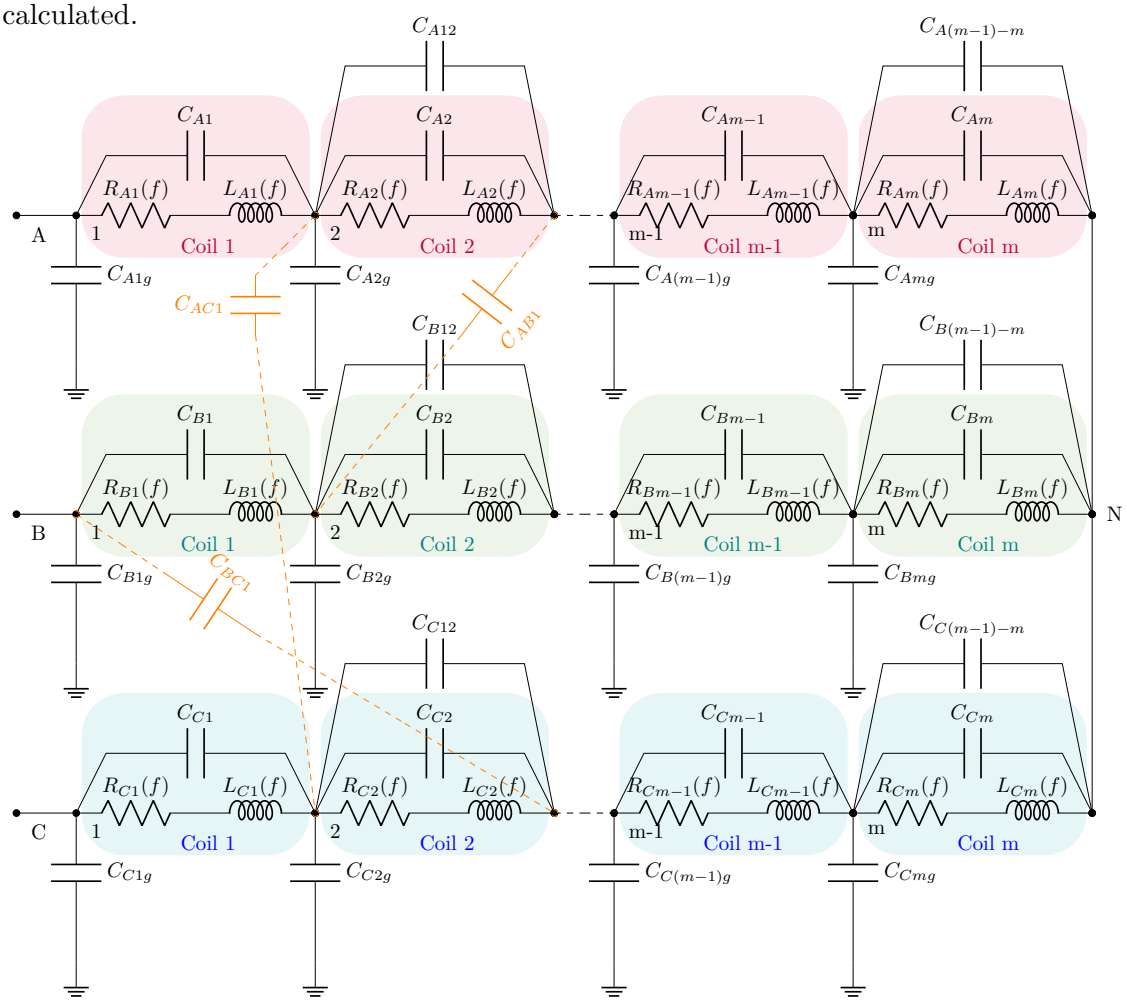

Figure 3.19: Simplified (coil-based) equivalent circuit of an electrical machine.

As discussed earlier, the calculation of the capacitances between the coils and slots is based on a single slot with two bulk coils, considering only the capacitances between consecutive coils. Consequently, the orange capacitances in the circuit, representing phase-to-phase couplings, are active only when the coils of different phases are adjacent in the same slot.

To validate the full machine model, impedance measurements of 28 electrical machines, including the rotor, were performed on a factory production line, as shown in Figure 3.20.

All machines under examination belonged to the same model, with 28 units assessed to account for manufacturing tolerances' effects on measured impedance. Impedance data, as illustrated in Figures 3.21 and 3.22, indicate a narrow tolerance range, suggesting consistent impedance characteristics in all machines, regardless of the variability of the manufacturing.

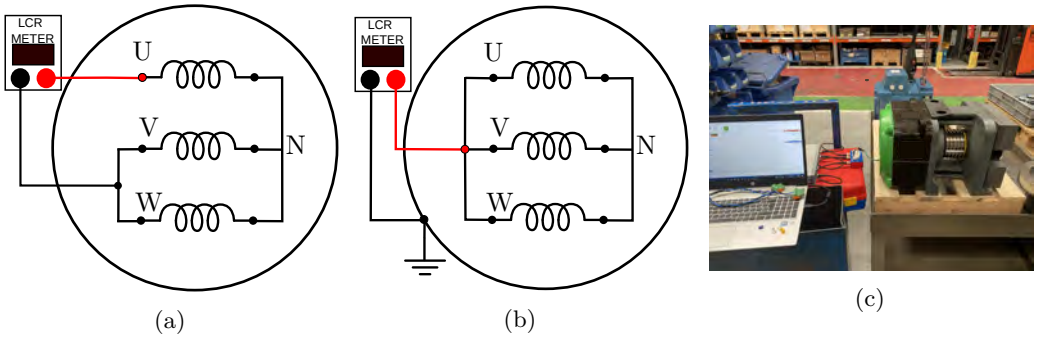

(a) (b) (c)

Figure 3.20: Experimental measurements of the machine: (a) DM; (b) CM; (c) Experimental setup.

In the common mode impedance analysis (Figure 3.21), close agreement is observed between the results and the experimental data throughout the frequency spectrum. In previous impedance measurements, an inductive effect was observed around 10 MHz that depends on not only the measured device but also the measuring connections. Thus, an approximate measurement was performed with different impedance meter calibrations, revealing that the measuring connections introduced an inductance of approximately 3.75 μH to the measured impedance. Consequently, a series inductance of this value was added to the circuit of Figure 3.19.

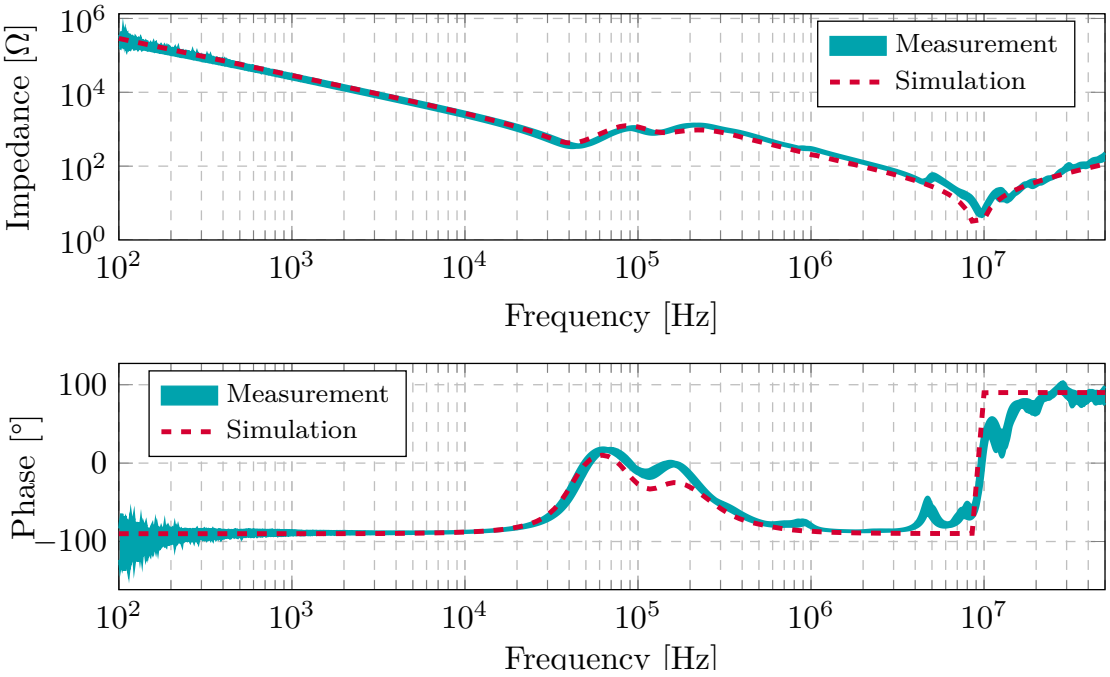

Figure 3.21: Simplified CM model of the machine with rotor. Experimental vs. simulation result.

In differential mode, two-phase connection configurations $uv - w$ and $uw - v$ were evaluated on the 28 machines, resulting in a tolerance area from the 56 measurements, as shown in Figure 3.22.

Similarly, in the differential mode impedance analysis (see Figure 3.22), the impedance values computed using FEM closely correspond to the experimental data. However, disparities in impedance values, particularly at a resonance frequency of 200 kHz, may arise from simplifications in representing the complex permeability of core behaviour at high frequencies.

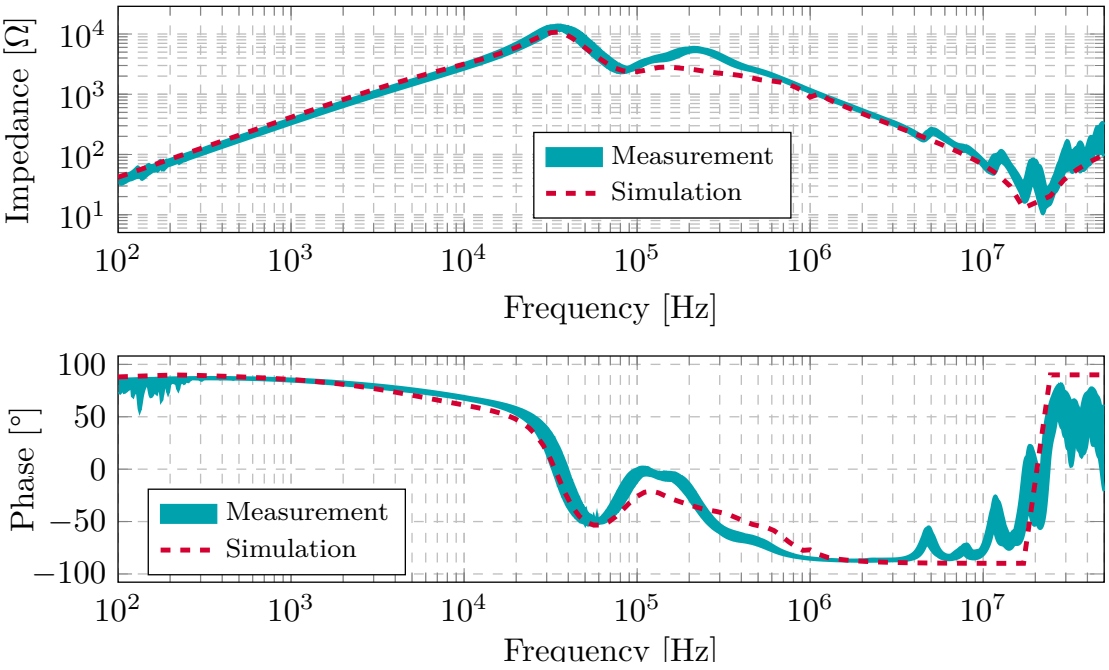

Figure 3.22: Machine DM simplified model with rotor. Experimental vs. simulation result.

Furthermore, the adopted model, designed for efficient simulation, incorporates capacitive couplings from coil to coil, but not from conductor to conductor, resulting in reduced agreement in minor resonances (10–50 MHz). However, the overall accuracy within this frequency range meets the primary objective of predicting EMI noise using high-frequency machine models.

3.5.4 Rotor Influence

Rotors are known to affect the impedance of electrical machines. Figure 3.23 shows that the presence of the rotor dampens the resonance point in the common-mode impedance and slightly displaces the resonant frequency.

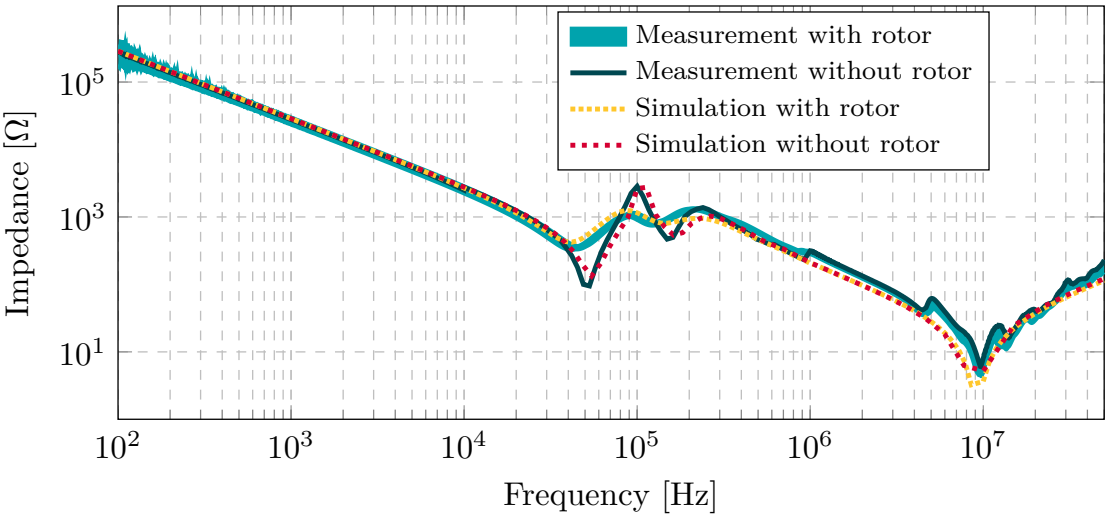

Figure 3.23: Rotor influence on CM impedance. Experimental vs. Simulation results.

The rotor also dampens the main resonance in the differential mode impedance, as shown in Figure 3.24. Additionally, the impedance until the resonant point is considerably lower without the rotor, because of the lack of magnets and the rotor core.

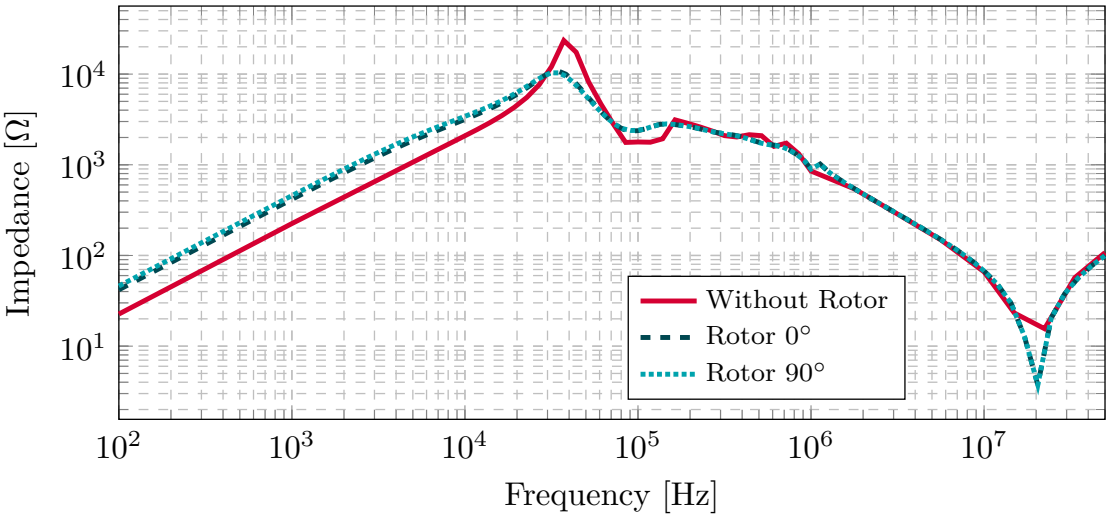

Figure 3.24: Rotor influence in DM. Simulation results.

Moreover, rotor position also influences the impedance at a low frequency due to the direct and quadrature axes, but this effect does not occur in the EMC range of 150 kHz to 30 MHz, so it was disregarded by our model.

Chapter 4

FULL DRIVE INTEGRATION

This chapter discusses the incorporation of the electric motor model into the simulation of the complete electric drive system. Initially, the modelling technique is introduced, outlining the various components and conducting an initial validation in the frequency domain before moving on to describe the time domain modelling. Subsequently, the entire drive system is validated by examining the common-mode voltage and currents. The impact of the machine on the common-mode current in the grid is then assessed. Lastly, the EMC filter is integrated into the system.

4.1 EXPERIMENTAL LAYOUT

Once the machine impedance is validated in the whole frequency range, it is time to evaluate its effect in the whole electric drive. It consists of the PMSM, the cable, the converter that generates the CMV, and the filter that prevents the CM current from going to the grid. The experimental layout is shown in Figure 4.1a, and the full drive schematic with the measurement points is shown in Figure 4.1b. The system to be measured is on a wooden pallet to avoid parasitic couplings as far as possible.

(a)

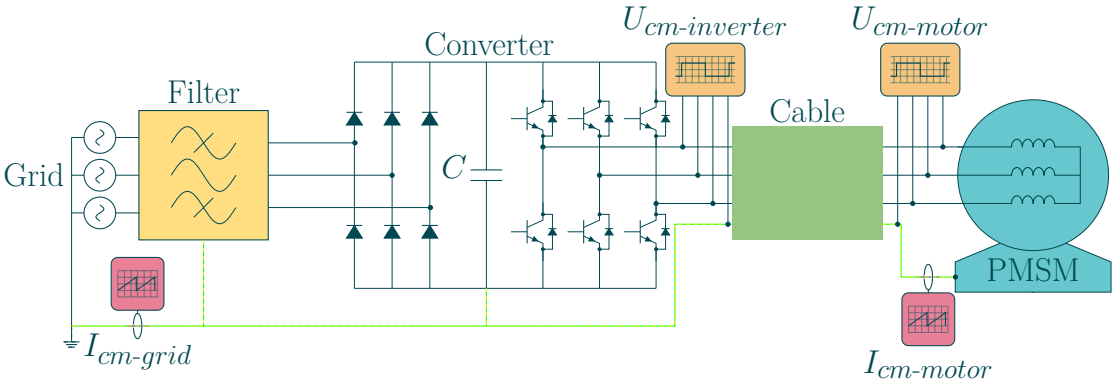

(b)

Figure 4.1: Analysed electrical drive. (a) Experimental Layout; (b) Schematic.

To validate the whole drive, some measurements are conducted to compare them with the simulations. The CM voltage is measured on the converter output and the motor input to consider the effect of the cable. The current is also measured in the motor and in the input of the grid.

The voltage probes used for the measurement are PMK BumbleBee with a bandwidth of 400 MHz. Current is measured with a TEKBOX TBCP2-750 RF current monitoring probe whose frequency measurement range is 1 kHz to 1 GHz and the transient limiter TBFL1 with a range of 9 kHz to 600 MHz. These signals are read and saved with a RIGOL oscilloscope model MSO5204 of 200 MHz 4 channels and 8GS/s.

Before comparing the simulations with the measurements, their accuracy must be carefully verified. In fact, when measuring high-frequency signals in the range of 150 kHz to 30 MHz, other devices can interfere with this measurement, and the probes themselves and the oscilloscope have a noise background.

To analyse this, the oscilloscope and the voltage and current probes are placed in the measurement position, but the drive is switched off. Then, voltage and current are measured and their spectra are obtained, as shown in Figure 4.2. This noise will be compared with all the next measurements to establish the limitations of each of them.

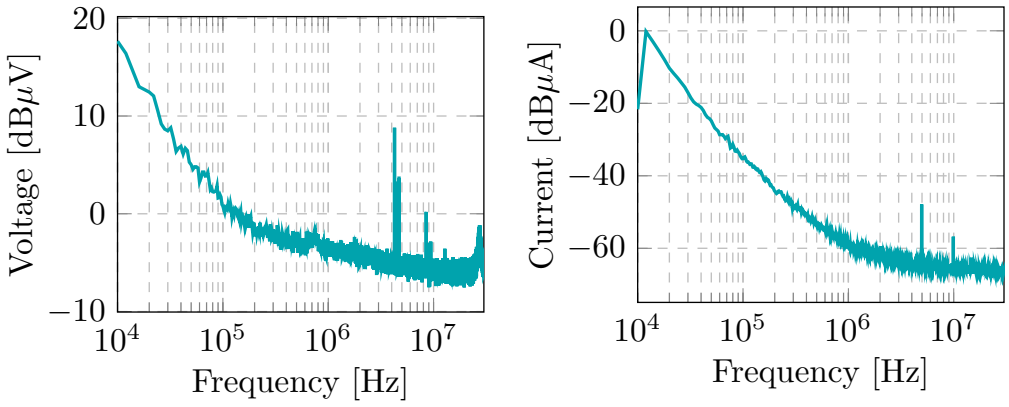

(a) (b)

Figure 4.2: Background noise in measurement: (a) Voltage probe; (b) Current probe.

As explained in Section 2.3, there are two domains for modelling electrical drives for EMI analysis, the frequency domain and the time domain. Although working in the frequency domain is more intuitive once the CM impedance of the motor is obtained with FEM simulations or measurements, it is complex to model the whole drive in this domain. Indeed, even if the connection cable can be modelled using its impedance spectrum, the PWM voltage of the converter must be generated in the time domain to observe changes in the grid current or overvoltages at motor terminals when modifying the motor impedance.

4.2 FREQUENCY DOMAIN MODEL

In order to validate the machine model in the frequency domain, Ohm's Law is used. To obtain the spectrum of the common-mode current, the spectrum of the voltage measured at the motor terminals is divided by the CM impedance of the machine. Then, this calculated current is compared with the experimental measurement. The diagram is shown in Figure 4.3.

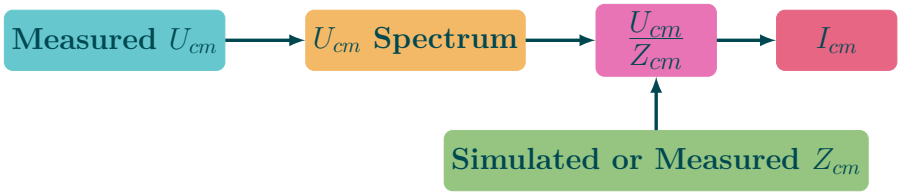

Figure 4.3: Validation process of the frequency-domain model of the electrical machines.

The common mode voltage spectrum measured in the motor is shown in Figure 4.4.

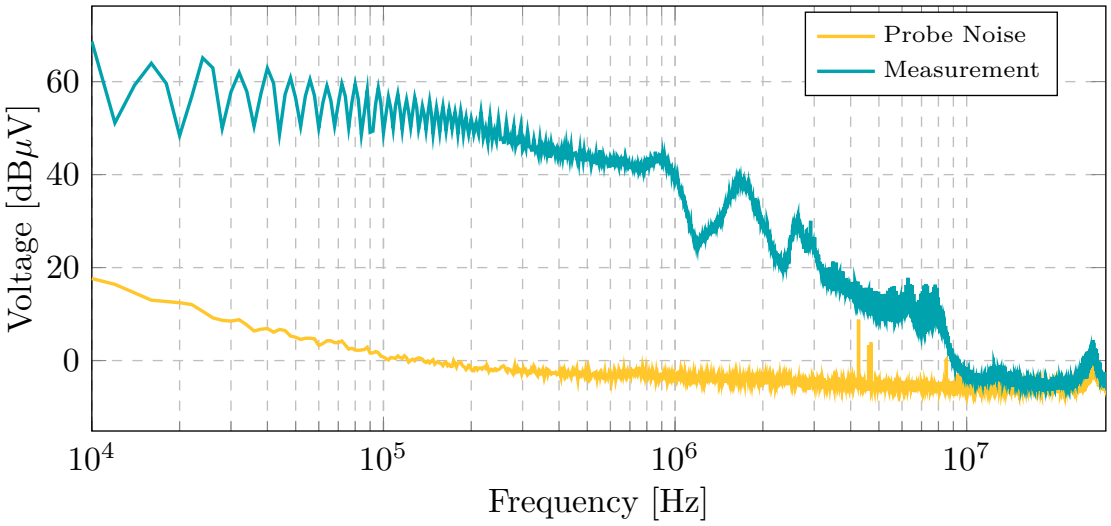

Figure 4.4: Motor Input common-mode voltage. Experimental measurement.

Given that the noise from the voltage probe becomes equivalent to the voltage value starting from 10 MHz, the validity of the voltage measurement is compromised beyond this frequency. Consequently, the resulting current will be subject to comparison only up to the 10 MHz threshold.

Then, applying Ohm's law by diving the voltage spectrum by the impedance of the machine, the current spectrum is obtained, as can be seen in Figure 4.5. When the voltage is divided by the impedance obtained with the FEM simulation, the current spectrum shown in red is obtained. The yellow and black currents are obtained by dividing the voltage by the maximum and minimum measured impedances, respectively.

On the one hand, it can be seen that the currents obtained with the FEM impedance and the ones obtained using the measured impedances agree with each other.

On the other hand, even if at some points there is a small discrepancy between the calculated and measured currents, there is overall agreement in the analysed frequency range with respect to resonance points and current value. Consequently, the current spectrum of the machine model is validated in the frequency domain.

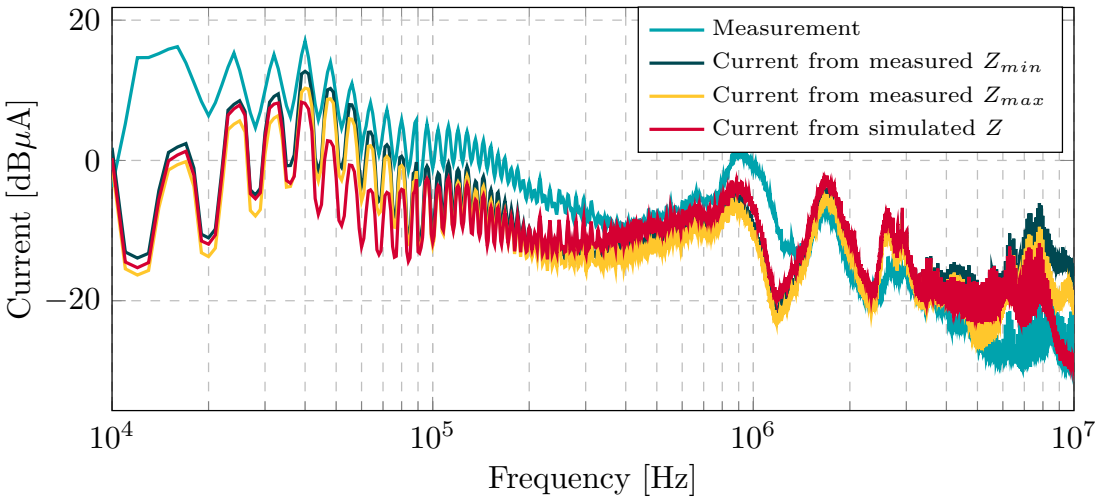

Figure 4.5: Frequency domain common-mode current. Experimental vs. Simulation results.

4.3 TIME DOMAIN MODEL

Upon validation of the electric motor model in the frequency domain, attention is now turned to the development of the time domain model for the entire electric drive. This section is dedicated to the characterization of the electric drive components, with the aim of incorporating all common-mode current paths present in the drive.

Subsequently, these components are integrated into a Matlab Simulink® model. The model is then subjected to time-domain simulation to derive the common-mode voltage frequency spectrum. As mentioned above, the drive system under consideration is depicted in Figure 4.1.

4.3.1 Converter

In the analysed drive, the grid feeds a converter. Initially, a three-phase diode rectifier feeds an uncontrolled DC bus containing a capacitor. Subsequently, a three-phase converter of IGBTs generates a PWM modulated voltage according to the voltage, frequency, and current indications requested by the drive control. These indications are those generated by the torque and speed required for the motor.

This converter is the root cause of conducted EMI, as it is the generator of the CM voltage coupled to its voltage pulses. However, the scope of this thesis is focused on the electrical machine, so a behavioural model of the converter is developed, including the common-mode current paths measured with the impedances shown in Figure 4.6 and the PWM voltage generation explained below. In addition, the bus capacitance is modelled as an RLC series branch to account for its high-frequency behaviour.

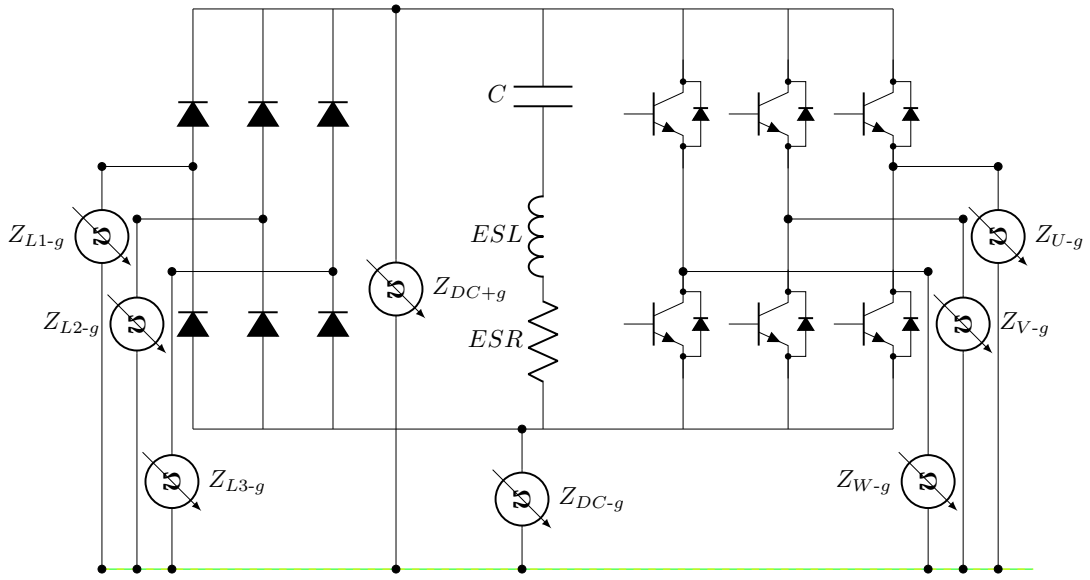

Figure 4.6: Converter CM current path characterisation.

The measured CM impedances shown in Figure 4.7, are simulated with RLC branches, and match the measured impedances in the desired frequency range. These parasitic current paths should be enough to characterise the CM currents of the entire electric drive for conducting EMI analysis.

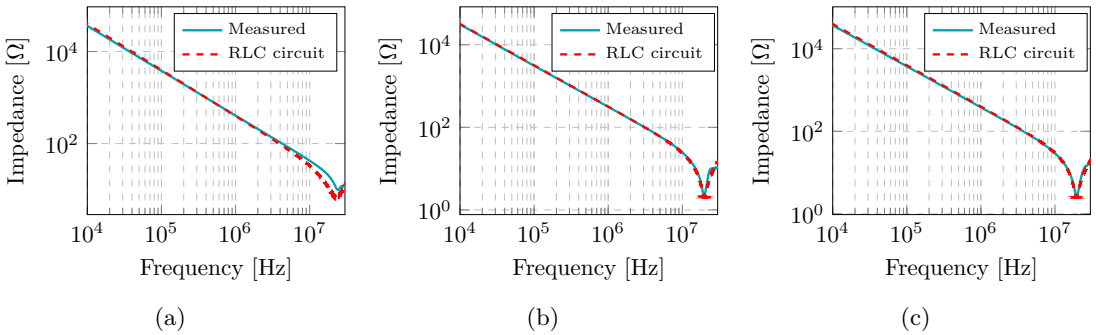

Figure 4.7: CM impedance of the converter. Experimental vs. Simulation results. (a) Z_{L1-g}; (b) Z_{DC+-g}; (c) Z_{U-g}.

The converter behavioural model produces modulated voltages through basic PWM generation by comparing a sinusoidal wave of the desired frequency with a triangular wave at a switching frequency of 8 kHz. The resulting rectangular pulse is modified to a trapezoidal one using an integrator, in order to introduce rise and fall times in the switching pulses, as it is crucial for the common-mode voltage spectrum. The diagram explaining this procedure is shown in Figure 4.8.

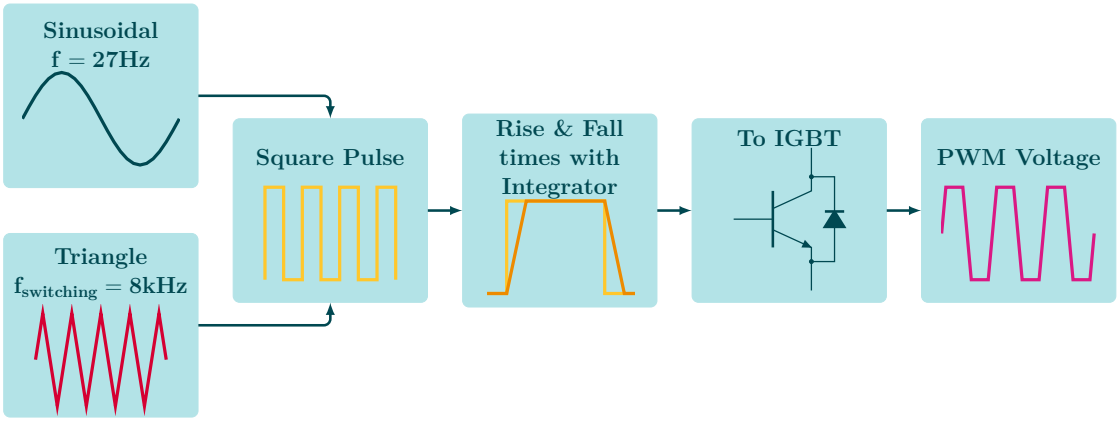

Figure 4.8: Converter modulation diagram.

It must be remarked that the parasitic components of each IGBT are not modelled for the behavioural model, only the impedances mentioned above and the switching procedure.

4.3.2 Connection Cable

The modelling of the cable is another key in the drive, as it could considerably affect the common mode voltage spectrum at the motor terminals and so on the common mode currents in the motor. The well-known PI model of an electric line is used to model the cable, as shown in Figure 4.9. In this case, 20 PI sections per phase have been used to make it more distributed, as in [107].

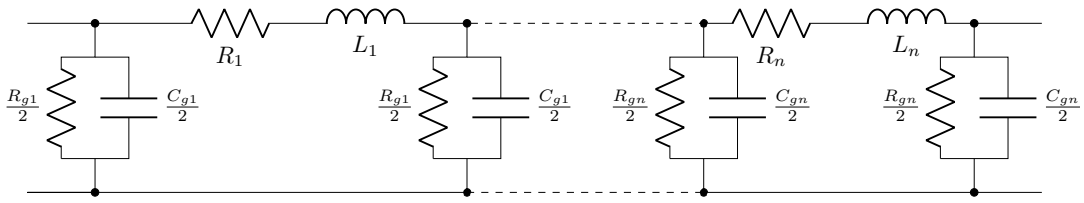

Figure 4.9: High-frequency PI model for the cable

The cable used is the same as that used in the actual drive application, so it will be characterised using its differential mode and phase-to-ground impedances (Figure 4.10), paying more attention to the latter, as the interest is focused on CM currents.

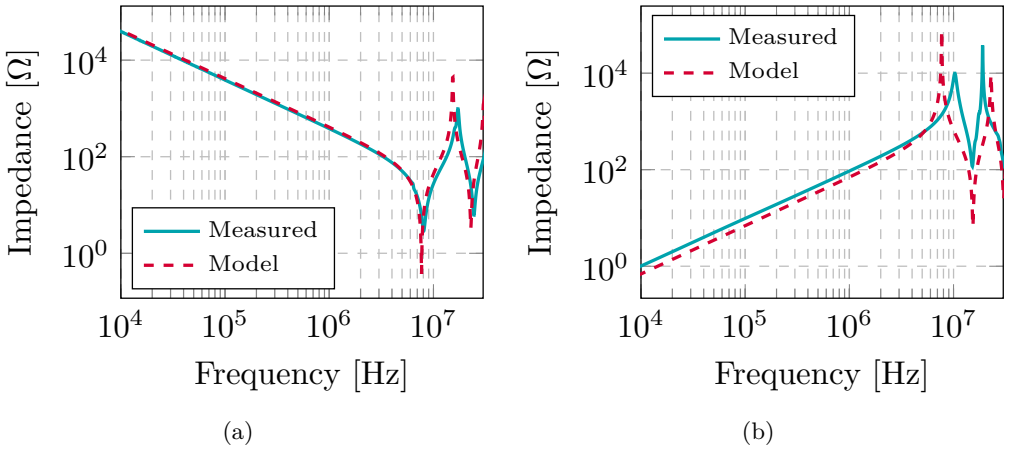

Figure 4.10: Impedance of the cable. Experimental vs. Simulation results: (a) Phase to ground; (b) Differential-mode.

4.3.3 Time-Domain Model of the Electrical Machine

In the previous chapter, a FEM simulation process was described to obtain the machine's DM and CM impedances accurately. However, these impedances are frequency dependent and must be modified to integrate them into the time-domain model of the overall electric drive. For this purpose, the lumped parameter circuit shown in Figure 4.11 is used as in [107]. The impedance obtained from the FEM model is used to define the circuit parameters so that the circuit impedance fits the impedance obtained by FEM.

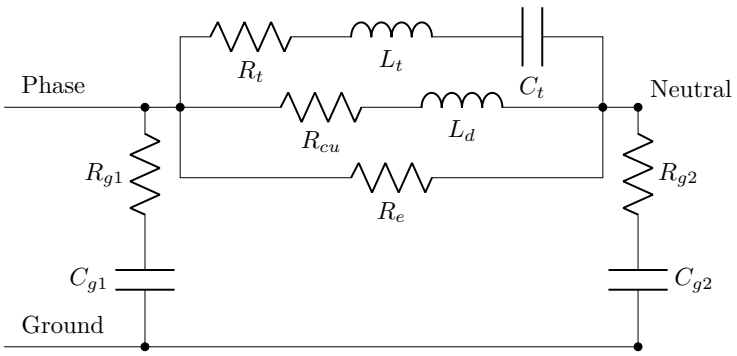

Figure 4.11: Machine Time-Domain Equivalent Circuit.

The main impedance of the phase winding consists of R_{cu} and L_d, while R_t, L_t and C_t refer to the high-frequency effects on the winding. Then R_e accounts for the core losses. Finally, R_{g1}, C_{g1}, R_{g2}, and C_{g2} represent the parasitic couplings from the winding to the ground.

These circuit parameters must be defined to match the CM and DM impedances obtained from the FEM simulation explained in chapter 3. This can be done manually or using optimisation algorithms. In this case, the parameters were adjusted using a global optimisation function consisting of a genetic algorithm. It must be remarked that priority is given to the CM impedance, as the CM currents are the main objective of this work.

When adjusting the time domain model with the FEM impedance simulation, the impedance error is defined as an objective to minimise. The per unit error for each frequency point is calculated as shown in equation 4.1, where $Z_{\text{FEM}}(f_i)$ is the FEM impedance value for the frequency i^{th} and $Z_{\text{model}}(f_i)$ is the impedance value of the model to adjust.

$$\Delta(f_i) = \left| \frac{\log(|Z_{\text{FEM}}(f_i)|) - \log(|Z_{\text{model}}(f_i)|)}{\log(|Z_{\text{FEM}}(f_i)|)} \right| \tag{4.1}$$

Then, the root mean square error for each defined frequency range is obtained in equation 4.2. The number of points for the rms value is defined as N and refers to the points of the frequency range.

$$error_{rms} = \sqrt{\frac{\sum_{\text{f=1}}^{n} \Delta(f_i)^2}{N}} \tag{4.2}$$

Six different error objectives are defined in order to catch all resonances. The error resulting from the optimisation of the genetic algorithm in each frequency range is shown in Table 4.1. The low frequency impedance is adjusted to consider the nominal conditions of the drive, which, in fact, will define the nominal current of the drive. Then, the intermediate frequency range is analysed for the resonances in CM and DM mode, and the high frequency range is used for the last part of the impedance after the resonance.

Table 4.1: Error of the time domain model of the motor respect to the FEM impedance.

Mode	$<$ 20 kHz	20 kHz – 300 kHz	$>$ 300 kHz
DM	2.77 %	3.88 %	1.09 %
CM	0.22 %	0.91 %	0.96 %

It is interesting to see how the different parameters converge during the algorithm to minimise the resulting error in the impedance, as shown in Figure 4.12. It can be appreciated that C_{g1} takes importance at the high frequency range, whereas C_{g2} it is crucial in the lower frequency range. Respect to R_e, it can be seen that it defines the damping in the resonance point in DM impedance, as is also converges to a value.

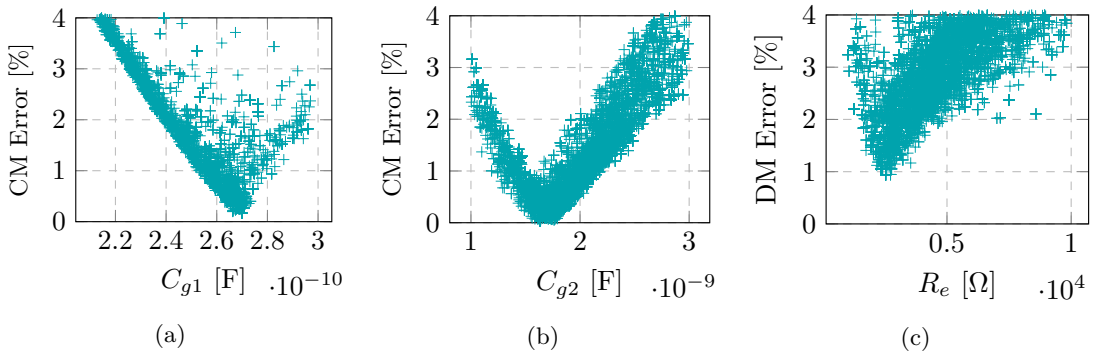

Figure 4.12: Circuit parameter convergence: (a) C_{g1} (300kHz<f<30MHz); (b) C_{g2} (f<20kHz); (c) R_e (20kHz<f<300kHz).

Using the circuit parameters obtained from the genetic algorithm, the resulting impedances are shown in Figure 4.13, showing no error in the CM impedance and a small error in the resonance point of DM impedance as expected.

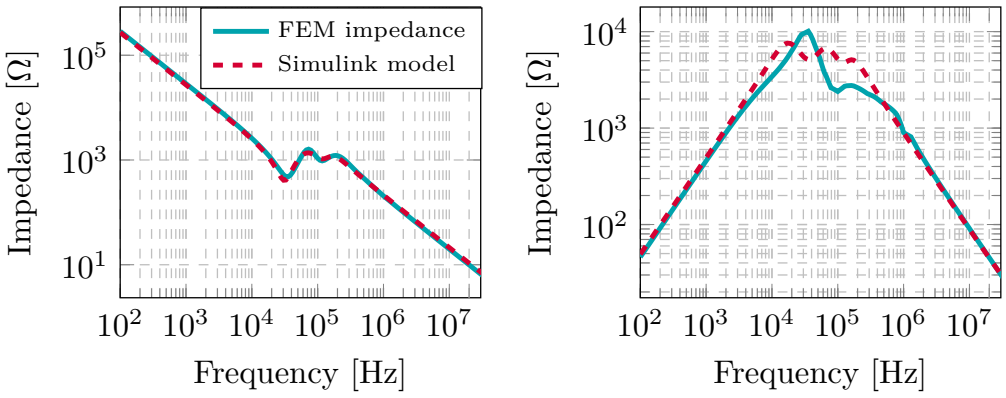

Figure 4.13: Impedance of the motor. Experimental vs. Simulation results. (a) CM; (b) DM.

Upon defining the model for each system component through their respective impedance spectra, it is imperative to validate the drive using the empirically measured voltage and current spectra.

4.3.4 Validation

4.3.4.1 *Validation of the Motor Model*

Initially, the measured CM voltage in the motor input will be introduced to the motor model to compare the measured CM current with the simulated one. In Figure 4.14, the layout of the simulation can be seen.

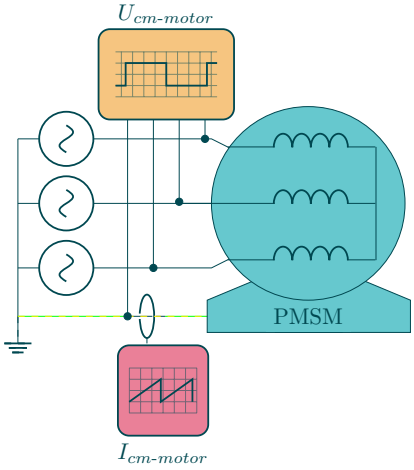

Figure 4.14: Motor time domain model validation.

As expected, the accuracy of the machines's time domain model is the same as in the frequency domain, as it can be seen in the current spectrum in Figure 4.15. Therefore, the accuracy of the time domain model of the machine is assured, for further analysis of the full drive.

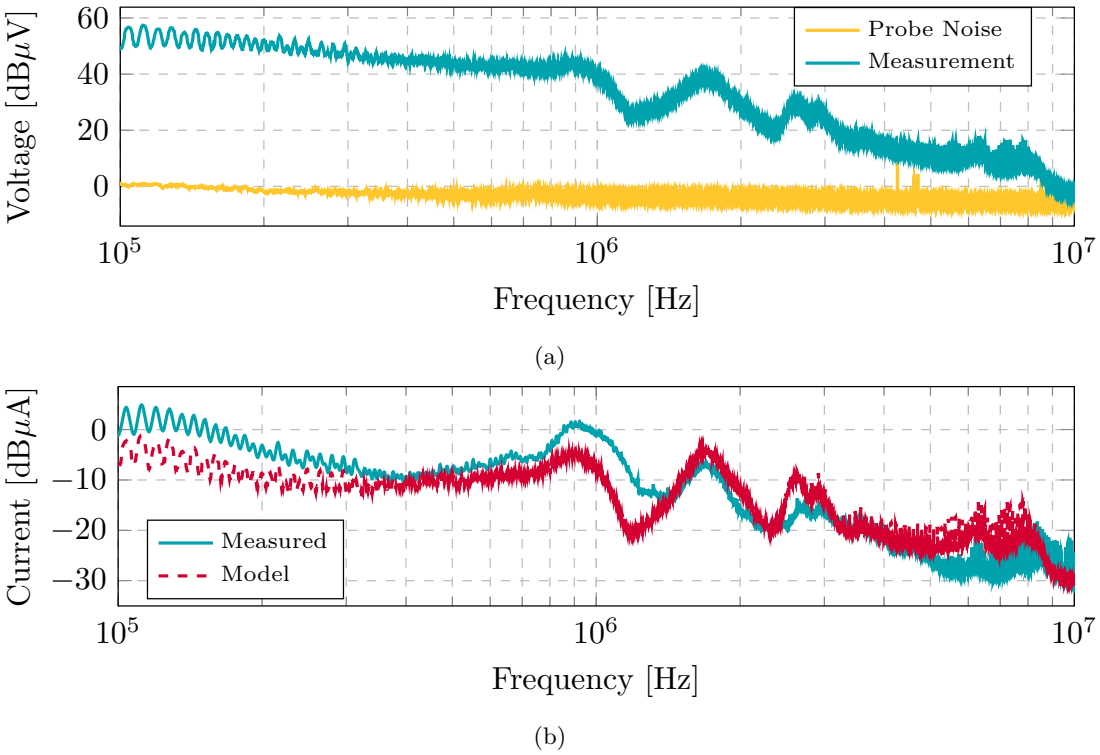

Figure 4.15: Electrical motor model. Experimental vs. Simulation results. (a) Input CM Voltage; (b) CM Current.

4.3.4.2 *Validation of the Full Drive Model*

Upon the independent examination of the machine, the whole drive system undergoes a process of validation. This involves measuring the CM voltage at both the converter output and the motor input, which serves to verify the amplification attributed to the cable. In addition, the CM current is quantified at three distinct points: the motor input, the converter output, and the grid input. These measurements are depicted in Figure 4.16.

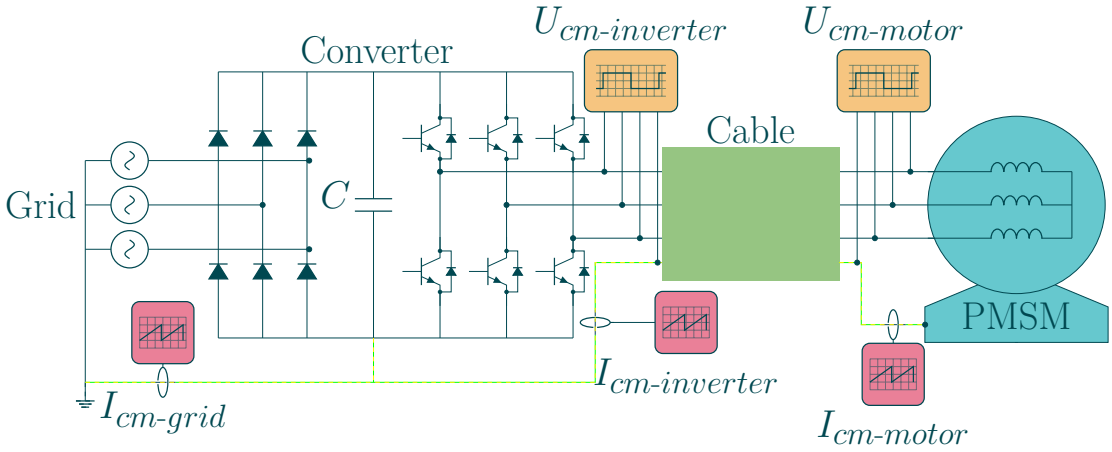

Figure 4.16: Full drive time domain model validation.

The grid supplies a three-phase 400 V system with protection or ground conductor. Then this voltage is rectified by an uncontrolled diode rectifier that generates a 560 V DC bus. Then, using modulation techniques as explained in Section 4.3.1, the machine is set to its nominal speed without load.

In Figure 4.17, the comparison between the simulated and measured common-mode voltage is illustrated. Recall that from 10 to 30 MHz, the voltages cannot be compared because of the background noise. Only currents can be compared within this range.

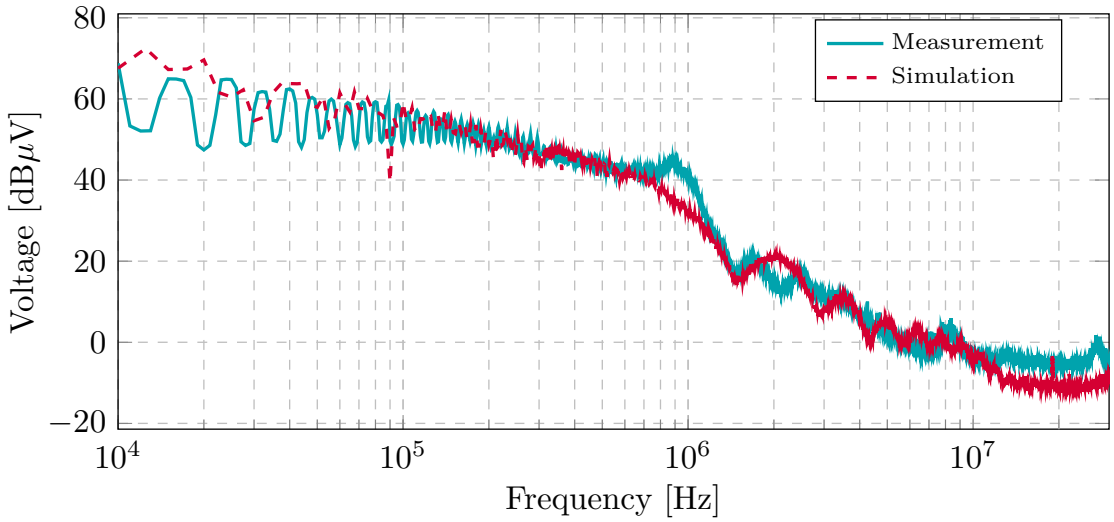

Figure 4.17: Commom mode voltage at converter output. Experimental vs. Simulation results.

It can be seen that the model agrees accurately, except for some minimal resonances in the range of 800 kHz–1 MHz and around 2 MHz. As expected, the voltage from 10 to 30 MHz is lower than the measured one, due to the probe noise mentioned in the above sections.

In Figure 4.18, the CM voltage at the motor terminals is depicted. The overall tendency agrees with the measurement, even if the resonances at 1.5 and 3 MHz are slightly displaced. It should also be noted that the voltage level is higher than in the converter output because of the cable amplification of the voltage.

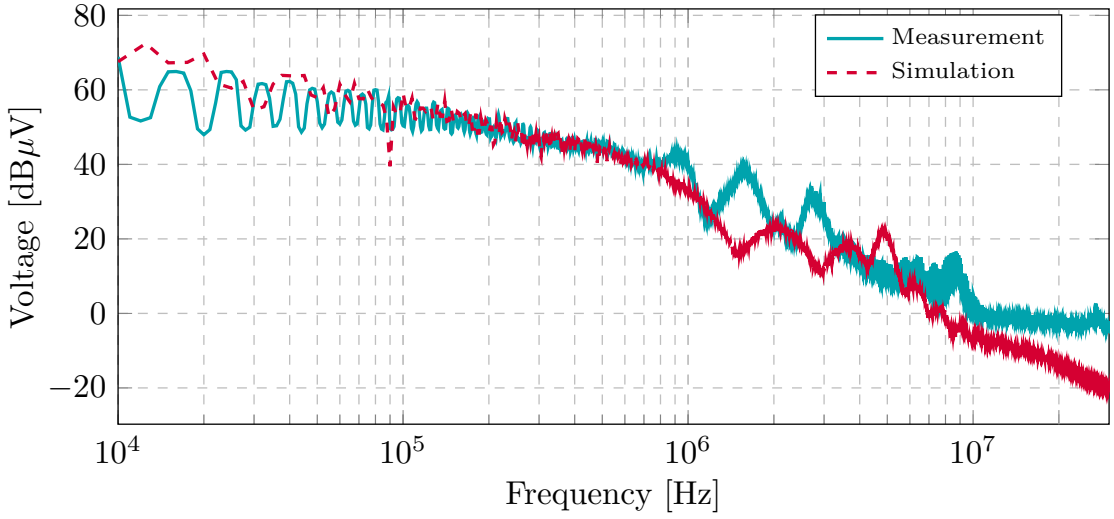

Figure 4.18: Motor input CM voltage. Experimental vs. Simulation results.

Then, in Figure 4.19 the CM current of the motor is presented. Overall, the simulation agrees with the measurement except for resonances from 1 to 5 MHz that were already displaced in the CM voltage on the motor input. Apparently, this may be due to the cable model because the motor model was previously accurately validated in Figure 4.15.

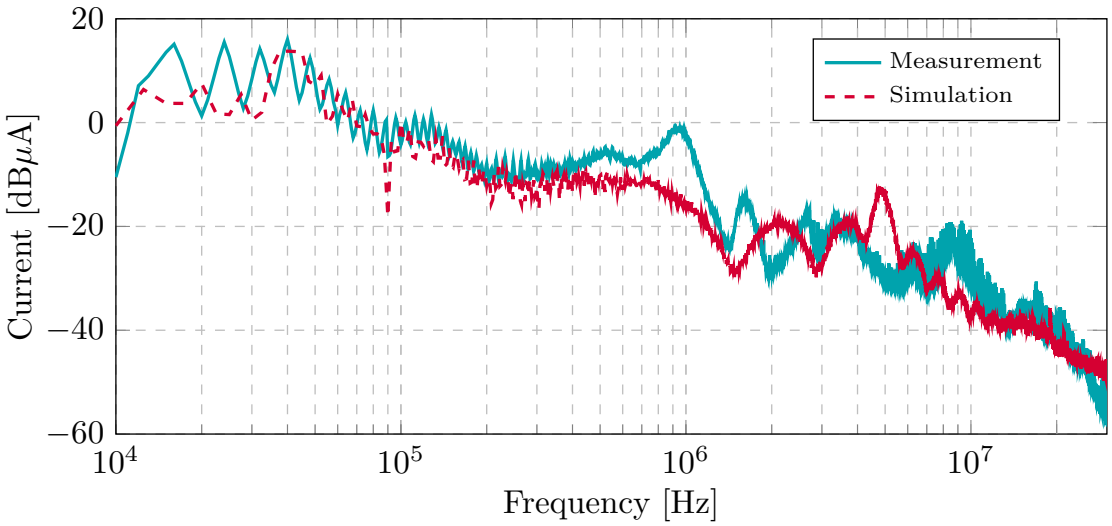

Figure 4.19: Motor input CM current. Experimental vs. Simulation results.

Finally, the current in the grid input is validated in Figure 4.20. As before, the overall spectrum agrees with the measurement, despite the small resonances previously missing in the motor input voltage, which are also missing in the final grid current. However, the resonance at 20 MHz caused by the converter parasitics is present in the model, even if a bit overestimated. It should be noted that the converter model considers the parasitic impedances shown in Figure 4.6, but the inside parasitics of each IGBT are not modelled, as it is not within the scope of the present work.

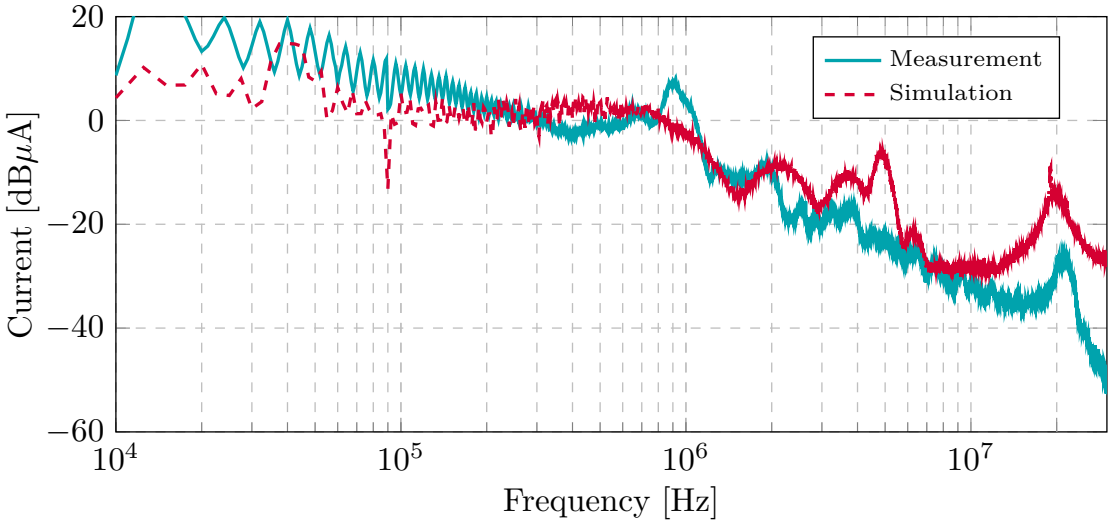

Figure 4.20: Grid input CM current. Experimental vs. Simulation results.

This section showed that the full drive model agrees with the overall measurement spectrum. In the next sections, further analysis will be made with the presented model in order to reduce the CM current conducted to the grid.

Interestingly, by measuring the CM current at the different points shown in Figure 4.16, the influence of each drive component can be appreciated. In Figure 4.21, the different currents are compared. As can be seen, the output currents of the grid and converter are higher than the one at the motor input. This is due to parasitics in the cable and converter, which also generate current paths to the ground. For example, from 100 kHz to 2 MHz it looks like the mayor parasitic current flows from the cable to ground due to

the gap between the motor and the converter output current. The peak around 20 MHz is interesting because it is not present in the motor current, but it is present in the converter output and the grid, so may be derived from the cable parasitic paths.

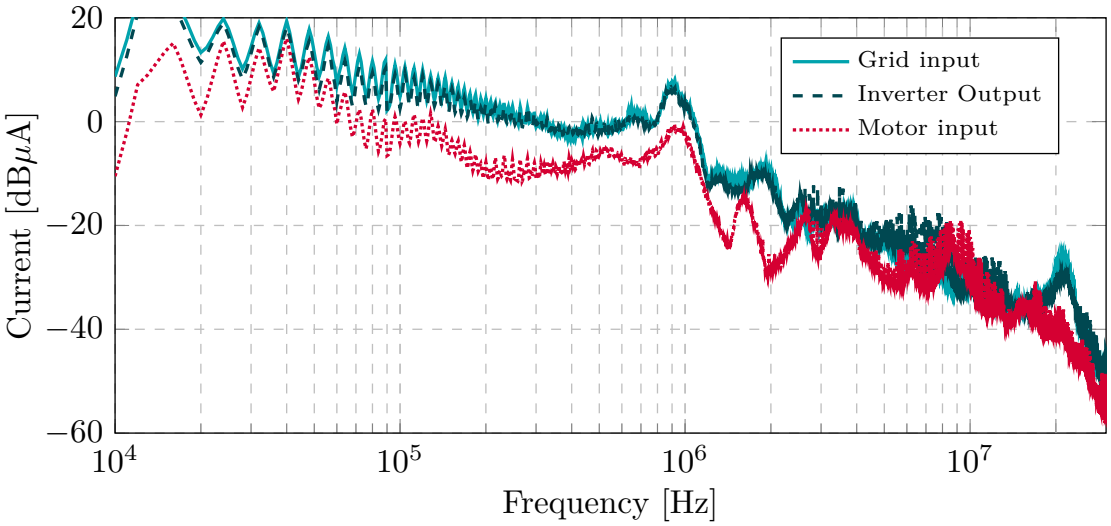

Figure 4.21: Measured CM current in different measuring points.

4.4 ANALYSIS OF THE INFLUENCE OF THE ELECTRIC MOTOR'S IMPEDANCE ON GRID CM CURRENT

Before analysing the changes that must be made in the machine to decrease the CM current, presumably increasing the CM impedance, it is convenient to check if the changes in the machine impedance affect the grid current in any way. To do so, the impedance of the machine is increased, as shown in Figure 4.22a, and the CM currents of the motor and the grid obtained from the simulation are compared in Figures 4.22b and 4.22c.

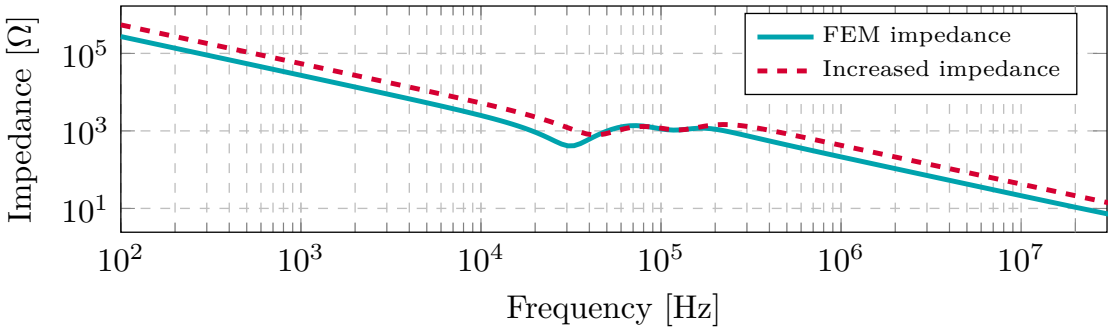

(a)

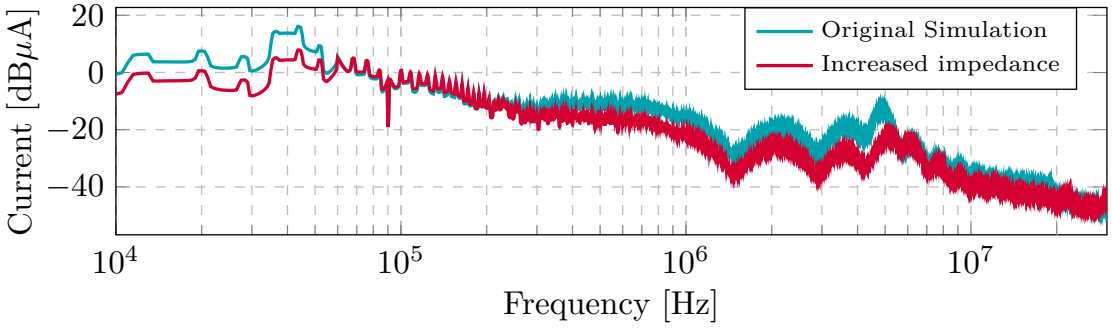

(b)

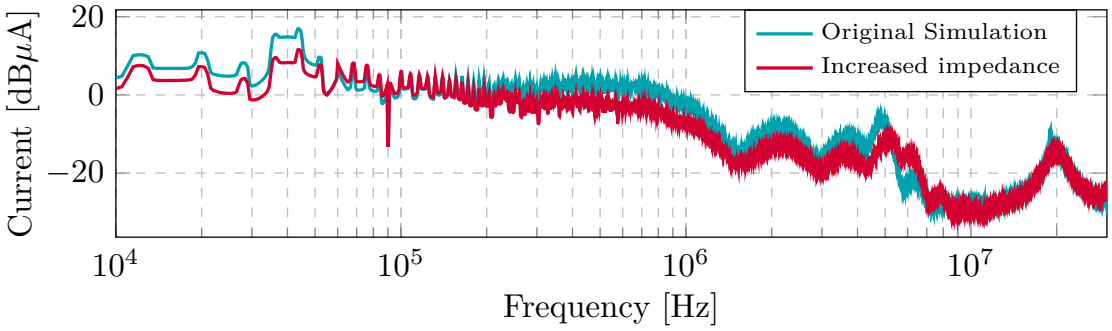

(c)

Figure 4.22: Influence of the electric motor's impedance on Grid CM Current. Simulation results. (a) Impedance change; (b) Motor CM current;(c) Grid CM current.

It can be seen that this small impedance change causes a decrease in the common-mode current at the motor terminals, as well as at the power supply input. Although the decrease at the grid input is smaller, this test confirms that the impedance of the machine has an influence on the system, and it is possible to modify its behaviour by modifying the machine. For this purpose, an analysis of the design parameters will be carried out in the next chapter.

4.5 MODELLING OF THE FILTER

After confirming the full drive's functionality and the machine's impact, it is necessary to verify compliance with the EMC standards specified by EN 12015. Even if the current is measured with a current RF probe, the regulations are defined by the emissions in dBμV, because they are usually measured by Line Impedance Stabilisation Networks (LISN). Therefore, to convert dBμA to dBμV a constant impedance of 50 Ω is used in all frequency ranges, as it is the standard impedance for RF measurements. As can be seen in Figure 4.23, the current exceeds the regulations at the connection point of the grid, which can interfere with other elements connected to the grid.

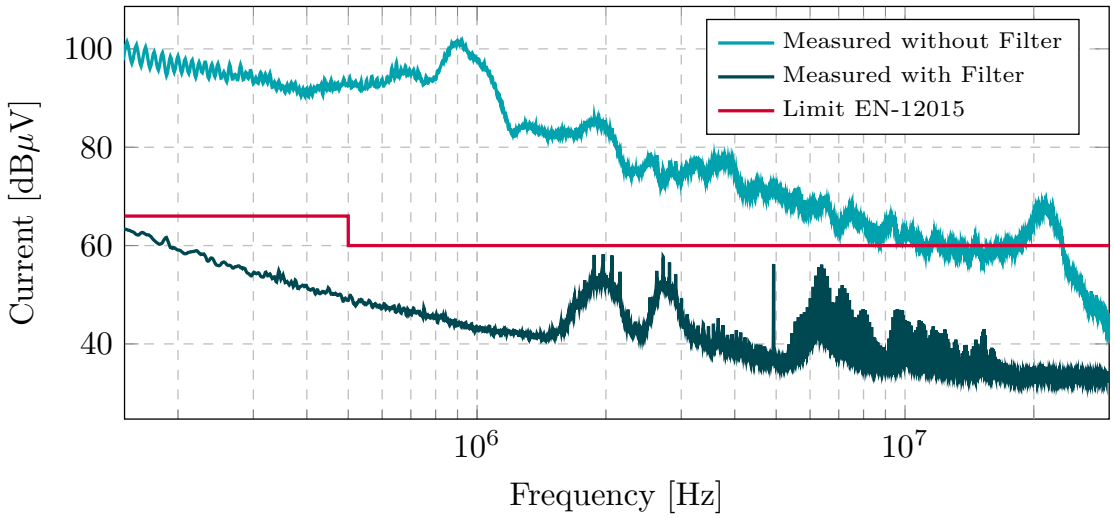

Figure 4.23: Grid current with and without EMC filter. Experimental measurements.

To solve this problem and comply with the regulations, the filter shown in Figure 4.24 is introduced between the converter and the grid, filtering the current emission to the grid as shown above. As mentioned before, this adds a new component, weight, volume and cost to the electric drive, but does not solve the root problem; it just mitigates the consequences.

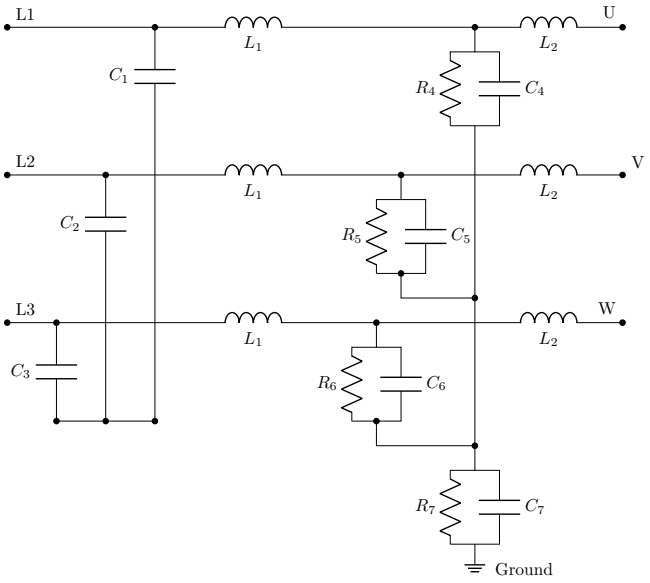

Figure 4.24: Electric circuit of the EMC filter

The model was calibrated with the impedance measurements of a phase, phase-to-ground in the input, and phase-to-ground in the output, as was done with the converter previously. The resulting calibrations are shown in Figure 4.25.

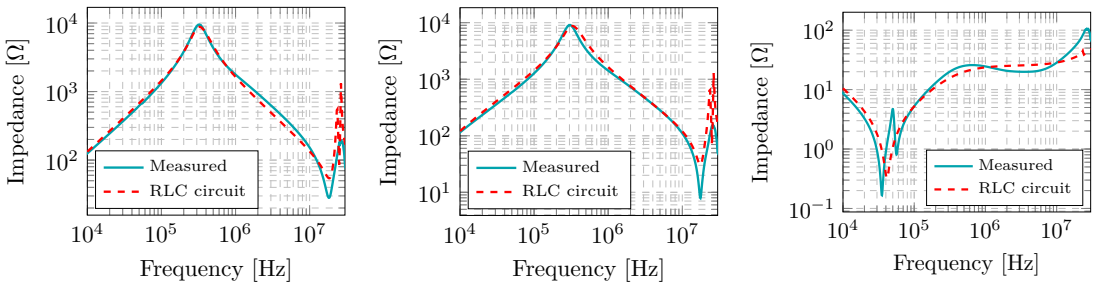

Figure 4.25: Filter impedance. Experimental vs. Simulation results: (a) Z_{L1-U}; (b) Z_{L2-g}; (c) Z_{U-g}.

4.5.1 Validation

In Figure 4.26, the CM current for the motor is depicted using the filtered drive model. Generally, the simulation results are consistent with the actual measurements, with the exception of resonances occurring between 1.5 to 5 MHz, which were also observed in the CM voltage at the motor's input in the unfiltered model.

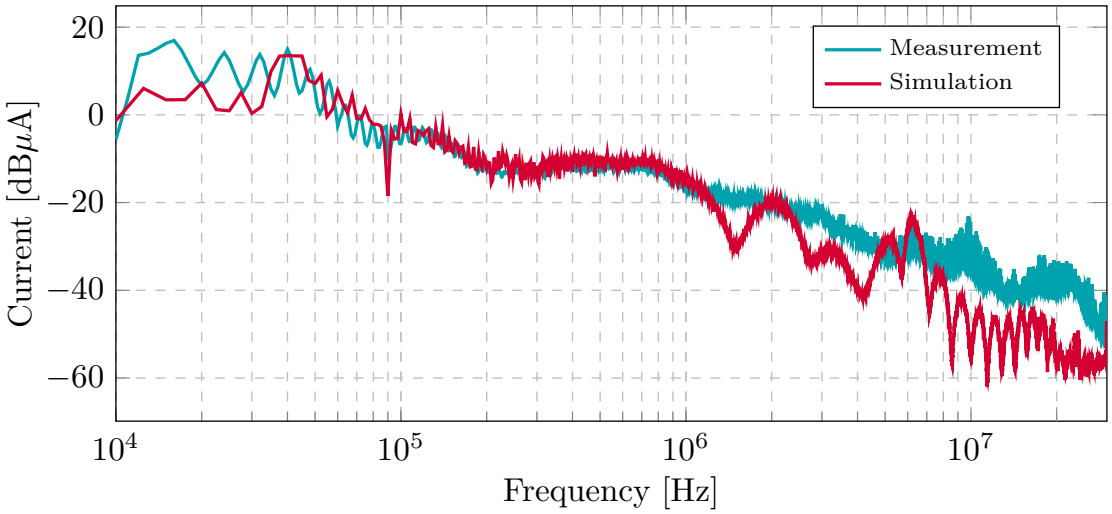

Figure 4.26: Common mode currents on the Motor. Experimental vs. Simulation Results.

Then, the current input of the grid is confirmed in Figure 4.27. Similarly to earlier observations, the complete spectrum is consistent with the measurements, although it lacks the minor resonances that were absent in the motor input voltage and are not observed in the final grid current either. It should be noted that the difference between the measurement and the simulation from 10 to 100 kHz is due to the noise of the probe, as mentioned in Figure 4.2b.

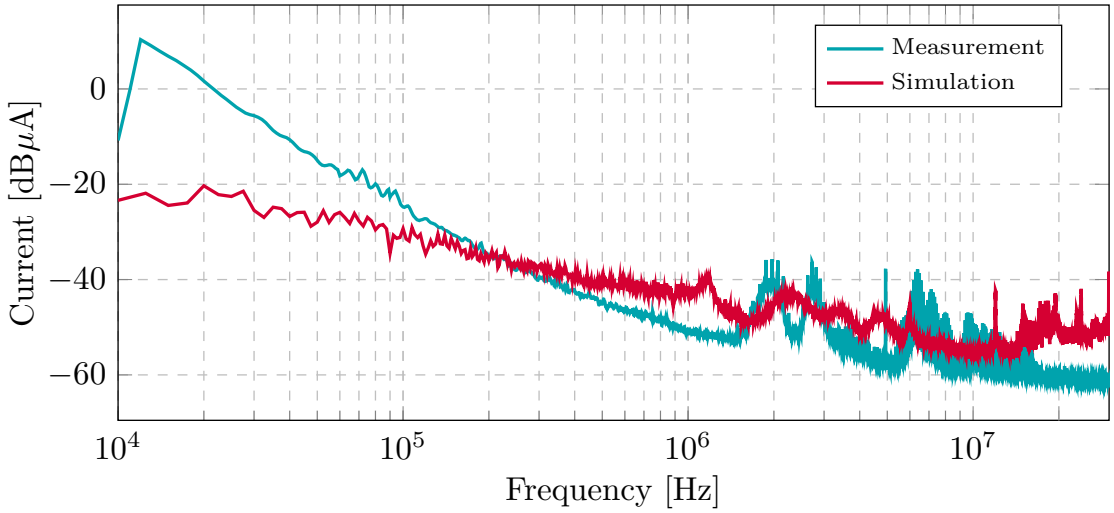

Figure 4.27: Grid input CM current with filter. Experimental vs. Simulation Results.

Finally, the current in the input of the grid is illustrated in dBμV to check the standard limit of EMC emission. The simulation with a filter is compared to the one without it in Figure 4.28. It can be seen that the current without filter is outside the standard.

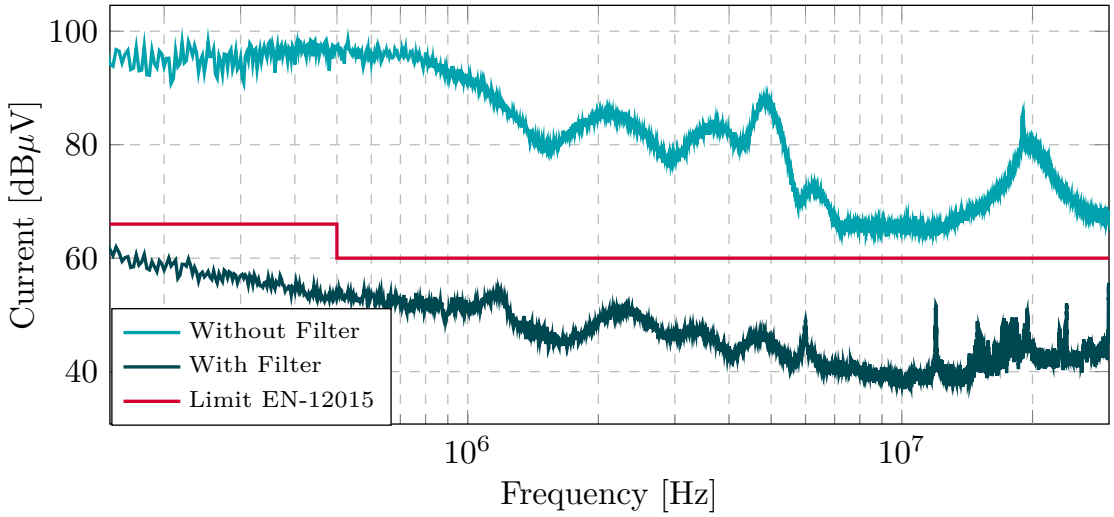

Figure 4.28: Grid input CM current comparison with or without EMC filter. Simulation results.

Chapter 5

MACHINE DESIGN SPECIFICATIONS

In this chapter, the design variables are analysed in order to evaluate their influence in the CM impedance of the electrical machine. Then, the variables that contribute the most to CM impedance are optimised and included in the general design methodology of electrical machines. Finally, a case study is proposed to apply those design specifications.

5.1 ANALYSIS OF DESIGN VARIABLES

In order to define design specifications for a EMC behaviour of the electrical machine, it is necessary to determine which design variables influence the impedance of CM more, since it is the one that defines the CM current in the machine and the CM current flowing to the grid, as concluded in the previous chapter.

Design of experiments (DoE) is employed to investigate the influence of various design variables on the CM Impedance. It is a branch of applied statistics that deals with the planning, conducting, analysing, and interpreting controlled tests. These tests evaluate the factors that control the value of a parameter or a group of parameters. The process is shown in Figure 5.1.

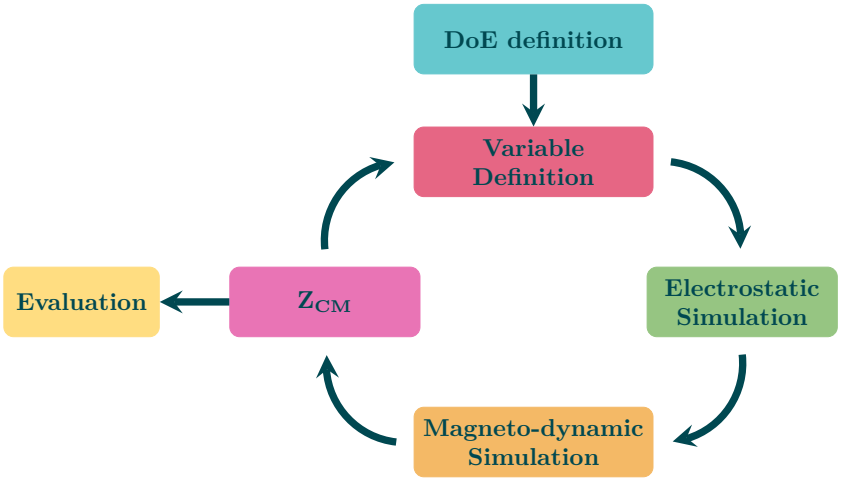

Figure 5.1: DoE procedure.

Based on the literature review presented in chapter 2, the design variables analysed and their range are described in Table 5.1.

Table 5.1: Analysed design parameters

Parameter	Original Value	Minimum value	Maximum value
Insulator permittivity	4.7	3.7	5.7
Insulator thickness	0.071 mm	0.06 mm	0.08 mm
Impregnation Permittivity	4.5	3.5	5.5
Liner	0.3 mm	0.1 mm	0.9 mm
Stack length	125 mm	100 mm	150 mm
Conductor Diameter	1.53 mm	1.4 mm	1.7 mm
Lamination Thickness	0.65 mm	0.58 mm	0.72 mm
Lamination permeability	100	90	200
Winding Configuration	Series	Series vs. parallel compared outside of the DoE	

The original value of each design variable is taken as a reference, and then the values are increased and decreased to check their influence on the CM impedance.

In Figure 5.2, a slot can be seen in the machine, which represents the design variables analysed.

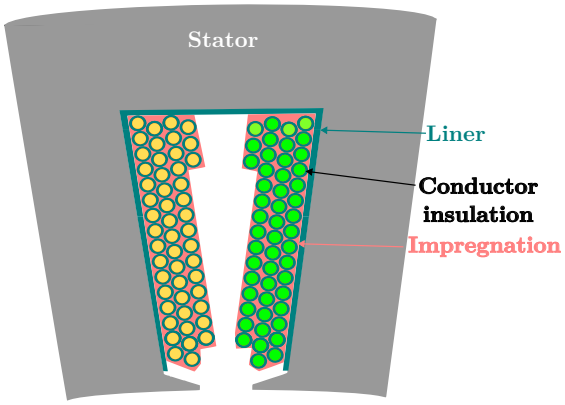

Figure 5.2: Analysis of the slot.

In addition, the winding configuration is analysed by comparing the series connection vs. a parallel one in the concentrated winding. This is done outside the DoE, due to its complexity.

For the result evaluation, an output must be defined. In this case, two outputs are defined, the maximum impedance value and the resonance frequency. Regarding the number of tests to perform, a Resolution IV fractional factorial design is used to efficiently explore the effects of eight variables on the system. This design allows for the testing of each variable at its minimum and maximum levels, allowing observation of the main effects of each variable and their low-order interactions.

The main effects represent the impact of each individual variable on the CM impedance when all other variables remain constant. Low-order interactions represent the combined effect of two or more variables on the impedance. By choosing a Resolution IV design, it is ensured that the main effects are not confounded by two-factor interactions, providing a clear understanding of the behaviour of the system. This design offers a practical and efficient approach for gaining maximum insights with a manageable number of tests when dealing with multiple variables.

In Figure 5.3 the DoE results are shown, where the contribution of each variable analysed to the CM impedance value can be seen.

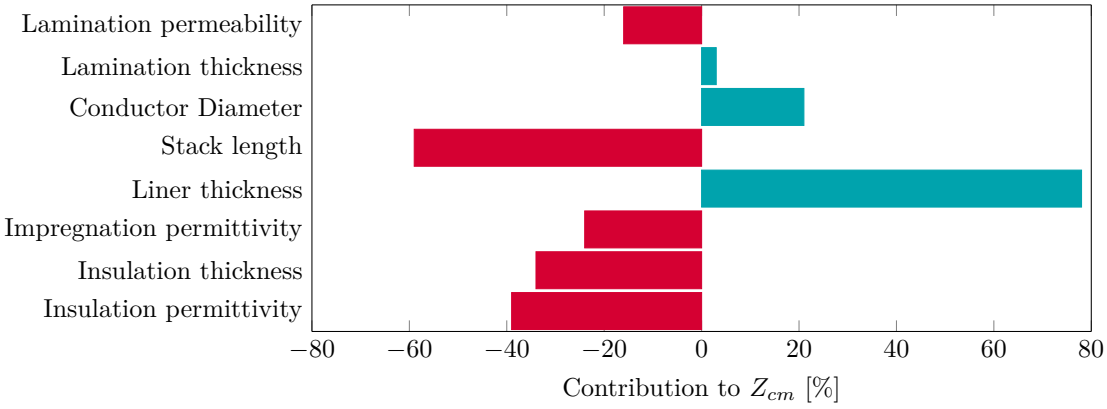

Figure 5.3: Contribution of each parameter to the machines's CM impedance.

In the diagram, there are positive and negative contributions. Positive means that if the variable value increases, the impedance will increase as well, whereas negative means that if the variable increases, the impedance decreases.

With regard to the values, it can be seen that the variable that most affects the value of the CM impedance is the thickness of the liner.

It must be remarked that even if the stack length also appears to have a big contribution, it is not straightforward, as the change of length would require changes in the winding properties (number of turns, diameter of conductors..) and would change the main requirements of the machine, as the nominal torque and current. This is analysed in the section below.

5.1.1 Stator length

The comparison of the simulated CM impedance of two different stator lengths is shown in Figure 5.4. The original machine is 125 mm long, and the shorter machine is 100 mm long. To maintain the requirement discussed above, the number of turns is increased, and the diameter of the conductor is decreased to maintain the filling factor.

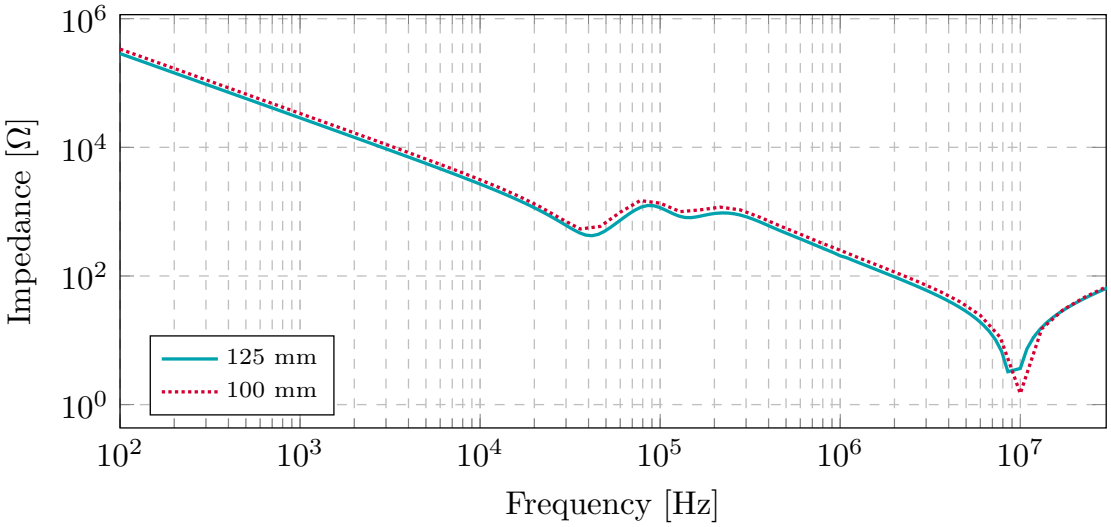

Figure 5.4: Influence of stator length in CM impedance. Turn number and conductor diameter adapted. Simulation results.

As can be seen in the figure above, the impedance increases slightly. However, the effect of an increase in length is counteracted by the decrease in the diameter of the conductors, minimising the desired effect.

With respect to conductor diameter and insulation thickness, they are related, as regulations define the minimum and maximum insulation thicknesses for each wire diameter and class. Furthermore, increasing the conductor diameter will also increase the conductor losses, in addition to an early skin effect. Thus, seeing the results, the optimisation will begin with the liner modification, not the length.

5.1.2 Winding circuit

Beyond the contribution analysis conducted, the series and parallel winding configuration is depicted in Figure 5.5 with respect to the CM impedance.

The series winding consists of twelve coils per phase, whereas the parallel one consists of six coils in parallel with the other six per phase. As can be seen, including parallel circuits

decreases the impedance after resonance, leading to higher CM currents. Thus, the first design criteria can be established. Parallel circuits should be avoided whenever possible.

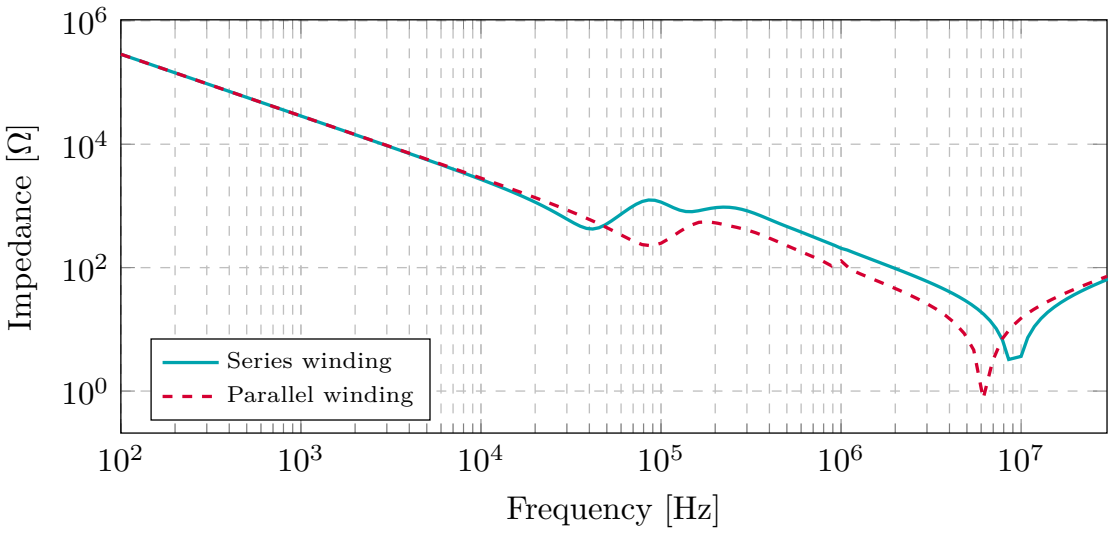

Figure 5.5: Comparison between series and parallel winding configurations. Simulation results.

This analysis has also been carried out experimentally, winding one phase of a small-scale stator shown in Figure 5.6. It is manufactured with M800-65A electrical steel, with a stator length of 53 mm. The different parameters of the windings are shown in Table 5.2.

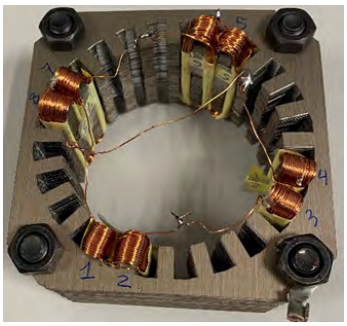

Figure 5.6: Small-scale stator with a phase formed of 2 parallel circuits.

Table 5.2: Parameters of the wounded coils

Circuit	**Coils**	**Turns per Coil**	**Conductor Diameter**
Series	8	50	0.5 mm
Parallel	4//4	100	0.35 mm

The resulting phase impedance is shown in Figure 5.7a. As expected, the parallel winding has a higher impedance due to the higher number of turns and lower winding diameter.

The impedance from the phase to the stator in the small stator is shown in Figure 5.7b. Under these circumstances, the impedance associated with the parallel circuit winding exhibits a lower value than the series one. The same prediction was accurately made by the model delineated in Figure 5.5 for the entire motor analysed.

This observation, in the first instance, substantiates the hypothesis that a parallel circuit contributes to a reduction in the machine's CM impedance. In the second, it validates

the applicability of the HF impedance model, presented in chapter 3, for the purpose of analysing design parameters, given its ability to discern modifications.

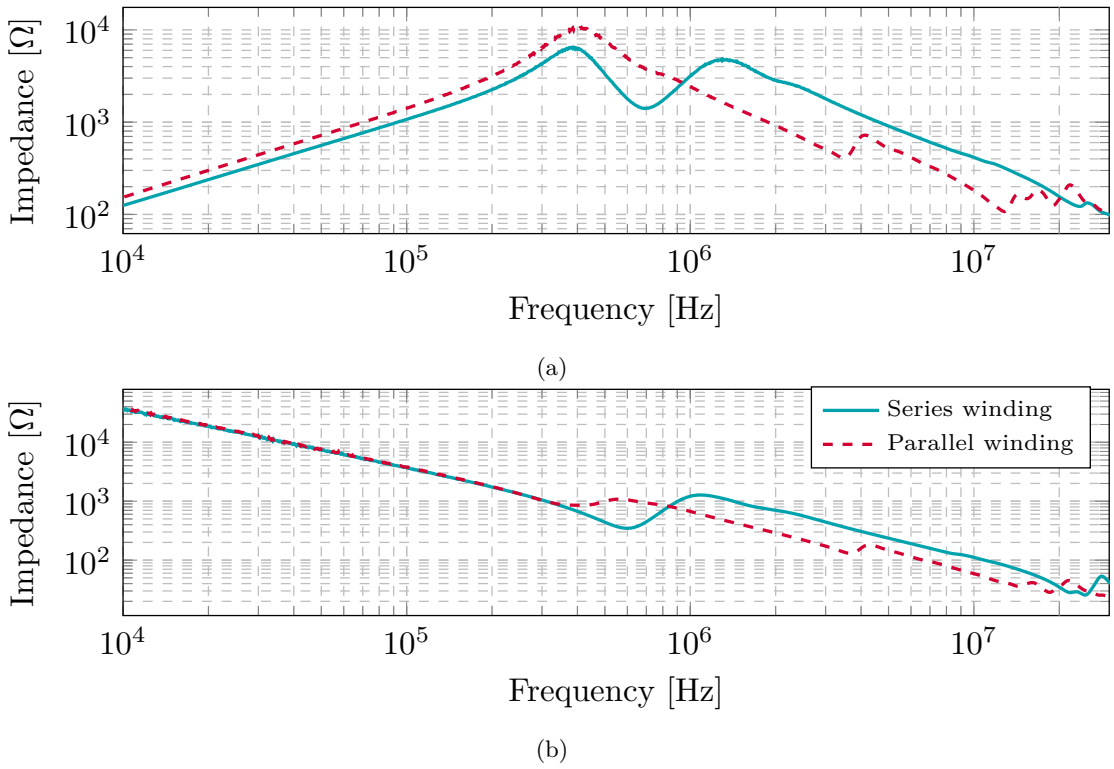

Figure 5.7: Comparison of series vs.parallel circuits. Experimental measurement. (a) Phase impedance; (b) Phase-to-stator impedance.

5.1.3 Optimisation of the liner thickness for CM current minimisation

Taking into account the contribution of each analysed design variable, the optimisation test is carried out to increase the CM impedance with the thickness of the liner. The maximum liner thickness that can fit the slot while maintaining the original winding and conductor disposition is 1 mm, so the comparison is the following: 1 layer of 0.3 mm liner vs. 3 layers of 0.3 mm, making a full liner of 0.9 mm. The resulting impedance is shown in Figure 5.8.

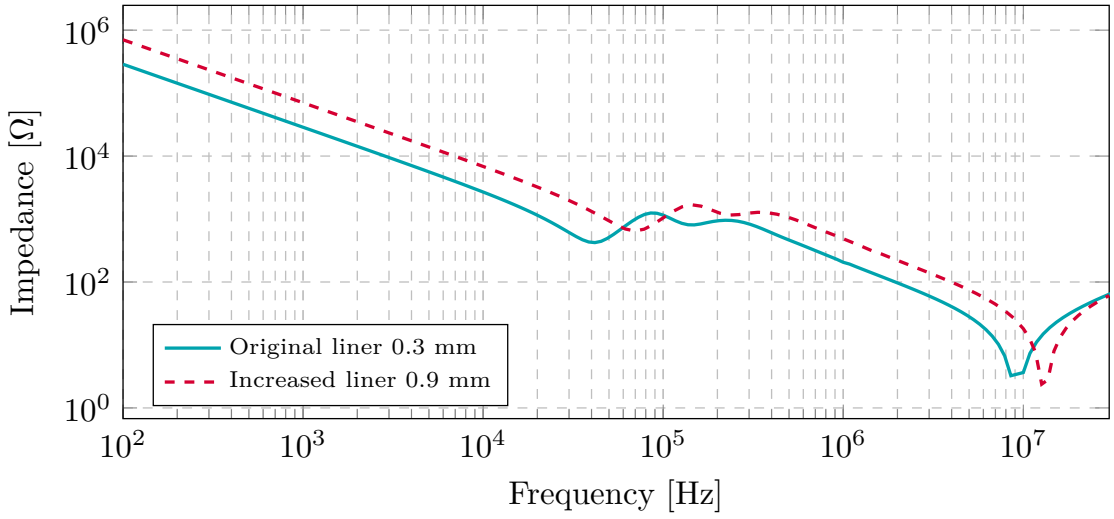

Figure 5.8: CM impedance optimization increasing the liner thickness. Simulation results.

It can be seen that the CM impedance increases considerably over the whole frequency range, just adding 2 more liner papers, or using a thicker one. Furthermore, it is confirmed that incorporating the machine with additional liner to the electric drive will reduce the CM current at the motor's input, as illustrated in Figure 5.9.

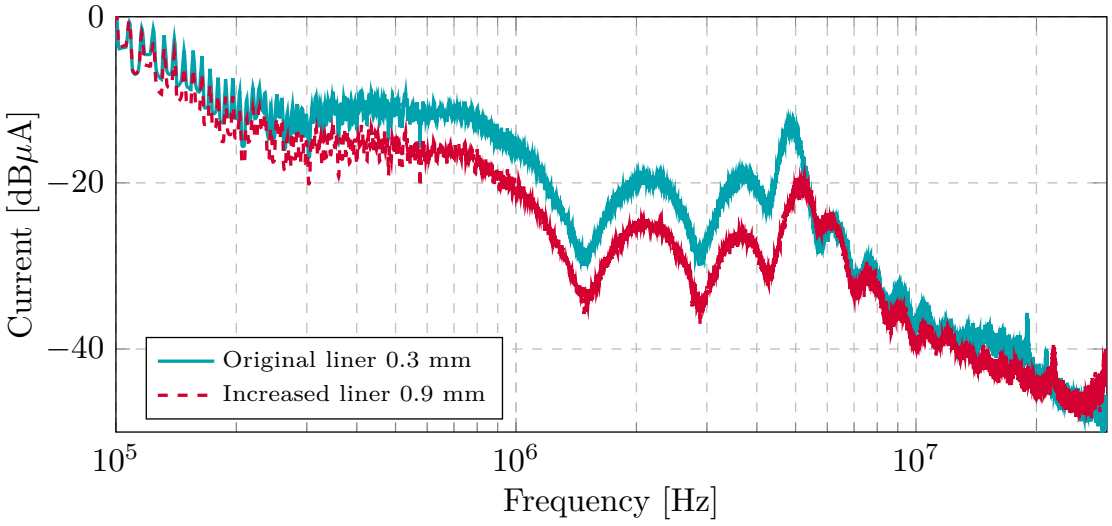

Figure 5.9: Motor CM current optimization increasing the liner thickness. Simulation results.

Then, in Figure 5.10 the current in the grid input is compared with the EMC standard limit, and a current decrease is observed, even if not enough to comply with the regulations. However, it can be a starting point for decreasing the filter size.

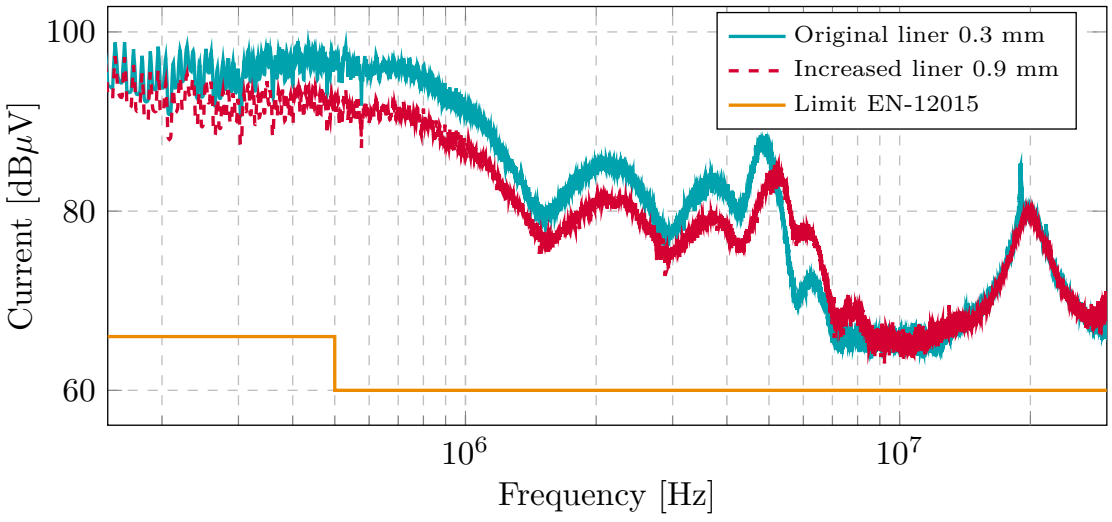

Figure 5.10: Grid CM current optimization increasing the liner thickness. Simulation results.

5.2 DESIGN METHODOLOGY

The general process for the design methodology of electrical machines is shown in Figure 5.11, from the specification stage to the manufacturing process. This is based on the methodology proposed in [117].

Figure 5.11: General design methodology of electrical machines [117].

5.2.1 Specification stage

Initially, it is essential to establish the design specifications of the electrical machines. This involves conducting a thorough analysis of various operational factors, such as speed and torque prerequisites, operational cycles, and working conditions. It is also important to consider environmental factors, mechanical limitations related to placement, and available space for installation. In addition, other design criteria, such as expenses, material selection, and manufacturing procedures, should also be considered.

As an additional specification to the above-mentioned, the EMC emission limits should be defined for the specific application. In the analysed case, this is ruled by EN 12015, but each application may have its own regulations.

5.2.2 Design stage

The design phase is an iterative procedure that includes three primary stages. They are shown in Figure 5.12, showing in red the specific steps proposed in the PhD.

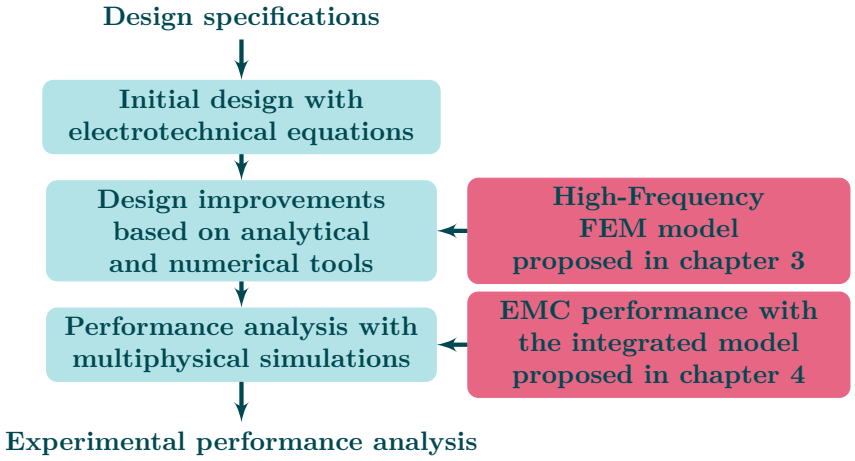

Figure 5.12: Proposed Design stage process.

Fist, an electromagnetic design of the motor is carried out using standard electrotechnical equations, focusing solely on average values and not taking into account harmonics or torque ripple. This preliminary design stage involves choosing the appropriate topology, determining the machine's size, and designing the magnetic (poles and slots, magnet grade...) and the electrical circuits (ampere turns, winding...).

Second, analytical tools are used to improve the pre-design from the stage above. It can consist of mathematical models or commercial software. These tools speed up machine

design, so it is advisable to use them as much as possible when their accuracy is adequate. Then, the design of the machine is fine-tuned using precise numerical tools based on FEM software. With the use of these tools, machine performance is scrutinised with precision, considering nonlinearities, detailed geometrical shapes, and field distributions, avoiding the simplifications used in analytical tools.

In this step, in order to consider the high-frequency behaviour of the machine, the HF FEM model of the machine should be included, as presented in chapter 3. Taking into account the other machine specifications, the CM impedance of the design should be maximised in order to decrease the resultant CM current.

Finally, the iterative design process culminates in the analysis of machine performance. This phase consists of multiphysic cosimulations to examine the overall operation of the drive system.

In this last step of the design process before prototyping, the fully integrated drive model presented in chapter 4 should be used, to obtain a general view of the EMC behaviour of the drive. In this way, if the drive CM conducted emission is higher than the allowed by the standard, the motor impedance can be increased if possible, or otherwise, the filter can be resized according to the actual need, keeping its size to the strictly minimum.

5.2.3 Performance analysis

If the performance of the machine shown in the simulations is favourable, a prototype is manufactured and experimentally tested. Habitually, electromagnetic, vibro-acoustic, and thermal performances are analysed. A key objective of the developed work is to minimise the use of prototyping. However, the experimental validation of the design is not neglected, creating a prototype that is validated experimentally. The final step in the performance analysis phase is the validation of the machine in its actual application.

It must be remarked that even if the integrated drive model is used to analyse the EMC performance of the drive, verifying this performance in the actual application is advisable, as external devices or elements may interfere with the drive and increase some emissions at high frequencies.

5.3 CASE STUDY

In this section, a practical case of design methodology is presented. Instead of following the full design process, this section is focused on the high-frequency behaviour design of the machine, from the HF machine impedance model to the EMC performance of the drive. Two machines are obtained from the design specifications and the parameters are shown in Table 5.3.

Table 5.3: Parameters of the studied Machines.

Machine	Ω [rpm]	Torque [Nm]	Coils per Phase	Turns per Coil	Conductor Diameter	Circuits
M1	166	400	8	64	2×1.5 mm	Series
M2	255	400	8	78	2×1.3 mm	Parallel

As mentioned above, using parallel circuits is not recommended, as they have a lower CM impedance, which will increase the CM currents. However, in this case, it is necessary. In fact, increasing speed while maintaining torque means higher power, leading to a current increase in the winding. To cope with a higher current, the section of the wires must get bigger, limiting the number of turns due to the filing factor, and compromising the manufacturing process of the coils, as the bigger the wire, the less ductile. Therefore, parallel circuits are used to reduce the current load on each conductor, thereby preserving the filling factor and ensuring a manageable diameter for the conductors.

5.3.1 Machine high-frequency Impedance

Once the pre-design of the machine is made to meet the electromagnetic performance specifications as shown in Table 5.3, the high frequency FEM model should be used to evaluate the CM impedance of the machines and propose some design changes for the high-frequency performance improvements. In Figures 5.13 and 5.14 the impedances of both machines are compared with their measured impedance.

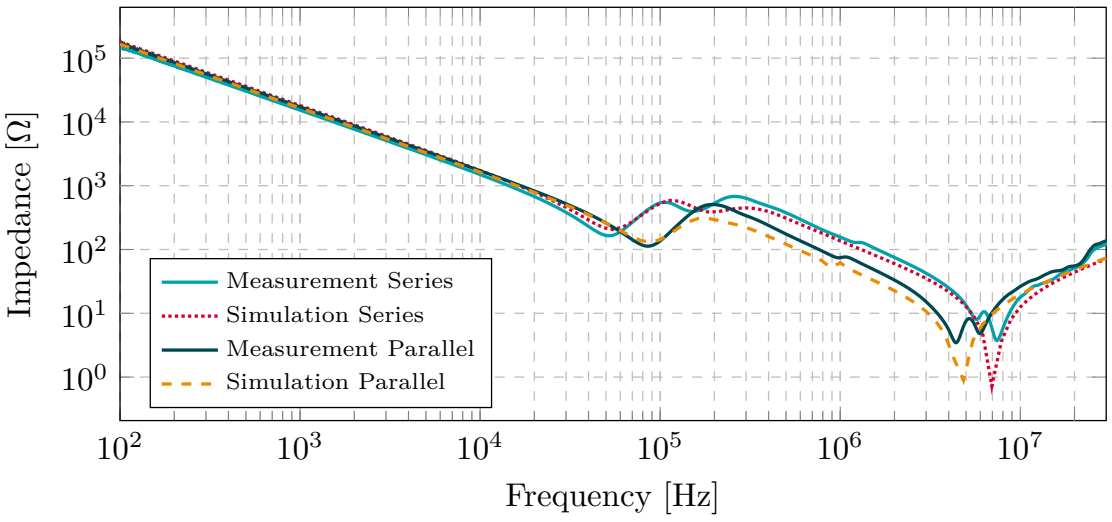

Figure 5.13: CM impedance of the studied machines. Experimental vs. Simulation results.

In Figure 5.13, the FEM simulation impedances exhibit a precise correlation with the CM impedance measurements of the two machines under study. Furthermore, the

discrepancy in the impedance ranging from 60 kHz to 10 MHz between the two machines is accurately represented by the FEM model.

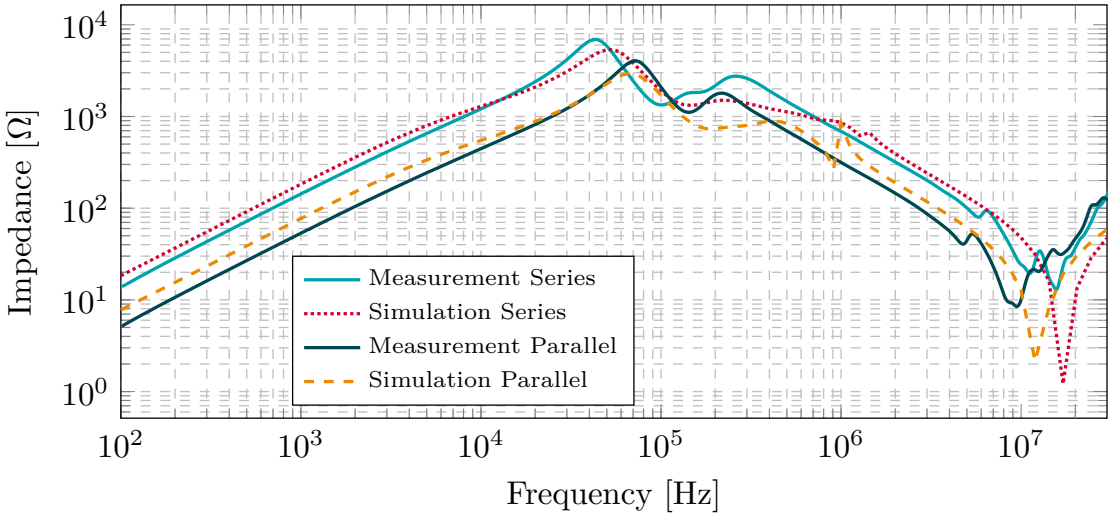

Figure 5.14: DM impedance of the studied machines. Experimental vs. Simulation results.

As depicted in Figure 5.14, the FEM simulated impedances manifest a precise correlation with the DM impedance measurements of the two machines under examination. Even if the accuracy of the models is lower around 200 kHz, the differences between the two machines are clearly represented by the model. In this case, the DM impedance of the parallel machine is lower in the whole spectrum, as expected because of its lower resistance and inductance.

5.3.2 Common-mode currents

The impedances calculated by FEM are introduced in the time domain model of the electric motor, and the overall electric drive system is simulated. As a results of these simulations, the CM currents at the motor terminals are shown in Figure 5.15 and the CM currents at the grid input are plotted in Figure 5.16.

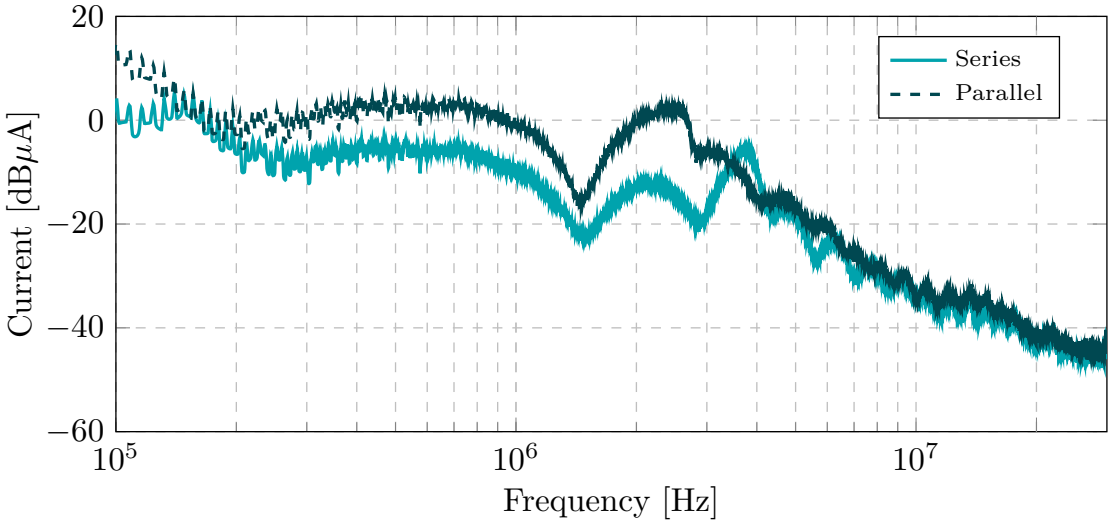

Figure 5.15: CM current of the studied machines without EMC filter. Simulation results.

It can be seen that the parallel winding CM current in the motor input is higher from 200 kHz to 3 MHz, as well as in the grid input, even if the difference is lower.

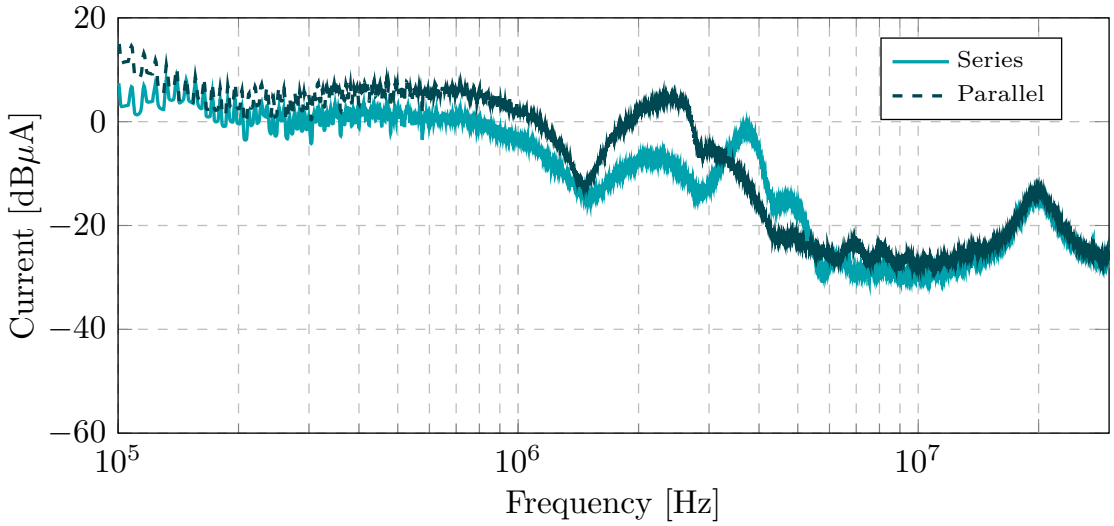

Figure 5.16: CM current computed by simulation at the connection point of the grid without EMC filter.

5.3.3 Proposed Design Improvement

As explained in the previous section, increasing the liner would increase the impedance of the motor and then would decrease the CM current, so this is applied to the analysed parallel winding machine in Figure 5.17.

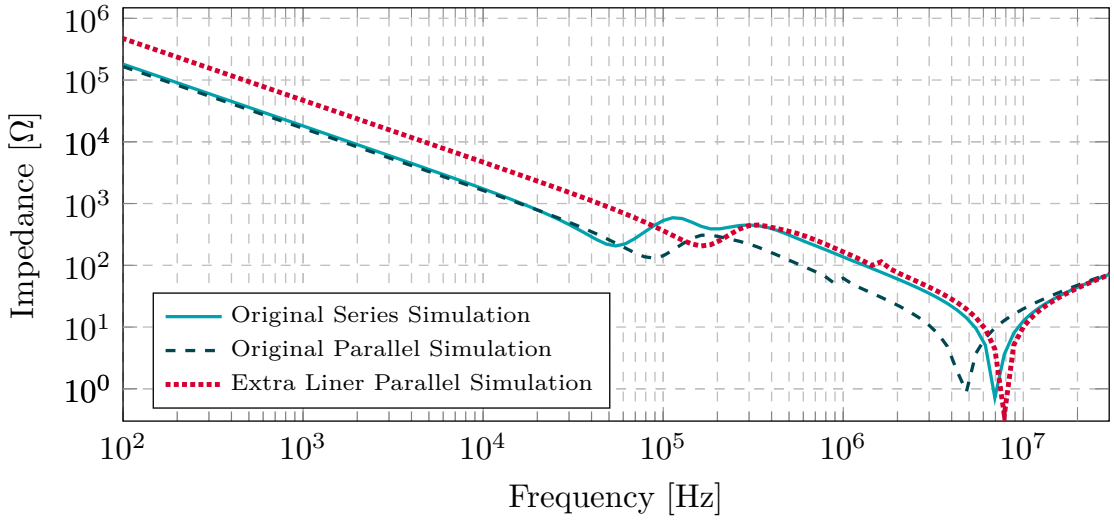

Figure 5.17: CM impedance of the optimised machine. Simulation results.

It can be seen that the resultant impedance is considerably higher than the series winding machine from 100 Hz to 100 kHz, and a bit higher from 150 kHz to 10 MHz. Thus, this change is analysed in the complete drive model to verify the CM current behaviour in Figure 5.18.

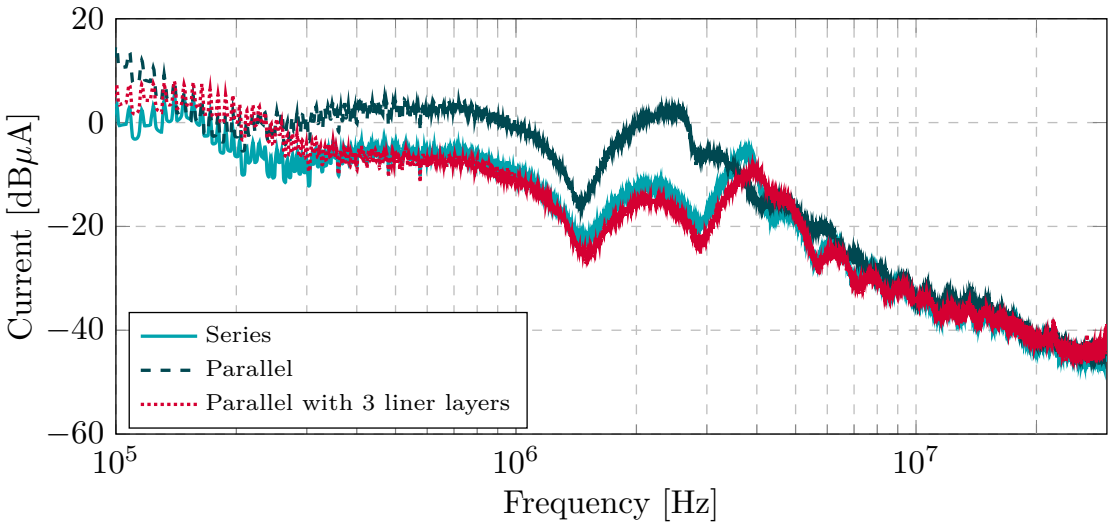

Figure 5.18: CM current of the optimised machine without EMC filter. Simulation results.

A considerable decrease of the CM current is obtained, equaling and even minimising the series winding machine current from 200 kHz to 10 MHz.

The same effect can be appreciated in Figure 5.19, even if the effect is minimised from 10 to 30 MHz, due to the CM currents flowing through the parasitic coupling of the inverter and the cable to the grid. However, the current is reduced by 10% at around 2 MHz.

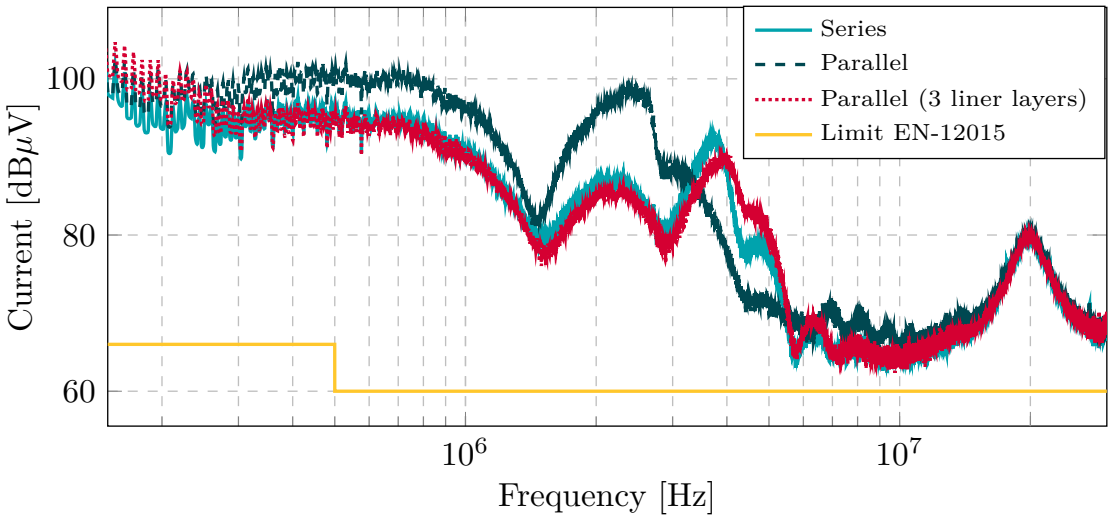

Figure 5.19: CM current at the grid input without EMC filter. Simulation results.

Overall, these results suggest that increasing the impedance of the machine decreases the CM current in the machine input, as well as on the grid input of the whole drive, improving the drive EMC behaviour. However, the decrease is not enough to comply with the EMC regulations without a filter.

In addition, the simulations of the analysed machines are conducted with the EMC filter in the drive. The current obtained at the input terminal of the grid is depicted in Figure 5.20. It is evident that the machine with parallel circuits exhibits two resonances at 1 and 2 MHz, which are higher than those of the other two machines. The first resonance even reaches the EMI limit. Therefore, the incorporation of additional liner layers mitigates this resonance by approximately 5 dBμ V, thus preventing the exceeding of the limit.

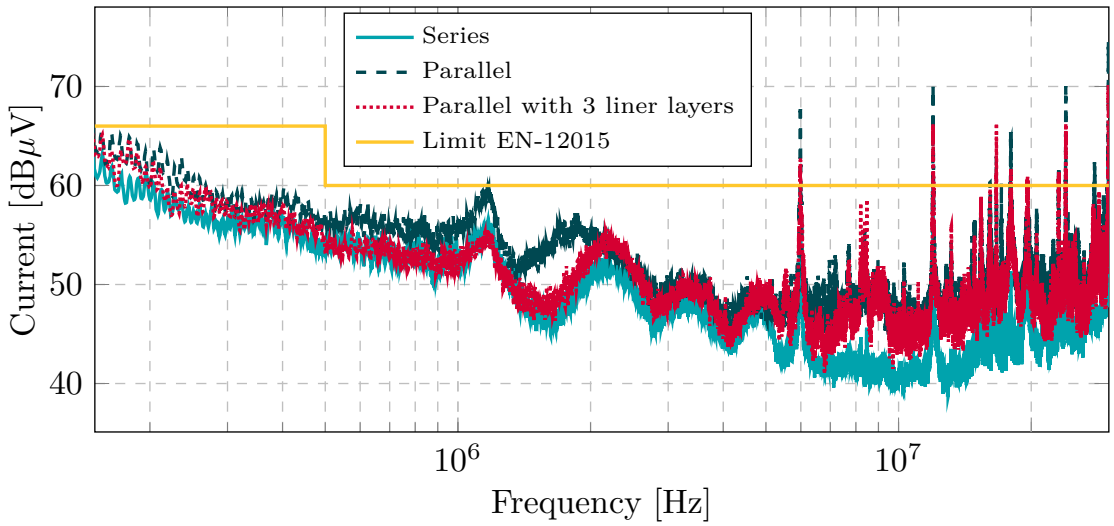

Figure 5.20: CM current at the grid input with EMC filter. Simulation results.

Furthermore, as can be seen in Figure 5.21, the voltage overshoot in the parallel winding machine is 14 %, which does not imply a significantly high peak voltage in the machines studied (a peak voltage of 320 V). However, for higher bus voltage levels, this overshoot could result in a risky voltage level for winding insulation [118]. As mentioned in [119], this overshoot could result in partial discharge (PD) activity, which is one of the common causes of motor winding insulation failure.

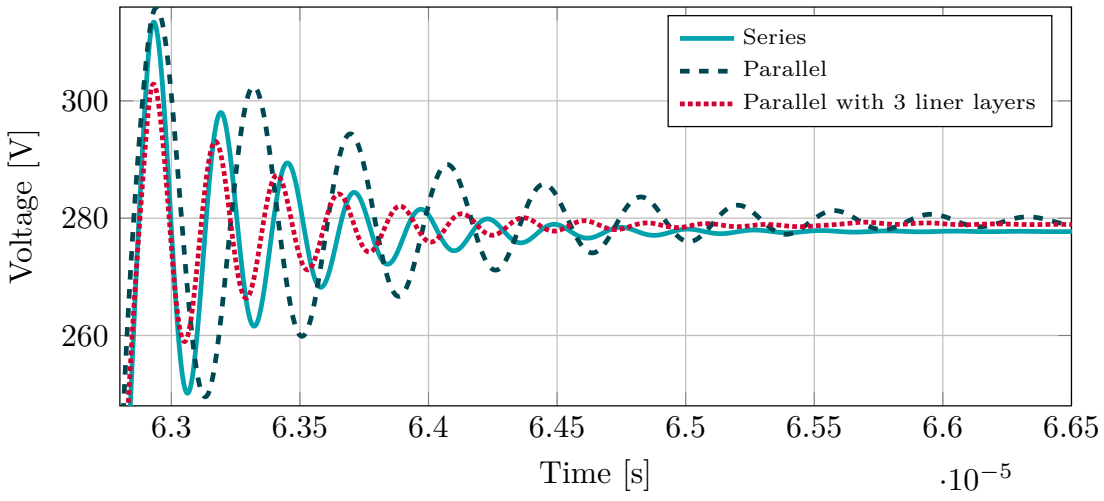

Figure 5.21: Motor terminal phase voltage pulse in the studied machines. Simulation results.

In fact, PD refers to a phenomenon in which electrical discharges occur within the insulation of electrical equipment, such as motors, without completely bridging the space between conductors. These discharges can degrade the insulation material over time, potentially leading to insulation failure. Thus, reducing discharges will increase insulation lifetime.

Hence, reducing or removing the overshoot could help to avoid PD activity and consequently increase the insulation lifetime. Interestingly, the overshoot obtained in the machine with the 3 liner layers decreases the overshoot by 4 % from the original machine. Thus, considering higher bus voltages, the inclusion of the extra layer may minimise partial discharge probability thanks to the reduction of the overvoltage.

In addition, the time that the voltage takes to stabilise in the bus voltage value is lower in the machine with the extra liner layers, minimising the ringings. According to [120], the less ringings occur, the lower the probabilities of partial discharge.

Altogether, including the extra liner layer can, on the one hand, decrease the CM current in the drive, reducing the conducted EMI, and, on the other hand, increase the lifetime of the insulation, as the PD probabilities may decrease. This is an interesting starting point for future research.

5.3.4 Experimental validation

In order to evaluate the impact of an increase in the thickness of the liner in the electrical machine, the impedance of one coil of the machine is measured. In Figure 5.22, the measured coil is shown, with 3 liner layers as outlined in the design stage to increase the CM impedance.

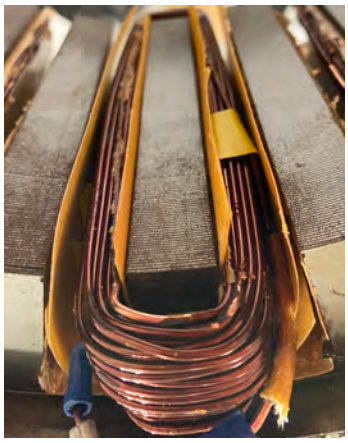

Figure 5.22: Coil with 3 liner layers of 0.3 mm each.

Then, in Figure 5.23, the coil-to-stator impedance is illustrated, comparing the impedance with different liner thicknesses. The original 0.3 mm liner obtains the lowest impedance, whereas including 3 of this papers, until 0.9 mm thick, increases the impedance substantially.

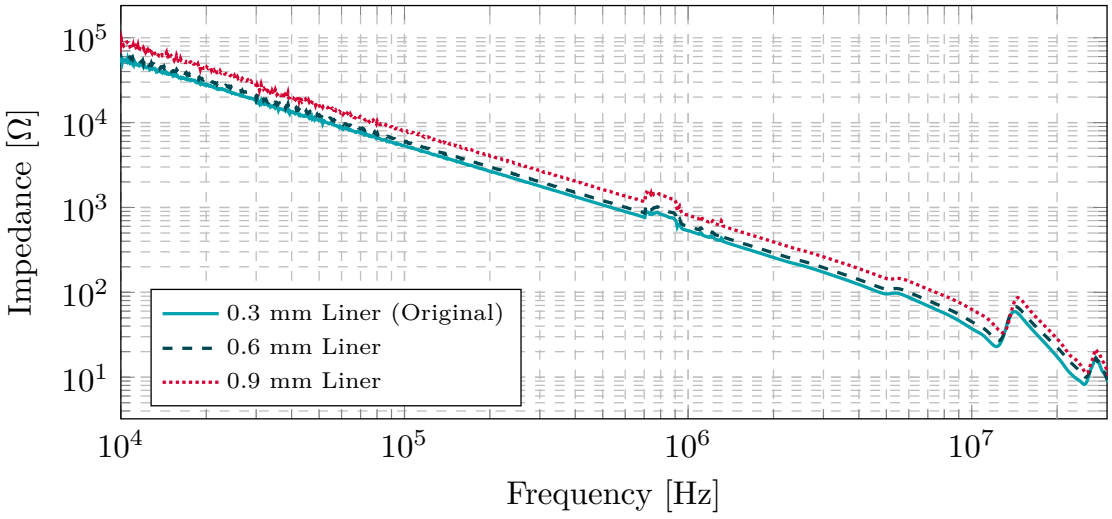

Figure 5.23: Effect of liner thickness in a CM impedance of a coil. Experimental measurement.

In the absence of a physical prototype of the electrical machine analysed with an increase in liner thickness, the validation of the design improvement was achieved through a two-step process. The first step involved the analysis of the coil-to-stator impedance of a single coil as shown in Figure 5.23. The observed increase in this impedance served to validate the increase in the common-mode impedance, a critical parameter in the operation of the machine.

The second step of the validation process was based on the full-drive model experimentally validated in the previous chapters. A key observation was the decrease in the CM current concurrent with the increase in impedance. This inverse relationship between CM current and impedance further supported the design improvement of the machine. Therefore, even without a physical prototype, the combination of these analytical observations provides a robust validation of the design improvement of the electrical machine.

Chapter 6

CONCLUSIONS AND FUTURE WORK

3 years and a half have already passed since the beginning of this PhD project. This is a long enough time to draw some sound conclusions. However, there are still many challenges and opportunities for further development. To finish the document, the main conclusions and some ideas for further work are listed in this chapter.

6.1 CONCLUSIONS

6.1.1 On the Fulfilment of the Initial Hypotheses and Objectives

At the beginning of the PhD, some hypotheses and objectives were defined, which have shaped the workflow of the last few years. In this section, their level of fulfilment and veracity are discussed.

The establishment of the design rules and the development of design and analysis tools that make it possible to improve the high-frequency behaviour and robustness of electrical machines, and indeed the high-frequency performance of the overall electrical drive, was defined as the main goal of the PhD. The goal is aligned with the structure of this document. The comparison between the existing high frequency analysis tools and modelling techniques was provided in Chapter 2, together with some influence of different design parameters on the HF behaviour of the machine. Chapter 3 focused on the FEM model developed for the analysis of the high-frequency impedance of electrical machines. For the full electric drive, Chapter 4 presented an integrated model of the electric drive that could predict the EMI behaviour of the overall system. The accuracy of both tools was experimentally validated with different industrial electric motors. With respect to the design parameters, their influence on the CM impedance was analysed in Chapter 5 to introduce some high-frequency-focused steps in the machine design methodology. Then a case study was presented and some design modifications were implemented successfully to reduce the CM current of an electric drive. Hence, overall, the main goal of the PhD can be considered accomplished at this stage. The following sections analyse the rest of the hypotheses and objectives.

6.1.1.1 *Veracity of the Hypotheses*

H1. *By adjusting the high-frequency behaviour of the electrical machine, the performance of the whole electric drive should be improved.*

This first hypothesis can be considered to have been verified by the case study presented in Chapter 5. The thickness of the motor liner was increased to increase the common-mode impedance, decreasing the common-mode current in the motor and at the connection point to the grid. The case study ended with a redesigned electric motor that was able to meet the demands of the application, reducing its common-mode current emissions.

H2. *By modifying the motor impedance, the lifetime of the bearings and the winding insulation would be increased, preventing unexpected and premature failures.*

Using the proposed design methodology and the variables analysed, the common mode currents from the motor to the ground can be attenuated. However, additional research is imperative to determine a reduction in bearing currents. Moreover, the voltage at the motor input appeared to decrease as a result of the additional liner in the slot, which consequently lowers the probability of partial discharges, thereby prolonging the lifetime of the winding. However, further empirical studies are required in this domain to derive a more definitive conclusion.

H3. *Knowledge of the high-frequency behaviour of electrical machines and the use of appropriate tools and methodologies for analysis and design could make possible the optimisation of the electric drive for each particular application.*

This hypothesis was also confirmed by examining the design variables shown in chapter 5, together with the suggested improved design methodology. The case study introduced at the end of the chapter further demonstrates that the tools developed can facilitate the optimisation of the electric drive for various applications.

H4. *Prototyping the electric drive with an optimised electrical machine would allow to evaluate the effectiveness and usefulness of the developed design methodology and tools, as well as the improvements obtained with respect to a conventional electrical machine.*

Although the study did not address a prototype with an optimised electrical machine, the developed model showed a clear reduction in common-mode current at the grid connection point by increasing the machine's CM impedance. This model was experimentally validated, so the results are sufficient to state that the EMC behaviour of the drive is enhanced with the increased liner. Additionally, a prototype of one coil is modified, increasing the liner layers to experimentally check their influence on the CM impedance, validating the increase in the CM impedance as predicted in the FEM model.

Thus, the work that was done during this project serves to prove this hypothesis in two steps: the impedance increase is experimentally validated, and the current decreases with the developed model, which was previously validated experimentally.

6.1.1.2 *Fulfilment of the Objectives*

In the beginning of the PhD, the following objectives were set to achieve the final goal of the thesis. The work of this thesis fulfilled the defined objectives as follows:

O1. *Reduce the EMI of the whole electric drive, without adding a filter by reducing the common mode current in the grid connection point.*

In the case study presented in chapter 5 the CM current delivered to the grid is reduced from 150 kHz to 3 MHz by adding 2 more liner layers to the machine analysed. The mayor decrease is produced in the range of 1-3 MHz, with a reduction of 10 dBμV. Thus, the objective is achieved. Furthermore, the emissions of the parallel-connected machine punctually exceeded the limit even with the EMC filter, and it is solved by adding the extra layer of liner, even reducing the emissions to those of a series-connected machine, about 5 dBμV less.

Based on these findings, it appears highly unlikely that the EMC filter can be eliminated solely by altering the motor design. This presents a significant challenge for future work in this area, as the change in the motor design can be used to reduce the filter size, even if not eliminating it.

O2. *Increase the reliability and robustness of the drive by reducing the common-mode current and the overvoltages in the motor terminals.*

The research and design methodology proposed during this thesis has successfully achieved an increase in the reliability and robustness of the drive system. In particular, the attenuation of the common-mode current has been effectively addressed. However, even if CM current attenuation positively impacts overall robustness, it does not directly guarantee a reduction in bearing currents. Further investigation may be necessary to specifically address bearing current issues, as well as to ensure the

winding lifetime expectation due to the overvoltage reduction at the motor input. However, the voltage overshoot has been successfully reduced by 4%.

O3. *Define a design methodology that also improves the high-frequency behaviour of electric machines.*

Chapter 5 presented a design methodology which includes the high-frequency models developed during this PhD, both the machine high-frequency impedance model and the full drive model. Using this methodology, the high-frequency behaviour of the machines can be analysed precisely and optimised.

O4. *Demonstrate the validity of the design tools and methodology in a practical case study by manufacturing and evaluating a prototype.*

The proposed new motor design in the case study presented in chapter 5 has not been finally manufactured due to lack of resources and time. Thus, the final validation of the proposed design has been conducted mainly in simulation. However, the developed models and the proposed design methodology have been completely validated by means of some conceptual motors and by means of 6 industrial electric motors. So it can be stated that the validity of the developed models and the proposed design methodology have been proved.

Moving on to more specific conclusions on some different topics that were analysed in the document, the following sections highlight the main points that can be extracted from the work of these years.

6.1.2 Literature Review on the High Frequency Behaviour of Electrical Machines

6.1.2.1 *High-Frequency Phenomena*

- In coil windings, skin and proximity effects increase with frequency, impacting resistance and inductance. These can be mitigated using smaller conductors and Litz wires, but effectiveness is reduced at high frequencies.
- For accurate capacitance calculations, it is crucial to know the properties of dielectric insulation materials. Variations in conductor positions during manufacturing can also cause discrepancies between theoretical and actual capacitance values.
- The end winding represents less than 1% of the winding-to-stator capacitance. However, it represents up to 40% of the total winding-to-rotor capacitance. Hence, it might be taken into account especially for modelling bearing currents, where the path through the rotor gains importance. Nevertheless, it might be neglected for the general high-frequency behaviour of the machine, as the common-mode currents are mainly established by the winding to stator capacitance.
- In magnetic cores, the presence of eddy currents is notable at high frequencies for their contribution to iron losses and the shielding effect they induce. Due to this shielding effect, the magnetic flux is pushed out from the magnetic core, decreasing the effective ferromagnetic material area and leading to a decrease in the value of the winding inductance. The lamination of the stator prevents the flux from being totally pushed out of the core, leading to a higher winding inductance compared to a bulk stator. However, once the skin depth is lower than the thickness of the sheet, more eddy currents are produced due to the proximity effect between the sheets.

6.1.2.2 *Analysis Tools*

- In FEM analysis of electrical machines, accurate modeling of detailed geometry is crucial for precise estimation of the resistance and inductance values, accounting for skin and proximity effects, and eddy current losses. Meshing is vital for accuracy, especially at high frequencies, where materials' skin depth must be finely meshed. However, detailed meshing increases computational load and a good trade-off between model complexity and accuracy must be found. Normally 2-D simulations might be accurate enough to analyse the active circuit of the motor, but occasionally 3-D simulations must be conducted to evaluate the contribution of the end-windings and the 3D effects that arise in the laminations. For electrostatic simulations in FEM, similar principles could be applied, although in this case rather fine mesh is required between the conductors to estimate precisely the turn-to-turn capacitice coupling. 3-D models are recommended for calculating the winding-to-rotor capacitance, due to the impact of the end winding.
- Analytical tools often require less computational load by making specific assumptions and simplifications, such as calculating the skin effect by reducing the conductor cross-section. However, accurately computing proximity effects is challenging because of the non-uniform magnetic fields, and methods like Bessel functions used for AC resistance calculations can lead to significant errors. Simplifications in the calculation of capacitances, such as the assumption of plate or cylindrical capacitors, often lack accuracy. In the turn-to-turn capacitance, some methods can reach acceptable results, but the method must be chosen depending on the specific disposition of the winding, otherwise large errors can appear.
- Measurement-based simulation models achieve good accuracy across the entire frequency range by adjusting the behaviour of the model. They are suitable for the modelling of already manufactured motors. These models normally are included in time domain simulations comprising the overall drive system, considering the high-frequency models of the motor, inverter, and EMC filter. But obviously, this approach is not suitable for predicting the behaviour of a novel motor in the preliminary design stage, as the prototype has not yet been built. There are two methods to obtain the values of the parameters included in these models: analysing the physical meaning of each parameter related to the impedance curve or using parameter fitting procedures that can yield even negative values.

In general terms, FEM tools are used for a detailed high-frequency analysis of electrical machines during the design stage. They take into account all high-frequency phenomena and obtain very accurate results provided that the geometry, the properties of materials, and the mesh are properly defined.

6.1.2.3 *Modelling*

- Typically, models can work either in frequency or time domain. Frequency domain models analyse parameters like CM and DM impedances across different frequencies. However, for simulating overvoltages and currents, time domain models are required. If frequency-dependent values are obtained from FEM simulations, equivalent RL branches can be derived using data-fitting methods.

- Depending on the specific objectives of the simulation, the constructed model may selectively emphasise or disregard certain components of the machine. Fundamentally, all models are constituted as RLC circuits, characterised by a variable number of segments and distinct physical meanings, even if, they all refer to winding self- and mutual inductances, resistance, and parasitic coupling capacitances. The inclusion of bearing capacitances depends on the analysis of bearing currents. Iron losses are occasionally integrated as a resistor in parallel to the winding, or alternatively, these losses may be implicitly represented within the circuit parameters.

- Concerning the rotor, its influence may only be significant when analysing bearing currents or shaft voltages. The rotor position is also important in the low-frequency range for salient-pole permanent magnet machines, as the inductance changes with the rotor position. However, the position of the rotor does not change the common-mode current of the motor, as it is induced at high-frequency.

- Generally, the models presented in the literature for electric motors have not been demonstrated to be accurate in the overall range of frequencies covered by the EMC standards (from 150 kHz to 30 MHz). All proposals found in the literature show rather good accuracy up to 10 MHz. It would be convenient to extend the precision range to 30 MHz. Furthermore, as technological developments in SiC and GaN devices increase the working frequencies, it is foreseeable that standards will increase the emission limits.

6.1.2.4 *Influence of Design Parameters*

- Different factors may affect the EMC behaviour of electrical machines, such as design variables, properties of materials, and tolerances associated to manufacturing processes. To go into detail about the design parameters and tolerances, normally FEM analysis is used as the main option.

- The analysis found in the literature is mainly focused on reducing bearing currents and insulation stress, so a broader approach may be needed to make an EMC strategy-based design for electrical machines.

6.1.3 High-Frequency Machine FEM Model

- A high-accuracy and low-computational-load simulation approach has been developed for calculating the high-frequency impedance of electrical machines. A novelty compared with other models is that the impedances, including the capacitances in the magnetic simulation, are calculated entirely via FEM simulations with a fast and accurate model.

- While the majority of models described in the literature were validated using the impedance measurements from only one or two machines, this research used the impedance from 28 industrial machines of the same model for validation purposes. Consequently, this approach took into account the effects of manufacturing tolerances on the impedance values. Additionally, 6 different industrial machines have been simulated by FEM and the obtained results show a very good agreement with experimental data. So it can be stated that the accuracy of the proposed model has been strongly validated.

- Typically, toroids are used in literature for the calibration of complex permeability in magnetic materials such as ferrites. However, to our knowledge, no one has so far studied laminated materials in this way. In this thesis, the modelling of the magnetic core via the complex permeability was validated with measurements of an M800-65A laminated toroid.
- The majority of models conventionally function beneath the 10 MHz threshold, and those surpassing this boundary frequently do not yield accurate results throughout the entire spectrum. The model developed in this thesis has undergone rigorous testing and has demonstrated accuracy within a range from 100 Hz to 50 MHz. This characteristic may prove advantageous in forthcoming scenarios, as technological advancements elevate the operational frequencies of devices, emission standards may expand the prescribed frequency ranges too.
- A systematic validation of the model was conducted, including a comparison between two versions: a full model and a simplified one. The simplified model omits capacitances between conductors, integrating them into the inter-coil capacitances instead. In assessing the balance between accuracy and simulation duration, the simplified model achieves a 66% decrease in simulation time while preserving adequate accuracy.
- The effect of the rotor was evaluated through comparisons of impedances with and without the rotor, along with the effects of varying rotor positions. Both simulations and experimental results indicated that the rotor presence damped the primary resonance in the common-mode impedance. Additionally, the rotor's presence and its positioning influenced the differential-mode impedance at frequencies below the EMI range of (150 kHz–30 MHz). Thus, the presence of the rotor does not affect the common-mode current in the high-frequency range, as both effects are out of this frequency range.

6.1.4 Full Drive Integrated Model

- Usually, in the literature, when analysing a full electric drive, the machine models are lumped parameter networks which parameters are fitted from experimental measurements. Thus, they are not valid for prediction in the design stage of the machine.
- In this thesis, a full drive model has been validated experimentally, using the motor impedance obtained from FEM simulations and fitting it to a lumped-parameter model with a basic genetic algorithm. The results show a rather good agreement with experimental data.
- The inverter and cable models used are based on impedance measurements since the focus of the thesis was the electric motor. However, a sufficient accuracy was obtained for the full simulation.
- The created full drive model proved beneficial for examining the high-frequency behaviour of the overall system as the motor's impedance changes, establishing it as an essential phase in the electric drive design process. The model reveals that motor impedance influences the full drive common mode current, though this is restricted to certain frequencies, specifically in the analysed case from 150 kHz to 3 MHz. Above 3 MHz, the significance shifts to the inverter and cable pathways.
- The filter used for EMC standard compliance is also modelled and validated within the model, thereby completing the full drive simulation.

6.1.5 Machine Design Methodology

- The presented design methodology is an improvement of the generally used one, including an EMC point of view.
- In the step where design improvements are made based on numerical tools, the presented high-frequency impedance model fits perfectly, as the typical electromagnetic simulation model can be completed with the capacitances from the electrostatic simulation and the modelling of the core in high frequency, to obtain the high-frequency impedance of the machine.
- For these design improvements, an analysis is made on the contributions of each design variable in the analysed motor, to take a reference of which is the most influential parameter in the high-frequency behaviour. The circuit configuration and the liner thickness are by far the most influential parameters, at least in the analysed cases.
- In the phase of performance analysis, the incorporation of a full drive model that predicts the electromagnetic interference of both the motor and the drive represents a significant advancement. This model facilitates modifications to the design of the machine or other components prior to prototyping. Furthermore, it enables the precise sizing of the EMC filter for each distinct application.
- The case study demonstrated that the integration of additional liner layers into a parallel circuit winding machine can equal the impedance and the common-mode currents with those observed in a series winding configuration, reducing the CM current in the grid about 10 dBμV at 2 MHz.
- The improvement of the design by adding two additional liner layers to the parallel winding machine prevents the drive from exceeding the grid current EMI standard limit.

6.2 FUTURE WORK

This PhD thesis has focused on the design and optimisation of PMSM from an EMC point of view. The developed high-frequency impedance model was validated accurately, as well as the full drive model. Moreover, after every research work, some further developments can be outlined. The main opportunities for further work could be:

- Regarding the high frequency impedance model, the validation of machines with distributed windings, or with bigger end-winding portion could be interesting to evaluate its impact on the model accuracy.
- Validating the full drive model using a three-phase LISN as established by the EMC regulations could be beneficial to increase the frequency range of the measurements, and would be a more accurate way of measuring the whole system electromagnetic interference.
- An interesting aspect that emerged from the analysis is that the voltage overshoot in the machine input decreased with the 3 liner layers, so a further analysis should be made to verify this effect on the partial discharges and consequently on the insulation lifetime.
- Respect to the electric drive components, modelling the cable and the inverter from data-sheet parameters or analytical equations, would make the model more multidisciplinary, as the cable and inverter could be changed without the need of measurements. In fact, a more complex cable model that the used PI model, could increase its accuracy.
- Regarding the machine model in the electric drive, it would be interesting to validate the drive when it has its nominal load, as in this PhD was modelled and validated with no load. Presumably, the current increase may have an impact on the high frequency behaviour of the machine and the drive.
- Observations from this thesis suggest that eliminating the EMC filter solely by altering the motor common mode impedance may not be feasible. However, a potential direction for future research could be to investigate the extent of filter reduction possible with the 10% decrease in common mode current achieved through modifications in motor design.
- Ultimately, the enhanced machine developed in Chapter 5 can be prototyped to facilitate an experimental comparison with the traditional machine within the drive system.
- As previously stated, the work presented in chapters 2 and 3 has been published in peer-reviewed journals. While the work presented in chapter 4 and the analysis in chapter 5 have not yet been published, efforts are underway to do so.

BIBLIOGRAPHY

[1] Y. Moreno, G. Almandoz, A. Egea, B. Arribas, and A. Urdangarin, "Analysis of Permanent Magnet Motors in High Frequency—A Review," *Applied Sciences*, vol. 11, no. 14, p. 6334, 7 2021. [Online]. Available: https://www.mdpi.com/2076-3417/11/14/6334

[2] Y. Moreno, A. Egea, G. Almandoz, G. Ugalde, A. Urdangarin, and R. Moreno, "High-Frequency Modelling of Electrical Machines for EMC Analysis," *Electronics*, vol. 13, no. 4, p. 787, 2 2024. [Online]. Available: https://www.mdpi.com/2079-9292/13/4/787

[3] Y. Moreno, A. Egea, G. Almandoz, G. Ugalde, A. Urdangarin, and R. Moreno, "High-Frequency Modelling of Windings," in *2022 International Conference on Electrical Machines (ICEM)*. IEEE, 9 2022, pp. 1232–1238. [Online]. Available: https://ieeexplore.ieee.org/document/9910696/

[4] United Nations, "Sustainable development goals," 2015, accessed: 12/01/2024. [Online]. Available: https://sdgs.un.org/goals

[5] European Parliament, "More electric cars on EU roads by 2030," 2018. [Online]. Available: https://www.europarl.europa.eu/news/en/press-room/20180911IPR13114/more-electric-cars-on-eu-roads-by-2030

[6] International Energy Agency, "Key World Energy Statistics," IEA, Tech. Rep., 2021. [Online]. Available: https://www.iea.org/reports/key-world-energy-statistics-2021

[7] A. K. Morya, M. C. Gardner, B. Anvari, L. Liu, A. G. Yepes, J. Doval-Gandoy, and H. A. Toliyat, "Wide Bandgap Devices in AC Electric Drives: Opportunities and Challenges," *IEEE Transactions on Transportation Electrification*, vol. 5, no. 1, pp. 3–20, 3 2019. [Online]. Available: https://ieeexplore.ieee.org/document/8611115/

[8] P. Mazurck, A. Michalski, H. Swiatck, C. Mazzetti, and Z. Flisowski, "Hazard for insulation and relevant emc problems due to voltages in circuits of motor supply by pwm converters," in *2003 IEEE Bologna Power Tech Conference Proceedings,*, vol. 2. IEEE, 2003, pp. 728–732. [Online]. Available: http://ieeexplore.ieee.org/document/1304637/

[9] Z. Shen, D. Jiang, T. Zou, and R. Qu, "Dual-Segment Three-Phase PMSM With Dual Inverters for Leakage Current and Common-Mode EMI Reduction," *IEEE Transactions on Power Electronics*, vol. 34, no. 6, pp. 5606–5619, 6 2019. [Online]. Available: https://ieeexplore.ieee.org/document/8440757/

[10] G. Spadacini, F. Grassi, and S. A. Pignari, "Conducted emissions in the powertrain of electric vehicles," in *2017 IEEE International Symposium on Electromagnetic Compatibility & Signal/Power Integrity (EMCSI)*, vol. 69, no. July. IEEE, 8 2017, pp. 1–28. [Online]. Available: http://ieeexplore.ieee.org/document/8078064/

[11] E. Robles, M. Fernandez, E. Ibarra, J. Andreu, and I. Kortabarria, "Mitigation of common mode voltage issues in electric vehicle drive systems by means of an

alternative AC-decoupling power converter topology," *Energies*, vol. 12, no. 17, p. 3349, 8 2019. [Online]. Available: https://www.mdpi.com/1996-1073/12/17/3349

[12] E. Robles, M. Fernandez, J. Andreu, E. Ibarra, and U. Ugalde, "Advanced power inverter topologies and modulation techniques for common-mode voltage elimination in electric motor drive systems," *Renewable and Sustainable Energy Reviews*, vol. 140, no. January, p. 110746, 4 2021. [Online]. Available: https://doi.org/10.1016/j.rser.2021.110746https://linkinghub.elsevier.com/retrieve/pii/S136403212100040X

[13] J. Zhang, M. Shen, and X. Zhao, "Study on the Effect of Inverter Modulation Methods and Operating Condition on Common Mode EMI for Motor Drive System," in *SAE Technical Papers*, vol. 2017-March, no. March, 3 2017. [Online]. Available: https://www.sae.org/content/2017-01-1223/

[14] K. Vostrov, J. Pyrhonen, M. Niemela, J. Ahola, and P. Lindh, "Mitigating Noncirculating Bearing Currents by a Correct Stator Magnetic Circuit and Winding Design," *IEEE Transactions on Industrial Electronics*, vol. 68, no. 5, pp. 3805–3812, 5 2021. [Online]. Available: https://ieeexplore.ieee.org/document/9057574/

[15] T. Weber, "EMC filters in high voltage traction drive systems," *IEEE International Symposium on Electromagnetic Compatibility*, 2008.

[16] L. Dawson, A. Rowell, R. Armstrong, and A. Ruddle, "EMC Design Guidelines for manufacturers of vehicle electric drives," York EMC Services, York, Tech. Rep. 314609, 2014. [Online]. Available: https://www.researchgate.net/publication/335724266_EMC_Design_Guidelines_for_manufacturers_of_vehicle_electric_drives_HEMIS_Deliverable_61

[17] European Committee for Electrotechnical Standardization, "EN 55011: Industrial, scientific and medical equipment-Electromagnetic disturbance characteristics - Limits and methods of measurement," 2016. [Online]. Available: https://tienda.aenor.com/norma-une-en-55011-2016-n0057077

[18] European Committee for Standardization, "EN 12015: Electromagnetic compatibility. Product family standard for lifts, escalators and moving walks. Emission." 2021. [Online]. Available: https://tienda.aenor.com/norma-une-en-12015-2021-n0065539

[19] S. Kim and D. P. Neikirk, "Compact equivalent circuit model for the skin effect," *IEEE MTT-S International Microwave Symposium Digest*, vol. 3, pp. 1815–1818, 1996.

[20] N. Idir, Y. Weens, and J. J. Franchaud, "Skin effect and dielectric loss models of power cables," *IEEE Transactions on Dielectrics and Electrical Insulation*, vol. 16, no. 1, pp. 147–154, 2009.

[21] O. Mohammed, S. Ganu, N. Abed, S. Liu, and Z. Liu, "High frequency PM synchronous motor model determined by FE analysis," *IEEE Transactions on Magnetics*, vol. 42, no. 4, pp. 1291–1294, 4 2006. [Online]. Available: http://ieeexplore.ieee.org/document/1608450/

[22] A. Al-Timimy, P. Giangrande, M. Degano, M. Galea, and C. Gerada, "Investigation of AC Copper and Iron Losses in High-Speed High-Power Density PMSM," in *2018 XIII International Conference on Electrical Machines (ICEM)*. IEEE, 9 2018, pp. 263–269. [Online]. Available: https://ieeexplore.ieee.org/document/8507166/

[23] B. Heidler, K. Brune, and M. Doppelbauer, "High-frequency model and parameter identification of electrical machines using numerical simulations," in *2015 IEEE International Electric Machines & Drives Conference (IEMDC)*. IEEE, 5 2015, pp. 1221–1227. [Online]. Available: http://ieeexplore.ieee.org/document/7409217/

[24] Kohji Maki, Hiroki Funato, and Liang Shao, "Motor modeling for EMC simulation by 3-D electromagnetic field analysis," in *2009 IEEE International Electric Machines and Drives Conference*. IEEE, 5 2009, pp. 103–108. [Online]. Available: http://ieeexplore.ieee.org/document/5075190/

[25] O. A. Mohammed, S. Ganu, S. Liu, Z. Liu, and N. Abed, "Study of high frequency model of permanent magnet motor," *2005 IEEE International Conference on Electric Machines and Drives*, pp. 622–627, 2005.

[26] A. Rahimi and K. Kanzi, "Improved High-Frequency Modeling of PMSM Using 3-D Finite Element Analysis," in *2019 International Power System Conference (PSC)*. IEEE, 12 2019, pp. 71–78. [Online]. Available: https://ieeexplore.ieee.org/document/9081510/

[27] J. E. Ruiz-Sarrio, F. Chauvicourt, J. Gyselinck, and C. Martis, "High-Frequency Modelling of Electrical Machine Windings Using Numerical Methods," in *2021 IEEE International Electric Machines & Drives Conference (IEMDC)*. IEEE, 5 2021, pp. 1–7. [Online]. Available: https://ieeexplore.ieee.org/document/9449561/

[28] P. Brauer, "High-Frequency Voltage Distribution Modelling of a Slotless PMSM from a Machine Design Perspective," Ph.D. dissertation, KTH ROYAL INSTITUTE OF TECHNOLOGY, 2018.

[29] G. R. Skutt, F. C. Lee, D. Chen, and W. Kohler, "High-Frequency Dimensional Effects in Ferrite-Core Magnetic Devices," Ph.D. dissertation, Virginia Polytechnic Institute and State University, 1996.

[30] K. G. B. Abeywickrama, T. Daszczynski, Y. V. Serdyuk, and S. M. Gubanski, "Determination of complex permeability of silicon steel for use in high-frequency modeling of power transformers," *IEEE Transactions on Magnetics*, vol. 44, no. 4, pp. 438–444, 2008.

[31] D. Zhang, L. Kong, and X. Wen, "A novel simple IGBT model for power electronic systems EMI simulation," *IEEE Transportation Electrification Conference and Expo, ITEC Asia-Pacific 2014 - Conference Proceedings*, pp. 1–5, 2014.

[32] M. Jaritz, C. Jaeger, M. Bucher, J. Smajic, D. Vukovic, and S. Blume, "An Improved Model for Circulating Bearing Currents in Inverter-Fed AC Machines," in *2019 IEEE International Conference on Industrial Technology (ICIT)*. IEEE, 2 2019, pp. 225–230. [Online]. Available: https://ieeexplore.ieee.org/document/8755123/

[33] J. O. Stockbrügger and B. Ponick, "Analytical determination of the end-winding portion of the winding-to-rotor capacitance for the prediction of bearing voltage in electrical machines," *Electrical Engineering*, vol. 102, no. 4, pp. 2481–2491, 12 2020. [Online]. Available: http://link.springer.com/10.1007/s00202-020-01046-y

[34] X. Ma, R. Liu, B. Zheng, and Y. Zhang, "Analysis and calculation of capacitance parameters in induction machines to predict shaft voltage," *ICEMS 2012 - Proceedings: 15th International Conference on Electrical Machines and Systems*, 2012.

[35] Y. Kwack, H. Kim, C. Song, M. Moon, D.-H. Kim, B. Kim, E. Kim, and J. Kim, "EMI modeling method of interior permanent magnet synchronous motor for hybrid electric vehicle drive system considering parasitic and dynamic parameters," in *2015 Asia-Pacific Symposium on Electromagnetic Compatibility (APEMC)*. IEEE, 5 2015, pp. 78–81. [Online]. Available: http://ieeexplore.ieee.org/document/7175390/

[36] F. Zare, "Practical approach to model electric motors for electromagnetic interference and shaft voltage analysis," *IET Electric Power Applications*, vol. 4, no. 9, pp. 727–738, 2010.

[37] H. Miloudi, A. Bendaoud, M. Miloudi, S. Dickmann, and S. Schenke, "Common mode and differential mode characteristics of AC motor for EMC analysis," in *2016 International Symposium on Electromagnetic Compatibility - EMC EUROPE*, vol. 2016-Novem. IEEE, 9 2016, pp. 765–769. [Online]. Available: http://ieeexplore.ieee.org/document/7739260/

[38] S. Lee, M. Liu, W. Lee, and B. Sarlioglu, "Comparison of High-Frequency Impedance of AC Machines with Circumferential and Toroidal Winding Topologies for SiC MOSFET Machine Drives," in *2020 IEEE Energy Conversion Congress and Exposition (ECCE)*. IEEE, 10 2020, pp. 3572–3579. [Online]. Available: https://ieeexplore.ieee.org/document/9236160/

[39] Y. Xiong, X. Li, Y. Li, and X. Zhao, "A High-frequency Motor Model Constructed Based on Vector Fitting Method," in *2019 Joint International Symposium on Electromagnetic Compatibility, Sapporo and Asia-Pacific International Symposium on Electromagnetic Compatibility (EMC Sapporo/APEMC)*. IEEE, 6 2019, pp. 191–194. [Online]. Available: https://ieeexplore.ieee.org/document/8893649/

[40] Y. Xiong, X. Chen, L. Zong, X. Li, X. Nie, G. Yang, and X. Zhao, "An Electric Drive System Modelling Method Based on Module Behavior," in *2019 International Conference on Microwave and Millimeter Wave Technology, ICMMT 2019 - Proceedings*. IEEE, 5 2019, pp. 1–3. [Online]. Available: https://ieeexplore.ieee.org/document/8992334/

[41] M. A. Gries and B. Mirafzal, "Permanent magnet motor-drive frequency response characterization for transient phenomena and conducted EMI analysis," in *2008 Twenty-Third Annual IEEE Applied Power Electronics Conference and Exposition*, no. 1. IEEE, 2 2008, pp. 1767–1775. [Online]. Available: http://ieeexplore.ieee.org/document/4522966/

[42] Z. Duan and X. Wen, "A new analytical conducted EMI prediction method for SiC motor drive systems," *eTransportation*, vol. 3, p. 100047, 2 2020. [Online]. Available: https://doi.org/10.1016/j.etran.2020.100047https://linkinghub.elsevier.com/retrieve/pii/S2590116820300047

[43] I. Oganezova, R. Kado, B. Khvitia, Z. Kuchadze, A. Gheonjian, and R. Jobava, "EMC model of low voltage DC motor," in *2014 IEEE International Symposium on Electromagnetic Compatibility (EMC)*, vol. 2014-Septe, no. September. IEEE, 8 2014, pp. 81–85. [Online]. Available: http://ieeexplore.ieee.org/document/6898947/

[44] M. Schinkel, S. Weber, S. Guttowski, W. John, and H. Reichl, "Efficient HF Modeling and Model Parameterization of Induction Machines for Time and Frequency Domain Simulations," in *Twenty-First Annual IEEE Applied Power Electronics Conference and Exposition, 2006. APEC '06.*, vol. 2006. IEEE, 2006, pp. 1181–1186. [Online]. Available: http://ieeexplore.ieee.org/document/1620689/

[45] M. Cai, T. Craddock, and O. Wasynczuk, "High-frequency modeling, parameterization, and simulation of IPM motor drive systems," in *2017 IEEE Power and Energy Conference at Illinois (PECI)*. IEEE, 2 2017, pp. 1–8. [Online]. Available: http://ieeexplore.ieee.org/document/7935769/

[46] D. Zhang, L. Kong, X. Wen, and Z. Duan, "Interior permanent magnet motor drive system modeling for electromagnetic interference analysis," in *2014 17th International Conference on Electrical Machines and Systems (ICEMS)*. IEEE, 10 2014, pp. 1498–1504. [Online]. Available: http://ieeexplore.ieee.org/document/7013728/

[47] A. Hoffmann and B. Ponick, "Statistical Deviation of High-Frequency Lumped Model Parameters for Stator Windings in Three-Phase Electrical Machines," in *2020 International Symposium on Power Electronics, Electrical Drives, Automation and Motion (SPEEDAM)*. IEEE, 6 2020, pp. 85–90. [Online]. Available: https://ieeexplore.ieee.org/document/9161915/

[48] W. Czuchra, "Modelling of the Traction Induction Motor in the Frequency Band of Electromagnetic Conducted Disturbances," in *2018 International Symposium on Electrical Machines (SME)*. IEEE, 6 2018, pp. 1–4. [Online]. Available: https://ieeexplore.ieee.org/document/8442838/

[49] D. Zhang, L. Kong, and X. Wen, "A measurement based modeling method of interior permanent magnet motor considering the rotor position for EMI analysis," *IEEE Transportation Electrification Conference and Expo, ITEC Asia-Pacific 2014 - Conference Proceedings*, pp. 1–6, 2014.

[50] J. Sun and L. Xing, "Parameterization of Three-Phase Electric Machine Models for EMI Simulation," *IEEE Transactions on Power Electronics*, vol. 29, no. 1, pp. 36–41, 1 2014. [Online]. Available: http://ieeexplore.ieee.org/document/6519273/

[51] A. Boglietti, A. Cavagnino, and M. Lazzari, "Experimental high-frequency parameter identification of ac electrical motors," *IEEE Transactions on Industry Applications*, vol. 43, no. 1, pp. 23–29, 2007.

[52] E. Carpaneto, A. Boglietti, "An Accurate Induction Motor High-Frequency Model for Electromagnetic Compatibility Analysis," *Electric Power Components and Systems*, vol. 29, no. 3, pp. 191–209, 3 2001. [Online]. Available: http://www.tandfonline.com/doi/abs/10.1080/153250001300006626

[53] X. Pan, R. Ehrhard, and R. Vick, "An extended high frequency model of permanent magnet synchronous motors in hybrid vehicles," *Proceedings of EMC Europe 2011 York - 10th International Symposium on Electromagnetic Compatibility*, pp. 690–694, 2011.

[54] G. Vidmar and D. Miljavec, "A Universal High-Frequency Three-Phase Electric-Motor Model Suitable for the Delta- and Star-Winding Connections," *IEEE Transactions on Power Electronics*, vol. 30, no. 8, pp. 4365–4376, 2015.

[55] M. Mohammadi-Rostam, M. Shahabi, and A. A. Shayegani-Akmal, "High frequency lumped parameter model for EMI problems and over voltage analysis of Induction motor," *Journal of Electrical Engineering*, vol. 13, no. 3, pp. 278–283, 2013.

[56] V. Gavrilenko and V. Gavrilenko, "Characterization of winding insulation of electrical machines fed by voltage waves with high dV / dt," Ph.D. dissertation, Université Paris-Saclay,Université polytechnique de Tomsk (Russie), 2020. [Online]. Available: https://tel.archives-ouvertes.fr/tel-03102553

[57] Y. Wu, C. Bi, K. Jia, D. Jin, H. Li, W. Yao, and G. Liu, "High-frequency modelling of permanent magnet synchronous motor with star connection," *IET Electric Power Applications*, vol. 12, no. 4, pp. 539–546, 4 2018. [Online]. Available: https://onlinelibrary.wiley.com/doi/10.1049/iet-epa.2017.0593

[58] M. S. Toulabi, L. Wang, L. Bieber, S. Filizadeh, and J. Jatskevich, "A Universal High-Frequency Induction Machine Model and Characterization Method for Arbitrary Stator Winding Connections," *IEEE Transactions on Energy Conversion*, vol. 34, no. 3, pp. 1164–1177, 9 2019. [Online]. Available: https://ieeexplore.ieee.org/document/8606154/

[59] B. Mirafzal, G. L. Skibinski, R. M. Tallam, D. W. Schlegel, and R. A. Lukaszewski, "Universal induction motor model with low-to-high frequency-response characteristics," *IEEE Transactions on Industry Applications*, vol. 43, no. 5, pp. 1233–1246, 2007.

[60] M. Kane, A. Ahmad, and P. Auriol, "Multiwire Shielded Cable Parameter Computation," *IEEE Transactions on Magnetics*, vol. 31, no. 3, pp. 1646–1649, 1995.

[61] N. Radja, M. Rachek, and S. N. Larbi, "Improved RLMC-Circuit HF-Dependent Parameters Using FE-EM Computation Dedicated to Predict Fast Transient Voltage Along Insulated Windings," *IEEE Transactions on Electromagnetic Compatibility*, vol. 61, no. 1, pp. 301–308, 2019.

[62] J. Guardado and K. Cornick, "Calculation of machine winding electrical parameters at high frequencies for switching transient studies," *IEEE Transactions on Energy Conversion*, vol. 11, no. 1, pp. 33–40, 3 1996. [Online]. Available: http://ieeexplore.ieee.org/document/486573/

[63] A. Muetze and A. Binder, "Calculation of motor capacitances for prediction of the voltage across the bearings in machines of inverter-based drive systems," *IEEE Transactions on Industry Applications*, vol. 43, no. 3, pp. 665–672, 2007.

[64] J. I. Ramos, J.-M. Dienot, P.-E. Vidal, C. Viguier, and B. Nogarede, "Contribution to modeling of parasitic couplings for predicting EMC behavior of electrical machines," in *2014 International Conference on Electrical Machines (ICEM)*. IEEE, 9 2014, pp. 1056–1062. [Online]. Available: http://ieeexplore.ieee.org/document/6960312/

[65] J. Benecke, "Impedance and Emission Optimization of Low-Voltage DC Motors for EMC Compliance," *IEEE Transactions on Industrial Electronics*, vol. 58, no. 9, pp. 3833–3839, 9 2011. [Online]. Available: http://ieeexplore.ieee.org/document/5595497/

[66] N. Djukic, L. Encica, and J. J. H. Paulides, "Electrical machines: Comparison of existing analytical models and FEM for calculation of turn-to-turn capacitance in formed windings," in *2016 Eleventh International Conference on Ecological Vehicles and Renewable Energies (EVER)*, no. April. IEEE, 4 2016, pp. 1–8. [Online]. Available: http://ieeexplore.ieee.org/document/7476427/

[67] N. Djukic, L. Encica, and J. J. H. Paulides, "Electrical machines: Turn-to-turn capacitance in formed windings with rectangular cross-section wire," in *2015 International Conference on Sustainable Mobility Applications, Renewables and Technology (SMART)*, no. July 2016. IEEE, 11 2015, pp. 1–4. [Online]. Available: http://ieeexplore.ieee.org/document/7399244/

[68] C. Martis, H. Hedesiu, and B. Tataranu, "High-frequency model and conductive interferences of a small doubly salient permanent magnet machine,"

in *2004 IEEE International Conference on Industrial Technology, 2004. IEEE ICIT '04.*, vol. 3. IEEE, 2004, pp. 1378–1383. [Online]. Available: http://ieeexplore.ieee.org/document/1490762/

[69] P. Maki-Ontto and J. Luomi, "Induction motor model for the analysis of capacitive and induced shaft voltages," in *IEEE International Conference on Electric Machines and Drives, 2005.* IEEE, 2005, pp. 1653–1660. [Online]. Available: http://ieeexplore.ieee.org/document/1531559/

[70] P. Mäki-ontto, "Modeling and Reduction of Shaft Voltages in Ac Motors Fed By Frequency Converters," Ph.D. dissertation, HELSINKI UNIVERSITY OF TECHNOLOGY, 2006.

[71] J. Ferreira, "Improved analytical modeling of conductive losses in magnetic components," *IEEE Transactions on Power Electronics*, vol. 9, no. 1, pp. 127–131, 1 1994. [Online]. Available: https://ieeexplore.ieee.org/document/285503/

[72] P. B. Reddy, Z. Q. Zhu, S.-H. Han, and T. M. Jahns, "Strand-level proximity losses in PM machines designed for high-speed operation," in *2008 18th International Conference on Electrical Machines*, no. 1. IEEE, 9 2008, pp. 1–6. [Online]. Available: http://ieeexplore.ieee.org/document/4800172/

[73] O. Magdun, A. Binder, C. Purcarea, and A. Rocks, "High-frequency induction machine models for calculation and prediction of common mode stator ground currents in electric drive systems," *2009 13th European Conference on Power Electronics and Applications, EPE '09*, pp. 1–8, 2009.

[74] K. Vostrov, J. Pyrhonen, J. Ahola, and M. Niemela, "Non-circulating Bearing Currents Mitigation Approach Based on Machine Stator Design Options," *Proceedings - 2018 23rd International Conference on Electrical Machines, ICEM 2018*, pp. 866–872, 2018.

[75] O. A. Mohammed and S. Ganu, "FE-Circuit Coupled Model of Electric Machines for Simulation and Evaluation of EMI Issues in Motor Drives," *IEEE Transactions on Magnetics*, vol. 46, no. 8, pp. 3389–3392, 8 2010. [Online]. Available: http://ieeexplore.ieee.org/document/5512907/

[76] P. Sangha and T. Sawata, "Evaluation of winding stray capacitance in motors for aerospace applications," in *2017 IEEE International Electric Machines and Drives Conference (IEMDC).* IEEE, 5 2017, pp. 1–6. [Online]. Available: http://ieeexplore.ieee.org/document/8002265/

[77] R. Ferreira and A. Ferreira, "Transient model to study voltage distribution in electrical machine windings considering the rotor," *Electric Power Systems Research*, vol. 195, no. March, p. 107155, 6 2021. [Online]. Available: https://doi.org/10.1016/j.epsr.2021.107155https://linkinghub.elsevier.com/retrieve/pii/S037877962100136X

[78] M. Jaritz, N. Stieger, C. Jaeger, M. Schneider, D. Vukovic, S. Blume, and J. Smajic, "An Improved Model for the Common Mode Impedance in Inverter-Fed AC Machines," in *2020 International Conference on Electrical Machines (ICEM).* IEEE, 8 2020, pp. 1053–1059. [Online]. Available: https://ieeexplore.ieee.org/document/9270808/

[79] H. De Gersem, O. Henze, T. Weiland, and A. Binder, "Transmission-line modelling of wave propagation effects in machine windings," in *2008 13th International Power Electronics and Motion Control Conference*, no. 3. IEEE, 9 2008, pp. 2385–2392. [Online]. Available: http://ieeexplore.ieee.org/document/4635621/

[80] J. Zhang, W. Xu, C. Gao, S. Wang, J. Qiu, J. G. Zhu, and Y. Guo, "Analysis of inter-turn insulation of high voltage electrical machine by using multi-conductor transmission line model," *IEEE Transactions on Magnetics*, vol. 49, no. 5, pp. 1905–1908, 2013.

[81] R. S. Ferreira and A. C. Ferreira, "Transient Voltage Distribution in Induction Motor Stator Windings Using Finite Elements Method," in *IECON 2018 - 44th Annual Conference of the IEEE Industrial Electronics Society*. IEEE, 10 2018, pp. 737–742. [Online]. Available: https://ieeexplore.ieee.org/document/8595148/

[82] J. E. R. Sarrio, C. Martis, and F. Chauvicourt, "Numerical Computation of Parasitic Slot Capacitances in Electrical Machines," in *2020 International Conference and Exposition on Electrical And Power Engineering (EPE)*, no. October. IEEE, 10 2020, pp. 146–150. [Online]. Available: https://ieeexplore.ieee.org/document/9305616/

[83] F. Birnkammer, J. Chen, D. B. Pinhal, and D. Gerling, "Influence of the Modeling Depth and Voltage Level on the AC Losses in Parallel Conductors of a Permanent Magnet Synchronous Machine," *IEEE Transactions on Applied Superconductivity*, vol. 28, no. 3, pp. 1–5, 2018.

[84] V. Venegas, J. L. Guardado, E. Melgoza, and M. Hernandez, "A finite element approach for the calculation of electrical machine parameters at high frequencies," *2007 IEEE Power Engineering Society General Meeting, PES*, vol. 0, no. 1, 2007.

[85] A. Krings, G. Paulsson, F. Sahlen, and B. Holmgren, "Experimental investigation of the voltage distribution in form wound windings of large AC machines due to fast transients," *Proceedings - 2016 22nd International Conference on Electrical Machines, ICEM 2016*, pp. 1700–1706, 2016.

[86] C.-N. Behrendt, J. Dittmann, B. Knebusch, and B. Ponick, "An Investigation Into the Trade-Off Between Full Machine and Single-Slot FEM Simulations for Electrical Machine Modeling at High Frequencies With Respect to Inter-Wire Couplings," in *2022 International Conference on Electrical Machines, ICEM 2022*, 2022.

[87] G. Volpe, M. Popescu, F. Marignetti, and J. Goss, "AC winding losses in automotive traction e-machines: A new hybrid calculation method," *2019 IEEE International Electric Machines and Drives Conference, IEMDC 2019*, pp. 2115–2119, 2019.

[88] N. Taran, D. M. Ionel, V. Rallabandi, G. Heins, and D. Patterson, "An Overview of Methods and a New Three-Dimensional FEA and Analytical Hybrid Technique for Calculating AC Winding Losses in PM Machines," *IEEE Transactions on Industry Applications*, vol. 57, no. 1, pp. 352–362, 1 2021. [Online]. Available: https://ieeexplore.ieee.org/document/9242250/

[89] M. Ceraolo and D. Poli, *Fundamentals of Electric Power Engineering*, M. Ceraolo and D. Poli, Eds. Hoboken, New Jersey: John Wiley & Sons, Inc., 4 2014. [Online]. Available: http://doi.wiley.com/10.1002/9781118922583

[90] D. Fleisch, *A Student's Guide to Maxwell's Equations*, 1st ed. New York: Cambridge University Press, 2008.

[91] H. Zhao, H. H. Eldeeb, Y. Zhang, D. Zhang, Y. Zhan, G. Xu, and O. A. Mohammed, "An Improved Core Loss Model of Ferromagnetic Materials Considering High-Frequency and Non-Sinusoidal Supply," *IEEE Transactions on Industry Applications*, vol. 9994, no. c, pp. 1–1, 2021. [Online]. Available: https://ieeexplore.ieee.org/document/9403938/

[92] J. Smajic, M. Bucher, T. Franz, B. Cranganu-Cretu, A. Shoory, and J. Tepper, "Modeling of Frequency Dependent Parameters in Time Domain High Frequency Transformer Simulations," *Procedia Engineering*, vol. 202, pp. 251–263, 2017. [Online]. Available: https://doi.org/10.1016/j.proeng.2017.09.712

[93] D. Winterborne, S. Jordan, L. Sjoberg, and G. Atkinson, "Estimation of AC copper loss in electrical machine windings with consideration of end effects," in *2020 International Conference on Electrical Machines (ICEM)*. IEEE, 8 2020, pp. 847–853. [Online]. Available: https://ieeexplore.ieee.org/document/9270816/

[94] C. Jaeger, I. Grinbaum, and J. Smajic, "Numerical simulation and measurement of common-mode and circulating bearing currents," in *2016 XXII International Conference on Electrical Machines (ICEM)*, no. Cm. IEEE, 9 2016, pp. 486–491. [Online]. Available: http://ieeexplore.ieee.org/document/7732570/

[95] O. A. Mohammed, S. Ganu, N. Abed, Z. Liu, and S. Liu, "High frequency modeling of PM synchronous machine for use in integrated motor drive," *IEEE Electric Ship Technologies Symposium, ESTS 2007*, pp. 245–249, 2007.

[96] J. E. Ruiz-Sarrió, "High-Frequency Modelling of Rotating Electrical Machines," Ph.D. dissertation, Technical University of Cluj-Napoca Romania, 2022.

[97] C.-N. Behrendt, J. Dittmann, B. Knebusch, and B. Ponick, "Common-Mode Impedance Prediction of a High Frequency Hairpin Stator Winding Based on FEM and Modified Nodal Analysis," in *2022 International Symposium on Power Electronics, Electrical Drives, Automation and Motion (SPEEDAM)*. IEEE, 6 2022, pp. 20–26. [Online]. Available: https://ieeexplore.ieee.org/document/9841953/

[98] K. Maki, "Automated technique for building high-frequency equivalent circuits of motors based on electromagnetic field analysis," *Electrical Engineering in Japan (English translation of Denki Gakkai Ronbunshi)*, vol. 215, no. 3, pp. 1–9, 2022.

[99] S. Mahdavi and K. Hameyer, "High frequency equivalent circuit model of the stator winding in electrical machines," in *Proceedings - 2012 20th International Conference on Electrical Machines, ICEM 2012*. IEEE, 9 2012, pp. 1706–1711. [Online]. Available: http://ieeexplore.ieee.org/document/6350110/

[100] D. Rincón, E. Aguilera, and J. C. Chacón, "Numerical treatment of floating conductors based on the traditional finite element formulation," *Advanced Electromagnetics*, vol. 7, no. 3, pp. 46–55, 2018.

[101] K. Vostrov, J. Pyrhonen, and J. Ahola, "Shielding the end windings to reduce bearing currents," in *2020 International Conference on Electrical Machines (ICEM)*, no. June. Gothenburg: IEEE, 8 2020, pp. 1431–1437. [Online]. Available: https://ieeexplore.ieee.org/document/9270673/

[102] P. Dowell, "Effects of eddy currents in transformer windings," *Proceedings of the Institution of Electrical Engineers*, vol. 113, no. 8, p. 1387, 1966. [Online]. Available: https://digital-library.theiet.org/content/journals/10.1049/piee.1966.0236

[103] Electric Machinery Committee, "IEEE Standard Test Procedure for Polyphase Induction Motors and Generators," IEEE, Tech. Rep. 4, 2 2018. [Online]. Available: https://ieeexplore.ieee.org/document/8291810

[104] N. Djukic, L. Encica, and J. J. H. Paulides, "Overview of capacitive couplings in windings," in *2015 Tenth International Conference on Ecological Vehicles and Renewable Energies (EVER)*. IEEE, 3 2015, pp. 1–11. [Online]. Available: http://ieeexplore.ieee.org/document/7112940/

[105] A. Massarini and M. Kazimierczuk, "Self-capacitance of inductors," *IEEE Transactions on Power Electronics*, vol. 12, no. 4, pp. 671–676, 7 1997. [Online]. Available: https://ieeexplore.ieee.org/document/602562/

[106] Y.-M. Yang, H.-M. Peng, and Q.-D. Wang, "Common Model EMI Prediction in Motor Drive System for Electric Vehicle Application," *Journal of Electrical Engineering and Technology*, vol. 10, no. 1, pp. 205–215, 1 2015. [Online]. Available: http://koreascience.or.kr/journal/view.jsp?kj=E1EEFQ&py=2015&vnc=v10n1&sp=205

[107] G. Almandoz, S. Zarate, A. Egea, Y. Moreno, A. Urdangarin, and R. Moreno, "High Frequency Modeling of Electric Drives for Electromagnetic Compatibility Analysis," in *2020 International Conference on Electrical Machines (ICEM)*. IEEE, 8 2020, pp. 1129–1135. [Online]. Available: https://ieeexplore.ieee.org/document/9270804/

[108] H. Peng, N. Driendl, S. Stevic, D. Butterweck, Y. Firouz, L. Sharifian, and K. Hameyer, "High-frequency Modeling of Permanent Magnet Synchronous Machines using Grey Box Models," *IEEE Transactions on Transportation Electrification*, vol. PP, no. 8, pp. 1–1, 2024. [Online]. Available: https://ieeexplore.ieee.org/document/10423906/

[109] F. Abdallah, "EMC Analysis of Electric Drives," Ph.D. dissertation, LUND University, 2012. [Online]. Available: https://www.iea.lth.se/publications/Theses/LTH-IEA-1065.pdf

[110] M. Popov, "General approach for accurate resonance analysis in transformer windings," *Electric Power Systems Research*, vol. 161, pp. 45–51, 8 2018. [Online]. Available: https://linkinghub.elsevier.com/retrieve/pii/S0378779618301019

[111] X. Zhao, C. Yao, A. Abu-Siada, and R. Liao, "High frequency electric circuit modeling for transformer frequency response analysis studies," *International Journal of Electrical Power and Energy Systems*, vol. 111, no. April, pp. 351–368, 2019. [Online]. Available: https://doi.org/10.1016/j.ijepes.2019.04.010

[112] N. Boucenna, S. Hlioui, B. Revol, and F. Costa, "A detailed analysis of the propagation paths of high-frequency common mode currents in AC motors," in *2013 15th European Conference on Power Electronics and Applications, EPE 2013*, 2013.

[113] P. Mellor, R. Wrobel, and N. McNeill, "Investigation of Proximity Losses in a High Speed Brushless Permanent Magnet Motor," in *Conference Record of the 2006 IEEE Industry Applications Conference Forty-First IAS Annual Meeting*, vol. 3, no. c. IEEE, 10 2006, pp. 1514–1518. [Online]. Available: http://ieeexplore.ieee.org/document/4025417/

[114] I. Kovacova and V. Melnykov, "Magnetic Fields of DC PM Motor and its EMC," *Proceedings of the International Conference on Modern Electrical and Energy Systems, MEES 2019*, pp. 186–189, 2019.

[115] N. Taran, V. Rallabandi, D. M. Ionel, P. Zhou, M. Thiele, and G. Heins, "A Systematic Study on the Effects of Dimensional and Materials Tolerances on Permanent Magnet Synchronous Machines Based on the IEEE Std 1812," *IEEE Transactions on Industry Applications*, vol. 55, no. 2, pp. 1360–1371, 2019.

[116] S. Zhu and B. Shi, "Modeling of PWM-Induced Iron Losses with Frequency-Domain Methods and Low-Frequency Parameters," *IEEE Transactions on Industrial Electronics*, vol. 69, no. 3, pp. 2402–2413, 2022.

[117] I. Gómez Serna, "Design methodology for achieving reliable permanent magnet synchronous machines," Ph.D. dissertation, Mondragon Unibertsitatea, 2017. [Online]. Available: https://dialnet.unirioja.es/servlet/tesis?codigo=250047&info=resumen&idioma=SPA%0Ahttps://dialnet.unirioja.es/servlet/tesis?codigo=250047

[118] International Electrotechnical Commission, "Iec 60034-18-41:2014 rotating electrical machines: Partial discharge free electrical insulation systems (type i) used in rotating electrical machines fed from voltage converters - qualification and quality control tests," IEC Standard, 2019. [Online]. Available: https://tienda.aenor.com/norma-une-en-55011-2016-n0057077

[119] L. Elorza Azpiazu, G. Almandoz, A. Egea, G. Ugalde, and X. Badiola, "Study of partial discharge inception voltage in inverter fed electric motor insulation systems," *Applied Sciences*, vol. 13, no. 4, 2023. [Online]. Available: https://www.mdpi.com/2076-3417/13/4/2417

[120] L. Lusaurdi, A. Cavallini, and M. Degano, "The impact of impulsive voltage waveforms on the electrical insulation of actuators for more electrical aircraft (mea)," in *IECON 2017 - 43rd Annual Conference of the IEEE Industrial Electronics Society*, Oct 2017, pp. 4414–4418.